AMPLITUDE ANALYSES OF THE D^+, $D_s^+ \to K^-K^+\pi^+$ AND $D^0 \to K_s^o K^+K^-$ FINAL STATES

BY

AMIR M. RAHIMI

B.S., Rensselaer Polytechnic Institute, 1990
M.S., University of Illinois at Urbana-Champaign, 1993

THESIS

Submitted in partial fulfillment of the requirements
for the degree of Doctor of Philosophy in Physics
in the Graduate College of the
University of Illinois at Urbana-Champaign, 2000

Urbana, Illinois

AMPLITUDE ANALYSES OF THE D^+, $D_s^+ \to K^-K^+\pi^+$ AND $D^0 \to K_s^o K^+K^-$ FINAL STATES

Amir M. Rahimi, Ph.D.
Department of Physics
University of Illinois at Urbana-Champaign, 2000
Jim Wiss, Advisor

Amplitude analysis of the D^+, $D_s^+ \to K^-K^+\pi^+$ AND $D^0 \to K_s^o K^+K^-$ final states are presented using the data collected by the Fermilab high energy photoproduction experiment E831(FOCUS), during 96-97. Our data are fit to a model consisting of a sum of Breit-Wigner amplitudes for the intermediate two-body resonant decay modes. We extract decay fractions and relative phases. The $K_sK^+K^-$ analysis provides information on the decomposition of this mode into CP even and CP odd eigenstates channels.

To my wife Fariba,

and my parents.

Acknowledgments

The success of the E831 experiment was the foundation of my ability to complete this work. Over a hundred physicists and technicians from around the world are responsible for this success.

The E831 co-spokespersons, John Cumalat and Luigi Moroni, deserve much credit for providing the leadership, support and enthusiasm to bring this experiment to a level of success which exceeded all expectations.

The results of this thesis would not be possible without the efforts of all the individuals in the E831 collaboration. Although I may not even be aware of the importance of each of their contributions, I value them all equally.

Furthermore, the experimenters who developed E687 laid the framework for the state of the art design of E831.

Of the individuals with whom I worked, I value the most my association with my teacher and adviser Jim Wiss. With his open door policy, I always felt welcomed to walk in his office and discuss my work with him. His world expertise in Dalitz analysis techniques, E831, and high energy physics in general as well as his enthusiasm allowed me to accomplish much more than I could have otherwise.

My friend and colleague Topher Cawlfield deserves much recognition as well. His expertise in computer software and his patience in taking time to teach me many computing tasks were indispensable for completing this analysis.

Dave Lesny is responsible for creating and maintaining a computing environment which few other institutions can equal. There is much I could not have accomplished were this not true.

Fred Cogswell, the high energy physics machinist at UIUC, provided the excellent support that was needed to design and build the E831 inner muon detectors. I would also like to thank Kee-Su Park for his help in building and assembling the Muon Detector.

I would like to thank Eric Vaandering and Jon Link as well as Brian O'Reilly, Alberto Sanchez, Matt Nehring, and Joel Butler for their excellent work in making the data processing job easier for the rest of the collaboration. I would like to thank Paul Sheldon for doing a great job with the SEZDEE skim which was used in this analysis. I would also like to thank Dario Menasce, Daniele Pedrini, and Silvano Sala for providing the Milano Ntuples which we used for the CP lifetime analysis.

I would like to thank Francesco Prelz for an excellent job in providing us the support to readout the Cerenkov detector through the Data Acquisition System.

There are many others in the collaboration who I am thankful to, and beg their-forgiveness if I have not mentioned their names.

Finally, I would like to thank my family and friends for providing the support and encouragement during my years of graduate study. I would like to thank my parents for helping me to build a foundation for my education. I am also thankful to my wife's parents Dr. and Mrs. Kazemi for always being supportive and who treated me like one of their sons. Most of all my thanks goes to my wife Fariba whose love, understanding and support was invaluable; this work would not have been possible without her.

This research is funded in part by the U.S. Department of Energy under contract DOE F4650.2

Table of Contents

Chapter 1 Introduction 1
1.1 Review of Dalitz Analysis of Charm decay Phenomenology 3
1.1.1 Studies of non-leptonic charm decay 4
1.2 Previous Dalitz Analyzes 6
1.2.1 Factorization Models 7
1.2.2 Dalitz Analyzes 11
1.2.3 Motivation for the principle study of this thesis 16
1.2.4 Summary 21

Chapter 2 The E831 Apparatus 22
2.1 Beam line 23
2.1.1 Proton Beam 23
2.1.2 Photon Beam 25
2.2 Beam Tagging 28
2.3 Target 30
2.4 Silicon Strip Detectors 31
2.4.1 Target Silicon Detector 32
2.4.2 Microstrip Detector 32
2.5 The Analysis Magnets 34
2.6 Multiwire Proportional Chambers (MWPC's) 34
2.7 The Straw Tube System 36
2.8 Čerenkov System 36
2.8.1 C1 38
2.8.2 C2 40
2.8.3 C3 41
2.9 Calorimetry 44
2.9.1 Outer Electromagnetic Calorimeter (OE) 44
2.9.2 Inner Electromagnetic Calorimeter (IE) 44
2.9.3 Hadron Calorimeter (HC) 44
2.9.4 Beam Gamma Monitor Calorimeter (BGM) 46
2.10 Muon Detector 46
2.11 Trigger 48
2.11.1 First Level Trigger 48
2.11.2 Second Level Trigger 50

Chapter 3 Data Reconstruction, Analysis Algorithm And Skim 51
3.1 MWPC Tracking 52
3.1.1 Microstrip Track Reconstruction 53
3.1.2 PWC Track Reconstruction 53
3.1.3 Linking of SSD and PWC tracks 55
3.1.4 Vertex Reconstruction 55
3.1.5 Momentum Determination 58
3.2 Čerenkov Identification Algorithm 59
3.2.1 The CITADL Algorithm 59
3.2.2 CITADL Performance 64
3.3 Vee Reconstruction 73
3.3.1 SSD Vees 73
3.3.2 MIC Vees 73
3.3.3 M1 Vees 74
3.4 Data Reconstruction and Skims 75
3.4.1 Pass1 75
3.4.2 Skim1 75
3.4.3 Skim2 76

Chapter 4 The $D^+, D_s^+ \to K^+K^-\pi^+$ Dalitz Analysis 78
4.1 The $D^+, D_s^+ \to K^+K^-\pi^+$ Signal 79
4.2 The D^+ and $D_s^+ \to K^+K^-\pi^+$ Analysis Formalism 83
4.2.1 Background Parameterization 87
4.2.2 Efficiency Correction 91
4.3 Fit Results 95
4.3.1 Fit Results for $D^+ \to K^+K^-\pi^+$ 96
4.3.2 Fit Results for $D_s^+ \to K^+K^-\pi^+$ 108

Chapter 5 The $D^0 \to K_sK^+K^-$ Dalitz Analysis 113
5.1 The $D^0 \to K_sK^+K^-$ Cuts and Signal 114
5.2 The $D^0 \to K_sK^+K^-$ Dalitz Plot 118
5.3 The $D^0 \to K_sK^+K^-$ Fit Results 118
5.4 Can a pure $K_s\phi$ CP odd be obtained from $D^0 \to K_sK^+K^-$? 120

Chapter 6 Checking the Fidelity of the Fitting Technique 123
6.1 Introduction 123
6.2 Getting the parameter pulls 125
6.2.1 The mini-Monte Carlo Technique 125
6.2.2 D^+ Pulls 130
6.2.3 D_s^+ Pulls 133
6.2.4 D^0 Pulls 136

Chapter 7 Estimating Systematic Errors 140
7.1 $D^+ \to K^+K^-\pi^+$ Systematics 141
7.2 $D_s^+ \to K^+K^-\pi^+$ Systematics 151
7.3 $D^0 \to K_s^o K^-K^+$ Systematics 152

Chapter 8 Summary and Conclusions 166
8.1 Summary on $D^+, D_s^+ \to K^-K^+\pi^+$ 166
8.2 Summary on $D^0 \to K_s^o K^-K^+$ 170
8.3 What we would do differently 175
8.4 Future Charm Dalitz Analysis Physics 179

Appendix A Glossary of Terms 182

References 186

Vita 189

List of Figures

1.1 The spectator diagrams present for the decay D^0 5
1.2 BSW model 8
1.3 BSW diagrams 9
1.4 Dalitz 3-D plot of D^+ 12
1.5 Feynman-like diagram for the process $D_s^+ \to \phi\pi^+$ 13
1.6 Sign of interference term 15
1.7 Three mechanisms for $D_s \to \pi^+\pi^-\pi^+$ 18

2.1 Proton production facilities 25
2.2 Proton beam line 26
2.3 Wideband photon beam line schematic 27
2.4 Target region and SSD configuration 31
2.5 Z distribution for the primary and secondary vertices 33
2.6 PWC orientation looking down stream 35
2.7 FOCUS spectrometer 37
2.8 C1, C2 and C3 cell structure 42
2.9 C1 side and top views 42
2.10 C1 schematic 43
2.11 HC schematics 45
2.12 Inner Muon array schematics 47
2.13 $H \times V$ and OH schematic 49

3.1 Schematic representation of isolation cuts Cl1 and CL2 57
3.2 The fraction that a C2 cell fires when with detected track 64
3.3 Fraction of times that a pion is misidentified 65
3.4 The fraction of times that a proton is misidentified 66
3.5 Invariant mass plot for three golden mode decays 66
3.6 The log likelihood difference $W_\pi - W_K$ distribution 67
3.7 Illustration of the effectiveness of Čerenkov cuts 70
3.8 E687 signal for $D^0 \to \pi^+\pi^-$ 71
3.9 Illustration of the effectiveness of Čerenkov cuts 72

4.1 Effect primary isolation (CL1) cut 80
4.2 Signal development plot for D_s^+ 81
4.3 Mass histograms of full data set for D^+ 82
4.4 The 3-D dalitz plot of the low sideband 89

4.5 Low sideband Dalitz plots and projections for D^+ 90
4.6 The 3-D dalitz plot of the high sideband. 91
4.7 High sideband Dalitz plots and projections for D_s^+ 92
4.8 Phase space Monte Carlo signals and statistics 93
4.9 D^+ and D_s^+ efficiency plots 94
4.10 The D^+ binned efficiency plot. 95
4.11 The D^+ signal and yield. 97
4.12 Dalitz plot of D^+ 100
4.13 The $K^-\pi^+$ projections of D^+ 101
4.14 The $K^+\pi^+$ projections of D^+. 102
4.15 The D^+ projections (a) 104
4.16 The D^+ projections (b) 105
4.17 The D^+ projections (c) 106
4.18 Bin by bin contribution to the χ^2 for the D^+ 107
4.19 The D_s^+ signal and yield. 108
4.20 Dalitz plot of D_s^+ 109
4.21 The D_s^+ projections 112

5.1 The D^0 signal 115
5.2 The D^0 Monte Carlo sample 116
5.3 Dalitz plot of D^0 117
5.4 The D^0 projection 119
5.5 The D^0 scatter plot 122

6.1 The signal region mini Monte Carlo simulation of D^+ 126
6.2 Low and high side band regions mini Monte Carlo 127
6.3 Simulated efficiency 129
6.4 D^+ fit parameter pulls 130
6.5 D^+ pulls on the four fit fractions. 131
6.6 D_s^+ fit parameter pulls 134
6.7 D_s^+ pulls five fit fractions. 135
6.8 D^0 fit parameter pulls 137
6.9 D^0 fit fraction pulls 137
6.10 D^0 fit fraction pulls in the ϕ region 139

7.1 The sum of the χ^2/D.o.F. 146
7.2 The signal fraction in the signal region 147
7.3 D^+ amplitude systematics. 148
7.4 D^+ phase systematics. 149
7.5 D^+ fit fraction systematics. 150
7.6 The D_s^+ sum of the χ^2/D.o.F. 152
7.7 The D_s^+ signal fraction in the signal region 154
7.8 D_s^+ amplitude systematics. 155
7.9 D_s^+ phase systematics. 156
7.10 D_s^+ fit fraction systematics. 157

7.11 The D^0 sum of the χ^2/D.o.F. 160
7.12 The D^0 signal fraction in the signal region 161
7.13 D^0 amplitude systematics 161
7.14 D^0 phase systematics. 162
7.15 D^0 fit fraction systematics. 163
7.16 D^0 χ^2/D.o.F. 164
7.17 D^0 χ^2/D.o.F. 165

8.1 Dalitz 3-D plot for D^+ and D_s^+ 170
8.2 Dalitz 3-D plot of $D^0 \to K_s K^+ K^-$. 176

List of Tables

1.1 , $(D^o \to K^+K^-)/, (D^o \to \pi^+\pi^-)$ 10
1.2 Isospin amplitude ratios and phase shifts for two body charm decays. 11

2.1 SSD specifications 33
2.2 PWC specifications 35
2.3 Čerenkov counter specifications 40
2.4 Particle identification momentum ranges 40

3.1 Super-stream Descriptions 76

4.1 D^+ and D_s^+ signal properties 82
4.2 Signal and Sideband Region Limits 83
4.3 D^+ Cuts 98
4.4 D^+ Fit Results 103
4.5 D_s^+ Cuts 109
4.6 D_s^+ Fit Results 111

5.1 $D^0 \to K_s K^+K^-$ signal properties 115
5.2 D^* tagged D^0 Cuts 116
5.3 non-tagged D^0 Cuts 117
5.4 D^0 Fit Results 120
5.5 fractions in the ϕ region 121

6.1 D^+ fit parameter pull statistics 132
6.2 D^+ fit fraction pull statistics 133
6.3 D_s^+ fit parameter pull statistics 136
6.4 D_s^+ fit fraction pull statistics 136
6.5 D^0 fit parameter pull statistics 138
6.6 D^0 fit fraction pull statistics 138
6.7 D^0 fit fraction pull statistics in the ϕ region $M^2_{K^+K^-} < 1.1$ 139

7.1 D^+ and D_s^+ cut variants 144
7.2 D^+ Errors 145
7.3 D_s^+ Errors 153
7.4 D^0 cuts variants. 159
7.5 D^0 Errors 159
7.6 ϕ region D^0 Errors ($M^2_{K^+K^-} < 1.1$) 160

7.7 ϕ region D^0 Errors ($1.034 < M^2_{K^+K^-} < 1.042$) 162

8.1 D^+ Fit Results 171
8.2 D_s^+ Fit Results 172
8.3 D^0 Fit Results 177

Chapter 1

Introduction

In this thesis we study the decay of mesons [1] containing a charm quark paired with either a $\bar{s}$, $\bar{d}$ or a $\bar{u}$ antiquark, into three meson final states. Specifically we examine the three decays D^+, $D_s^+ \rightarrow K^-K^+\pi^+$ and $D^0 \rightarrow K_s^o K^+K^-$. To a large extent, the thesis was motivated by an attempt to study $D^0 \rightarrow K_s^o K^+K^-$ both as a probe of the decay dynamics of this unusual decay, and to measure some important properties of this decay which bear on the topically interesting subject of CP eigenstate lifetimes. Both motivations will be described in depth later in this chapter. The other two decays, D^+, $D_s^+ \rightarrow K^-K^+\pi^+$, have been studied by our earlier experiment, E687, but with much less data. They primarily served as a means of "calibrating" our methodology.

Our principle analysis tool is the Dalitz plot. A Dalitz plot is a scatter plot of m_{ab}^2 versus m_{ac}^2 for the decay $D \rightarrow abc$. For the decay of a spinless D into three spin 0 mesons (abc), there are only two, non-trivial degrees of freedom which can describe the quantum mechanical amplitude of the decay. These can be chosen as the invariant mass between any 2 daughter combinations. If one choses the square of

[1] Strongly interacting particles made up of a quark and anti-quark, which have integral spin.

these masses, the resulting scatter plot has the important property that equal areas in the plot corresponds to equal volumes in the Lorenz Invariant Phase Space. Any deviations from a uniform distribution an (efficiency corrected) Dalitz scatter plot, indicates the presence of a non-constant amplitude. Interestingly enough, although three body charm particles were initially expected to have nearly constant amplitudes, it soon became apparent that nearly all three body decays were of the (quasi-two-body) form $D \to rc$, followed by $r \to ab$. The particles a,b and c represent $J^P = 0^-$ pseudoscalar mesons and r represent highly unstable mesons (called "resonances") with $J^P = 0^+, 1^-, 2^+, 3^-, ...$

The Dalitz plots is a great way of studying such quasi-two-body decays. For example if a resonance occurs between particles a and b for example, there will be an increased density of points in the band at the fixed M^2_{ab}. This band will have very visible nodes which disclose the spin of the resonance. The number of nodes gives the spin of the meson resonance. The Dalitz plot is bordered by a boundary by momentum conservation and the total energy available to the system [34]. In this thesis, we use likelihood techniques to fit the Dalitz scatterplot for these three decays to a probability density function described by an intensity constructed out of the interfering amplitudes representing the various quasi-two-body contributions.

This thesis presents the first amplitude analysis of the $D^0 \to K^o_s K^- K^+$ final state. There are two principle motivations for such a study. The $D^0 \to K^o_s K^- K^+$ final state appears to have a branching ratio consistent with a Cabibbo favored decay where a c-quark decays into an s-quark within the same quark generation. At quark level one would expect decay through a $c \to su\bar{d}$ transition, leading to a final state (at quark level) of the form $D^0 \equiv c\bar{u} \to (su\bar{d})\bar{u}$. But unlike the usual Cabibbo allowed decays such as $D^0 \to K^-\pi^+$, three kaons appear in the final state each with either an s or $\bar{s}$ quark. How are these additional strange and antistrange quarks produced?

Our second motivation involves the analysis of the lifetime for CP odd eigenstates. There are interesting and somewhat conflicting information from CLEO[20] and FOCUS[19] that there are surprisingly large flavor oscillations of the form $D^0 \leftrightarrow \bar{D}^0$. If this is correct and CP is approximately conserved in charm decay, one would expect that a CP even final state would have a different lifetime than a CP odd final state. FOCUS data indicates that the CP even K^-K^+ final state has a shorter lifetime than the CP mixed final state $D^0 \to K^-\pi^+$ by $(3.42 \pm 1.39 \pm 0.74)\%$. If so, one would expect an odd CP final state such as $D_s^+ \to \phi K_s^o$ to have a **longer** lifetime by about 3.42 %. The $D_s^+ \to \phi K_s^o$ final state is perhaps the most experimentally accessible CP odd[2] decay available to FOCUS and (perhaps) CLEO. We will show in this thesis that there is a strong $f_0(980)K_s^0$ contribution to $D^0 \to K^-K^+K_s^o$, which will produce CP **even**[3] contamination to the $D_s^+ \to \phi K_s^o$ process in the same region of the $D^0 \to K^-K^+K_s^o$ Dalitz plot. It is therefore of considerable, topical interest to assess the lavel of $f_0(980)K_s^o$ in the "ϕ" region of the $D^0 \to K^-K^+K_s^o$ Dalitz plot.

1.1 Review of Dalitz Analysis of Charm decay Phenomenology

In this section we review the existing known phenomenology of charm decay with a special emphasis on that phenomenology directly related to this thesis. This chapter will allow us to introduce many of the physics ideas necessary to understand this work and the techniques required to perform it. Much of the work is motivated by

[2] This final state is CP odd since the CP of the K_s^o and ϕ are both even, and to conserve angular momentum the $K_s^0\phi$ must be in an odd parity p-wave angular momentum state.

[3] Again the $f_0(980)$ and K_s^o are both CP even. This time they are in an even parity relative s-wave making the $f_0(980)K_s^o$ an even CP final state.

the desire to extend these studies to the decay mode considered here for the first time: $D^o \rightarrow \bar{K}_o K^+ K^-$.

1.1.1 Studies of non-leptonic charm decay

Perhaps the least understood aspect of charm decay physics is the physics of non-leptonic charm decay. Primarily this is due to the complexities of the strong interaction which makes it extremely difficult to reliably calculate the rate and properties of such decays. One of the clearest demonstrations underlying complexity of this subject is the rough order of magnitude difference between the lifetimes of the seven long-lived, singly charmed mesons or baryons which consist of a single charmed quark and either two or three light (u,d,s) quarks. This vast disparity in lifetimes primarily reflects differences in the non-leptonic decay width since the semileptonic width is a small fraction of the total width and are expected and measured to be roughly the same among charm species. What is astonishing is that the primary way such states decay is that the charm quark decays, a strange quark is created and yet the light quarks do not play a passive role (as is the case for beauty) but actively modify the rate by a huge factor.

There are several ways of studying non-leptonic charm decays. The most inclusive way is through the precise measurements of charm particle lifetime. On a less inclusive level, one can study the partial decay widths of charm mesons into specific two body, non-leptonic final states. Much of the rich phenomenology of non-leptonic decays can be explained and organized by a model which we will call *factorization*. The factorization model concerns so-called spectator decays where the light quark found along with the charm quark plays a rather minimal (spectator role) in the decay of the charm particle. Examples of spectator and non-spectator charm decays are

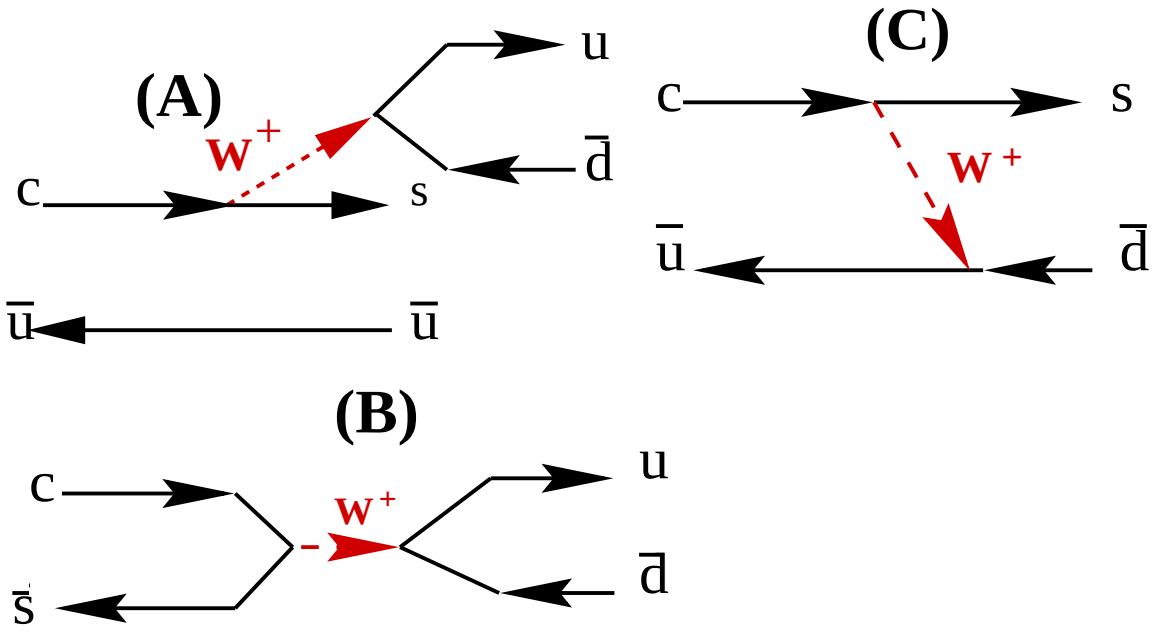

Figure 1.1: Figure A shows one of the spectator diagrams present for the decay D^0 . Figure B shows a non-spectator process called **weak annihilation** which is possibly present in the decay D_s^+. Figure C shows a non-spectator process called **weak exchange** which might be present in the decay of the D^o.

illustrated in Figure 1.1.

Factorization models predict the partial decay widths of two body decays of charmed mesons in the absence of final state interactions which describes subsequent strong re-scattering of the final state mesons after they are produced from the initial charm decay. The simplest experimental tests of factorization involve comparing the pure two body decays of charmed mesons into two pseudoscalar final states involving kaons and pions. Final state interaction effects become apparent in the interference between the various isospin amplitudes which contribute to different charged variants of a given final state which would have to have relatively real phases in the absence of such interactions.

One can extend factorization tests to quasi-two body decays such as pseudoscalar - vector decays by analyzing the resonance structure in multibody, nonleptonic,

charmed meson decays. These amplitude analyzes provide additional handles on final state interaction effects through interference of the amplitudes describing competing resonant channels in *eg* a three particle decay Dalitz plot. Comparing the decay "widths" into various resonant channels in different charge states allows one to extend the isospin decomposition to quasi-two-body final states as well as two body states. It is often found that the various resonant amplitudes have relatively imaginary phases which again underscores the importance of final state interactions and provides a unique data to study these effects.

In addition to pinning down the parameters of factorization models, Dalitz analyzes have often been used to explicitly search for the presence of the sort of non-spectator processes illustrated in Figure 1.1. Often such processes such as weak annihilation are expected to produce three body non-resonant contributions to the Dalitz plot that (in isolation) would produce a relatively uniform Dalitz scatter plot.

1.2 Previous Dalitz Analyzes

Several groups in the past have performed the types of high statistics, coherent amplitude analyzes discussed here. These include the Mark 3 Collaboration[6], the ARGUS Collaboration[7], and E687[35]. In addition groups have presented informal, resonant analyzes of three body final states which have played important roles in elucidating the physics discussed in this thesis[39]. In this section we will attempt to further motivate why such studies are interesting and summarize much of the information which is already known about hadronic charm decay using the Dalitz analysis technique.

Many previous analyzes have concentrated on determining the fit fractions or the fraction of decays which proceed via a particular resonance channel.Often [1] these fit fractions are used to producing the equivalent of "branching fractions" or decay

widths for quasi-two-body final statues which can then be compared to specific model for charm hadronic decay such as the BSW[23] factorization model. [4]

1.2.1 Factorization Models

The factorization framework, in which non-leptonic charm decays have been traditionally analyzed, begins with an effective Hamiltonian such as that given by Equation. 1.1 describing CKM allowed decays:

$$\mathcal{H} = \frac{G_f}{\sqrt{2}} V_{cs}^* V_{ud} \left(\frac{C_+ + C_-}{2} (\ \bar{u}\ d)\ (\bar{s}\ c\ ) \ + \ \frac{C_+ - C_-}{2} (\ \bar{s}\ d)\ (\ \bar{u}\ c) \right) \tag{1.1}$$

The Hamiltonian of Equation. 1.1 incorporates QCD corrections to the underlying weak decay process through the use of renormalization group methods. The coefficients $C_\pm$ are called "Wilson coefficients". In the absence of QCD corrections , $C_+ = C_-$ and one recovers single weak process corresponding to the familiar external "W" spectator diagram where a $c \to sW^+ \to su\bar{d}$. The Wilson coefficients depend on the scale of the QCD coupling constants. When taken at the charmed quark mass , the Wilson coefficients have the values given by Eqn. 1.2.

$$\frac{C_+(M_Q) + C_-(M_Q)}{2} \approx 1.25 \quad , \quad \frac{C_+(M_Q) - C_-(M_Q)}{2} \approx -0.49 \tag{1.2}$$

In 1987 , Bauer, Stech, and Wirbel (BSW) [23] combined these ideas into an explicit model applied two body and quasi-two body non-leptonic charmed meson decay. In

[4] Given the large degree of interference present in many Dalitz plots, such resonance contributions should be properly described by quantum mechanical ***amplitudes*** rather than fit fractions which represent fractional ***intensities***. Unfortunately fit fractions have become a ***de facto*** convention to describe the relative strength of resonant contributions. Although fit fractions are misleading, they is not a terrible way of specifying this information since the amplitudes can be determined from fit fractions, and phases. Fit fractions have an advantage in that are invariant with respect to the particular normalization, and internal conventions used by a given group.

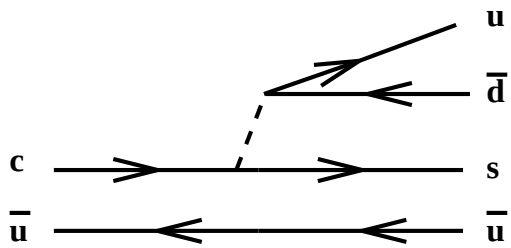

Figure 1.2: In the BSW model the amplitude for this decay is written as $a_1\ G_f\ 2^{-1/2}\ < \pi^+|(\bar{u}d)|0 >< K^-|(\bar{s}c)|D^o >= a_1\ G_f\ 2^{-1/2}\ (-if_\pi P_\pi) \times f_+(m_\pi^2)$. The coupling of the π^+ with respect to the virtual W^+ involves the same current as the leptonic decay $\pi^+ \to \ell^+\nu$ which is proportional to the pion lepton decay constant. The CKM allowed current which describes the process $D^o \to W^{+*}\ K^-$ is the same current involved in the semileptonic decay process $D^o \to K^-\ell^+\nu$ which is described by the form factor $f_+(q^2)$.

the BSW model, the two terms of Eqn. 1.1 are organized into an effective "charged" current and effective "neutral current" between the parent and daughter hadrons. The first term with an amplitude, $a_1 \approx (C_+ + C_-)/2$ (with a small color correction), describes the familiar spectator process. The effective neutral current process with an amplitude $a_2 \approx (C_+ - C_-)/2$ will decrease as $M_Q \to \infty$ gives rise to additional effects which are important in charm but less so in beauty. If a given non-leptonic charm decay can only proceed through the effective charged current interaction, it is classified as a Class 1 process. Class 2 processes only proceed through the effective neutral current interactions. Class 3 processes have contribution from both interactions. In the process, $D^o \to K^-\pi^+$,illustrated by Figure 1.2 , one has a neutral parent and two charged daughters and hence this must be a Class 1 process. In the Class 2 process, $D^o \to \bar{K}^o\pi^o$, one has neutral parent D^o decaying into two neutral daughters. The CKM allowed decays of the D^+ such as $D^+ \to \bar{K}^o\pi^+$, depicted in Figure 1.3, are Class 3 processes.

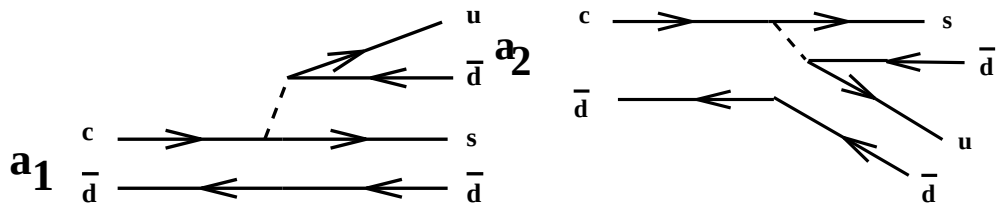

Figure 1.3: The two processes depicted in the figure differ by the exchange of $\bar{d}$ quark fermion in the final state. Because a_1 and a_2 interfere with the opposite sign one generally has destructive interference for D^+ decays which causes the D^+ to have a longer life than the D^o.

Watson's Theorem

According to the Watson theorem, the weak amplitudes predicted in factorization models such as BSW must all be relatively real. However, the final state hadrons can continue to interact via long range strong interactions and acquire complex phases. These final state interactions (FSI) can be accommodated by multiplying the bare (weak) amplitudes by the square root of a complex, unitary S matrix describing the strong rescattering. To illustrate the effects of FSI consider the isospin classification of three amplitudes related to $D \to \pi\pi$ decay:

$$A(D^o \to \pi^-\pi^+) = \frac{1}{\sqrt{3}}\left(\sqrt{2}\, a_o + a_2\right)$$

$$A(D^o \to \pi^o\pi^o) = \frac{1}{\sqrt{3}}\left(-a_o + \sqrt{2}\, a_2\right) \quad , \quad A(D^+ \to \pi^o\pi^+) = \sqrt{\frac{3}{2}}\, a_2 \tag{1.3}$$

The measured a_o and a_2 amplitudes will acquire complex phases through the FSI S-matrix as indicated in Eqn. 1.4.

$$\begin{pmatrix} a_0 \\ a_2 \end{pmatrix} = \begin{pmatrix} \eta\ e^{2i\delta_0} & i\sqrt{1-\eta^2}e^{i(\delta_0+\delta_2)} \\ i\sqrt{1-\eta^2}e^{i(\delta_0+\delta_2)} & \eta\ e^{2i\delta_2} \end{pmatrix}^{1/2} \begin{pmatrix} a_0 \\ a_2 \end{pmatrix}_{\text{bare}} \tag{1.4}$$

Since QCD respects isospin symmetry, there should be no mixing between a_o and a_2 which means the elasticity parameter in Eqn. 1.4 should be $\eta = 1$.[5] Even a

[5] One can still have , however, inelastic final state interactions between final states such as $D \to \pi\pi$ and $D \to KK$ since a dipion final state can potentially scatter into a dikaon final state. One could

purely elastic FSI can change the total width of charm decays into a particular final state by changing the value of $\cos(\delta_2 - \delta_0)$ when converting *eg* $A(D^o \to \pi^-\pi^+)$ into $,(D^o \to \pi^-\pi^+)$ via Eqn. 1.5.

$$,(\pi^+\pi^-) = \frac{2}{3}\ |a_o|^2 + \frac{1}{3}\ |a_2|^2 + \frac{2\sqrt{2}}{3}|a_o|\ |a_2|\ \cos(\delta_2 - \delta_0) \tag{1.5}$$

The unexpectedly large branching ratio for the decay $D^o \to K^+K^-/\pi^+\pi^-$ provided an early example of the possible role of FSI affecting branching ratios. Table 1.1 summarizes recent data on $,(K^+K^-)/,(\pi^+\pi^-)$. As one can see from Table 1.1 ,

Table 1.1: $,(D^o \to K^+K^-)/,(D^o \to \pi^+\pi^-)$

E687[24]	WA82[25]
$2.53 \pm 0.46 \pm 0.19$	$2.23 \pm 0.81 \pm 0.46$
E691 [26]	CLEO[28]
$1.95 \pm 0.34 \pm 0.22$	$2.35 \pm 0.37 \pm 0.28$

although both processes are CKM suppressed by the same amount and $D^o \to \pi^+\pi^-$ is favored by having a larger phase space, $D^o \to K^+K^-$ occurs at roughly twice the rate as $D^o \to \pi^+\pi^-$. Since these decays were the first CKM suppressed decays to be studied, their width ratio was initially quite surprising. In the context of the BSW model, both decays are Class 1 processes, since no effective neutral currents are possible between the parent and either daughter, and the BSW model makes the prediction $,(K^+K^-)/,(\pi^+\pi^-) \approx 1.4$ independent of the value of a_2/a_1. Conventional wisdom has it that discrepancy between the data and the BSW prediction is due to FSI changing the phase of interfering dipion or dikaon isospin amplitudes.

accommodate such a case with a 4×4 matrix describing the two isospin amplitudes for the dipion and two isospin amplitudes for the dikaon.

A more direct way of seeing the effects of final state interactions is to measure the widths into various isospin related channels such as , $(\pi^+\pi^-)$, , $(\pi^o\pi^o)$, , $(\pi^+\pi^o)$ and extract a_0 , a_2, and $\cos(\delta_2 - \delta_0)$ by solving the Eqn. 1.5 and the two similar equations. Table 1.2 taken from the Annual Review article by Pedrini,Browder, and Honschied[29] summarizes the results of such isospin analyzes for many two body and quasi-two body charm decays. Table 1.2 shows that more often than not,

Table 1.2: Isospin amplitude ratios and phase shifts for two body charm decays.

Mode	Ratio of amplitudes	$\delta = \delta_I - \delta_{I'}$
$K\pi$	$\lvert A_{1/2}\rvert/\lvert A_{3/2}\rvert = 3.86 \pm 0.20$	$90^\circ \pm 6^\circ$
$K^\star\pi$	$\lvert A_{1/2}\rvert/\lvert A_{3/2}\rvert = 5.59 \pm 0.35$	$104^\circ \pm 14^\circ$
$K\rho$	$\lvert A_{1/2}\rvert/\lvert A_{3/2}\rvert = 3.59 \pm 0.75$	$0^\circ \pm 28^\circ$
$K^\star\rho$	$\lvert A_{1/2}\rvert/\lvert A_{3/2}\rvert = 5.12 \pm 1.97$	$33^\circ \pm 57^\circ$
KK	$\lvert A_1\rvert/\lvert A_0\rvert = 0.57 \pm 0.06$	$51^\circ \pm 9^\circ$
$\pi\pi$	$\lvert A_2\rvert/\lvert A_0\rvert = 0.63 \pm 0.13$	$80^\circ \pm 10^\circ$

a considerable phase shift is observed between the two isospin amplitudes. Watson's theorem tells us that phase shifts between interfering isospin amplitudes where $\sin(\delta_{I'} - \delta_I) \neq 0$ cannot arise from the weak processes alone and thus constitutes direct evidence for FSI.

1.2.2 Dalitz Analyzes

Several groups [6]−[35] have gone a step further and published resonant amplitude analyzes of particular final states. Most of this work concerns three body decays where all of the amplitude information resides in the Dalitz plot. Amplitude analyzes allow one to extend factorization model tests to pseudoscalar-vector and vector-vector

non-leptonic decays of D mesons and provide new ways of studying FSI effects. A particularly clean and instructive example is provided by the E687[35] group's analysis of the D^+ , $D_s^+ \rightarrow K^-K^+\pi^+$ final state. Since we will perform a similar analysis in this thesis, we will use FOCUS data to illustrate all of these ideas. The D_s^+ Dalitz plot is dominated by the $\phi\pi^+$ and $\bar{K}^{o*}K^+$ channels; while the D^+ also has a significant contribution from a single or multiple broad resonances. In order to extract information from Dalitz plots such as those illustrated in Figure 1.4, the experimental groups fit the intensity across Dalitz plot to a coherent sum of quasi-two body or possible non-resonant contributions. For example, one can fit the D_s^+ Dalitz plot to the form $d, /(dM_1^2 dM_2^2) \propto |\mathcal{A}(D_s^+ \rightarrow K^+K^-\pi^+)|^2$ where the amplitude is given by Eqn. 1.6.

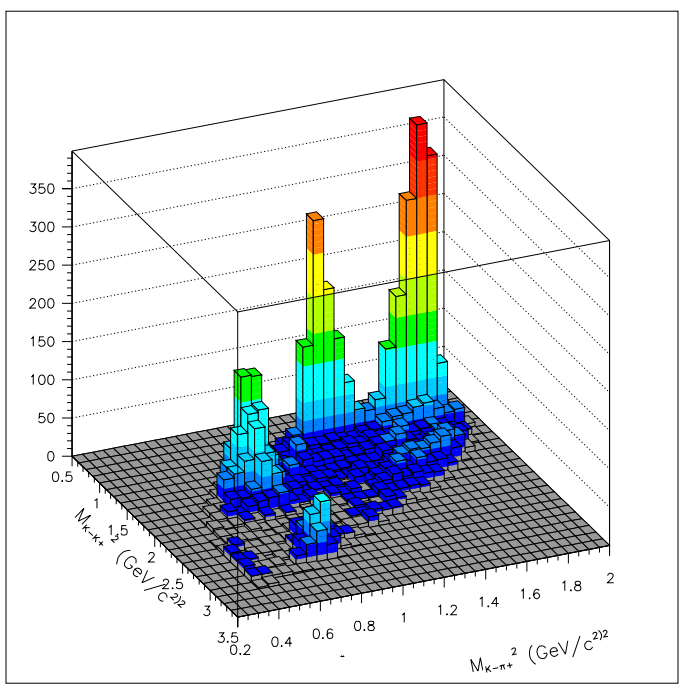

Figure 1.4: Dalitz 3-D plot of $D^+ \rightarrow K^+K^-\pi^+$. The Dalitz plot is dominated by ϕ and $\bar{K}^*(890)$ resonances. The asymmetry in the $\bar{K}^*(890)$ peaks is due to interference with the broader resonance $K^*(1430)$.

$$\mathcal{A}(D_s^+ \to K^+K^-\pi^+) = a_{\bar{K}^*}\ e^{i\delta_{\bar{K}^*}}\mathcal{M}(\pi^+K^-K^+|\bar{K}^{*o}\ K^+)$$
$$+a_\phi\ e^{i\delta_\phi}\mathcal{M}(K^+K^-\pi^+|\phi\pi^+) + ... \qquad (1.6)$$

Figure 1.5 illustrates the form of one of these quasi-two body contributions. Each

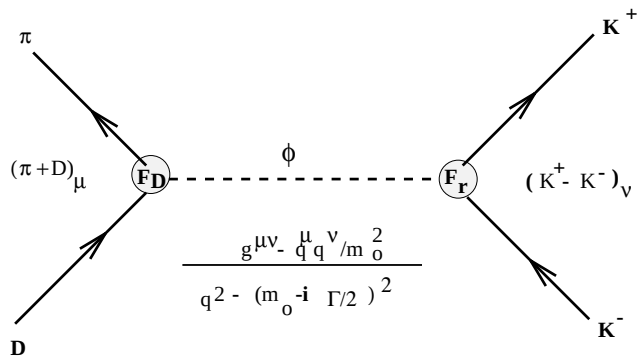

Figure 1.5: We show a Feynman-like diagram for the process $D_s^+ \to \phi\pi^+$. A $D \to \pi^+$ current with a form factor F_D interacts with a kaon current with form factor F_r through an unstable ϕ propagator with an imaginary width contribution to the propagator mass. This diagram gives an amplitude contribution of the form $\mathcal{M} = F_D\ F_r\ \times\ |\vec{c}|^J|\vec{a}|^J P_J(\cos\theta^r_{ac})\ \times\ BW(m_{ab})$ where the angular factor which gives rise to the Dalitz nodes follows from the structure of current $\times$ current contribution, and the Breit-Wigner represents the unstable propagator. The form factors are relatively unimportant.

resonant channel contribution is multiplied by a complex amplitude coefficient whose modulus serves as a gauge to the relative "importance" of the channel.[1]

Any non-real phase differences are due to the influence of final state interactions which in a two resonant model would be given by Eqn. 1.7

$$\begin{pmatrix} a_{\bar{K}^*}\ e^{i\delta_{\bar{K}^*}} \\ a_\phi\ e^{i\delta_\phi} \end{pmatrix} = \begin{pmatrix} \eta\ e^{2i\delta_1} & i\sqrt{1-\eta^2}e^{i(\delta_1+\delta_2)} \\ i\sqrt{1-\eta^2}e^{i(\delta_1+\delta_2)} & \eta\ e^{2i\delta_2} \end{pmatrix}^{1/2} \begin{pmatrix} a_{K^*} \\ a_\phi \end{pmatrix}_{\text{bare}} \qquad (1.7)$$

[1]In fitting to the shape of the relative event density across the Dalitz plot, one of the fitted amplitude factors is generally set to unity and serves as a reference channel. Clearly since one is fitting to $|\mathcal{A}|^2$ the overall phase of $\mathcal{A}$ cannot be measured. The modulus of the reference amplitude can be determined if desired through the total decay width and the partial branching fraction into the given state.

One of the more interesting features of the Dalitz plots of Figure 1.4 is the pronounced asymmetry between the two $\bar{K}^*$ lobes for the $D^+ \rightarrow K^- K^+ \pi^+$. We believe that this lobe asymmetry is due to interference of the $\bar{K}^{*o} K^+$ channel with a broad, spinless resonance channel. From the interference pattern, one can infer that the data requires a nearly imaginary relative phase shift. We present this argument for the relative phase shift. For simplicity, we model the broad resonance in the vicinity of the $\bar{K}^*$ as a nearly constant amplitude which we write as $\cos\ \delta + i \sin\ \delta$. Eqn. 1.8 gives an explicit form for this interference term.

$$Re\left\{(\cos\ \delta + i \sin\ \delta)^* \ \frac{\cos\ \theta}{M_r^2 - M_{K\pi}^2 - i,\ M_r}\right\} =$$
$$\frac{(M_r^2 - M_{K\pi}^2)\ \cos\ \theta\ \cos\ \delta}{(M_r^2 - M_{K\pi}^2)^2 + ,^2 M_r^2} + \frac{,\ M_r\ \cos\ \theta\ sin\ \delta}{(M_r^2 - M_{K\pi}^2)^2 + ,^2 M_r^2} \tag{1.8}$$

The asymmetry comes about because the $\bar{K}^{o*} K^+$ decay amplitude contains an angular factor of $\cos\theta$, where θ is the angle between the two kaons in the $\bar{K}^{o*}$ rest frame. This $\cos\theta$ factor causes the interference term to change sign from the left lobe to the right lobe. We get an interference term from both the real part of the Breit-Wigner as well as the imaginary part. Since the real part of a Breit-Wigner reverses sign as one passes through the resonance (thus canceling the net interference across the lobe), any net interference is due to the second term which is proportional to $\sin\delta$. Figure 1.6 makes this argument graphically. The net lobe asymmetry thus provides visible evidence for final state interactions since all bare amplitudes must be real ($\delta = 0$ or 180°). After exploring many possibilities, E687 settled on the $\bar{K}_0^*(1430)^0\ K^+$ channel as the most likely channel interfering with the $\bar{K}^{*0} K^+$ band. Several groups have performed Dalitz analyzes for the $D^o, D^+ \rightarrow K\pi\pi$ final state. Although these fits provide a good qualitative match to the data, often discrepancies are apparent in comparisons between the data and mass projections. This will especially be true given the much larger statistics data present in my thesis.

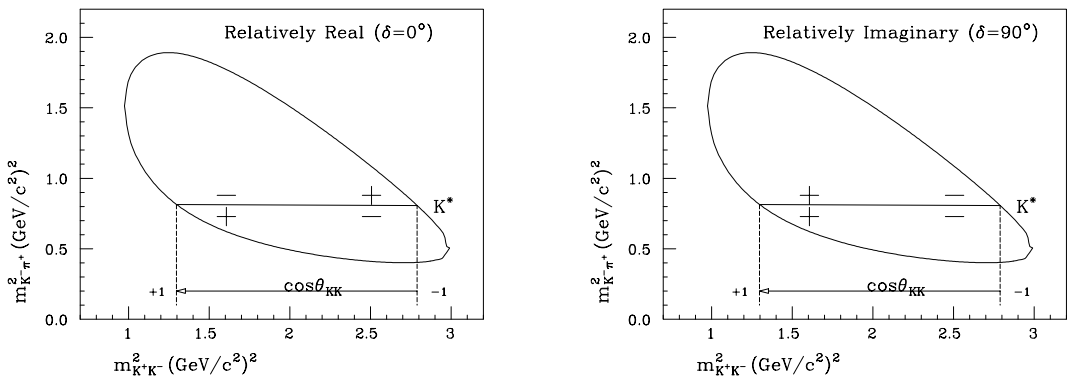

Figure 1.6: The "+" and "-" indicates the sign of the interference term between a constant phase and the $\bar{K}^{o*}K^{+}$ Dalitz band for the case of relatively real (left) and relatively imaginary (right) phase shift. The sign alternates from the left to the right of the band owing to the $\cos\theta$ portion of the $\bar{K}^{o*}$ amplitude in Eqn. 1.8. The real part of a Breit-Wigner amplitude reverses sign as one passes through the resonance which implies an additional sign change for the relatively real case. The relatively imaginary part has no such additional sign reversal.

Previous Dalitz analyzes have provided a wealth of information on new decay modes which can be compared to models based on factorization, QCD sum rules, and $1/N_c$ expansions. Generally agreement of the models with the data is only at about the ± 60 % level. Often the isospin amplitudes show nearly imaginary relative phases as reported in Table 1.2. It is interesting to note that all experimental groups report a sizeable non-resonant contribution to the $D^+ \to K^-\pi^+\pi^+$ Dalitz plot which makes it unique among the plots discussed here.

1.2.3 Motivation for the principle study of this thesis

The principle result of this thesis is the first coherent Dalitz analysis of the decay $D^o \to \bar{K}_o K^+ K^-$. There are two principle motivations for this study. The first motivation is to understand the dynamics of this unusual decay. What makes this process unusual is that it is a Cabibbo allowed process which generally produces a single final state strange quark in the final state. However, the $\bar{K}_o K^+ K^-$ has three strange (or antistrange) quarks in the final state. Where did they all come from?

A similar decay is $D_s^+ \to \pi^+\pi^-\pi^+$. This is also a Cabibbo favored decay which generally produces both an s and $\bar{s}$ quark in the final state. However the $\pi^+\pi^-\pi^+$ final state has no s or $\bar{s}$ quarks. Where did they go? Although a natural answer to this question is the weak annihilation process shown in Figure 1.1, experimentally the answer is quite different and very interesting as discussed in the next section. The experimental data strongly supports the Class 1 factorization process but one involving highly unusual resonances with simultaneous couplings to up-down and $s\bar{s}$ quarks. We will demonstrate that a very similar mechanism is at work for $D^0 \to \bar{K}^0 K^- K^+$.

A second motivation involves the flavor oscillation of a $D^o \to \bar{D}^o$. If this mixing

were to occur through a CP conserving process, the mass matrix eigenstates would be CP even and CP eigenstates such as $D_{1,2} = (D^o \pm \bar{D}^o)/\sqrt{2}$. These states, rather than the D^o or $\bar{D}^o$, would have unique lifetimes. At present there is some exciting but weak and very contradictory evidence from both CLEO and FOCUS that suggests that the D^o are able to mix into $\bar{D}^o$ primarily through the difference of their decay widths rather than their masses.[2] In the case of FOCUS, the evidence was the direct measurement of a lifetime difference between $D^o \to K^+K^-$ which is a pure CP even state and $D^o \to K^-\pi^+$ which is a mixed CP state by about 3.5%. A possible way of further testing this result would be to measure the lifetime of the $D^o \to \bar{K}_o\phi$ where the ϕ subsequently decays via $\phi \to K^+K^-$. It is easy to show that such a final state has odd CP. However there is an open question as to how much $D^o \to \bar{K}_o K^+K^-$ final state with the dikaon in the vicinity of the ϕ is actually due to CP odd final states such as $D^o \to \bar{K}_o\phi$ and how much is from CP even final states such as $D^o \to \bar{K}_o f_o$ or the interference of the two.

Much of my work on the $D^0 \to K_s^0 K^- K^+$ Dalitz plot was guided by an analysis of a related process $D_s^+ \to \pi^+\pi^-\pi^+$ which we summarize in the section below.

All pion decays of the D_s^+

Because the D_s^+ contains both a charm and anti-strange quark all pion decays obey the $\Delta C = \Delta S$ selection rule and are therefore Cabibbo favored. The most experimentally accessible decay would be $D_s^+ \to \pi^+\pi^-\pi^+$ which proceeds with a fairly large branching ratio $\mathcal{B}(\pi^+\pi^-\pi^+) = (1.4 \pm 0.4)\%$. [40]. Figure 1.7 illustrates three ways that such a decay might proceed. The first of the mechanisms, illustrated in Figure 1.7, involving a quasi-two-body spectator diagram, is very analogous to that of the

[2] The width can be thought of as the imaginary part of the unstable state's rest energy while the mass can be thought of as the real part of an unstable state's rest energy.

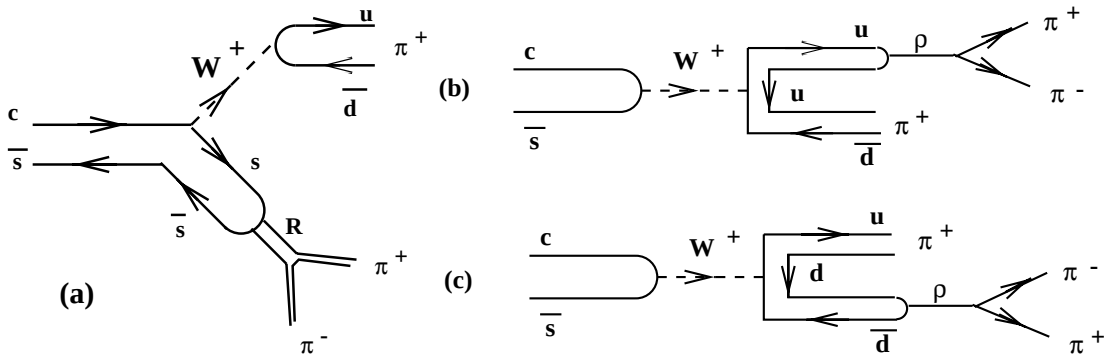

Figure 1.7: Three mechanisms for $D_s \to \pi^+\pi^-\pi^+$. (a) is a class 1 process involving a resonance "R" which must be formed from the initial $s\bar{s}$ quarks and decays to a final state dipion. (b) + (c) show two interfering annihilation contributions to $D_s^+ \to \rho_o\pi^+$.

well known $D_s^+ \to \phi\pi^+$ decay mode. The resonance "R" , however, is unusual since it must couple simultaneously an $s\bar{s}$ pair as well as to an all pion final state with no strange quarks. Searching the Particle Data Book [1] for established resonances with simultaneous dipion and dikaon decay modes, reduces the list to just two: the $f_o(980)$ with comparable dipion and dikaon branching fractions and the $f_2(1270)$ which decays 85% of the time into dipion and only 5% of the time into dikaon. One might therefore, reasonably expect $D_s^+ \to f_o(980)\pi^+$ to dominate the three pion decay of the D_s^+.

The remaining two processes, shown in Figure 1.7 are weak annihilation processes which are expected to be suppressed relative to the spectator process by a helicity violation argument (similar to the suppression of $\pi^+ \to e^+\nu$ relative to $\pi^+ \to \mu^+\nu$ but on the quark level). Recall that the near equality of the D_s^+ and D_o measured lifetimes also suggests that the WA contributions are significantly suppressed. In fact, a clear demonstration of the process $D_s^+ \to \rho\pi^+$ would constitute the first observation of a pure, weak annihilation process outside the fully leptonic process $D_s^+ \to \mu^+\nu$. Another possibility, not shown in Figure 1.7, is that the three pion final

state is created in a non-resonant final state via the weak annihilation process. It is very difficult to prove or stringently limit the existence of a non-resonant three body state with a nearly constant matrix element owing to the possibility that the apparent non-resonant state is actually a quasi-two-body state involving several broad resonant channels.

The interference between the (b) and (c) diagram of Figure 1.7 provides some interesting twists to this story. Anselmino, Bediaga, and Predazzi [42] recently pointed out that one might expect cancelation of (b) and (c) since the $u\bar{u}$ and $d\bar{d}$ contributions couplings to the spectroscopic wave function of the ρ have the opposite phase ($\rho \equiv (u\bar{u} - d\bar{d})/\sqrt{2}$). On the other hand, Lipkin [43] argues that this (-1) phase factor due to the couplings is offset by the (-1) brought about by the fact that the ρ and π^+ are exchanged in the two diagrams and yet are in an odd angular momentum state (relative P-wave). By this argument, Lipkin would conclude that the two diagrams constructively interfere and $D_s^+ \to \rho\pi^+$ might be a good place to look for WA contributions. Whatever the actual situation ($\rho\pi$ cancelation or constructive interference), the process $D_s^+ \to \omega\pi^+$ presumably interferes in the opposite fashion since $\omega \equiv (u\bar{u} + d\bar{d})/\sqrt{2}$.[3]

E687[45] completed the first, fully coherent, Dalitz analysis of the $D_s^+, D^+ \to \pi^+\pi^-\pi^+$ final state.

E687 was able to achieve reasonable fits to the $D^+ \to \pi^+\pi^-\pi^+$ Dalitz plot by including just a uniform non-resonant amplitude with a "decay fraction" of $77 \pm 5\%$ and a $\rho\pi^+$ amplitude with a "decay fraction" of $23 \pm 5\%$ and a relative phase of 36 ± 9°. By way of contrast, clear structure was evident in the $D_s^+ \to \pi^+\pi^-\pi^+$ plot. The most prominent feature of that plot is the "L-shaped" band just below

[3]Lipkin [43] argues that the cancelation expected for $D_s^+ \to \omega\pi^+$ is related to the fact that this decay , if it took place as shown in Figure 1.7 , would require a second class current to proceed.

$1GeV^2$ corresponding to $D_s^+ \rightarrow f_o(980)\pi^+$. As expected and previously observed[18], this resonance contribution with simultaneous dikaon and dipion couplings , strongly dominates the D_s^+ Dalitz plot.

In addition to the $f_o(980)$ "L", and $f_2(1270)\pi^+$ corners, there was strong evidence suggesting the presence of a scalar, dipion resonance with a mass near 1.5 GeV. E687 decided to assume that the horizontal band structure was due to a single Breit-Wigner resonance and varied the mass and width of this resonance (which they refer to as the $\mathcal{S}(1475)$) to maximize the likelihood of their fits. The mass and width of the $\mathcal{S}(1475)$ state are in excellent agreement with the $f_o(1500)$ entry in PDG96 [1]. The $f_o(1500)$ decays via modes such as $\eta\eta$ and $\pi\pi$ which (given the large strangeness content of the η) is consistent with a resonance with simultaneous couplings to strange quarks and pions. E687[45] found that the $D_s^+ \rightarrow \pi^+\pi^-\pi^+$ could be well fit by a mix of $f_o(980)\pi^+$ (decay fraction $85 \pm 7\%$) $\mathcal{S}(1475)\pi^+$ ($34 \pm 8\%$) and $f_2(1270)$ ($34 \pm 8\%$). The phases of the $\mathcal{S}(1475)\pi^+$ and $f_2(1270)$ amplitudes relative to the $f_o(980)\pi^+$ were 210 ± 10° and 83 ± 16° respectively.

E687 set a fairly stringent upper bound on the decay $D_s^+ \rightarrow \rho\pi^+$ of $\mathcal{B}(D_s^+ \rightarrow \rho\pi^+) < 0.09\%$ $(90\% CL)$ which is over 3 times better than the previously existing limit on this decay and significantly smaller 0.24 % which is the value computed by Buccella, Luisignola, and Pugliese[46] in a model where the $\rho\pi$ state can be generated via final state interactions. A somewhat loose upper bound of $\mathcal{B}(D_s^+ \rightarrow \pi^+\pi^+\pi^+(BR)) < 0.33\%$ $(90\% CL)$ was obtained for non-resonant decays but it is unclear what the true systematic error on this given the possibility of broad resonances mimicking or masking a true non-resonant contribution.

In this thesis we will apply a similar argument in our analysis of the $D^0 \rightarrow K_s^0 K^+ K^-$ process. We will show that $D^0 \rightarrow K_s^0 \rightarrow K^+K^-$ Dalitz plot is dominated by resonances which simultaneously couple to dipion and dikaons.

1.2.4 Summary

Here is a very brief summary of this rather lengthy section. A factorization framework , the Bauer Stech Wirbel (BSW) model, was designed to incorporate QCD corrections into non-leptonic decays. The BSW model deals specifically with 2 body and quasi-2 body decays. Predictions are made in terms of leptonic and semileptonic form factors. It has been known for some time that long range, final state interactions, FSI, can significantly distort BSW predictions for two body decay branching ratios. FSI is also responsible for creating complex phase shifts between isospin amplitudes. Amplitude analyzes have confirmed quasi-2 body nature of most three body decays. FSI effects are evident in the interference between resonant channels. Amplitude analyzes make possible vector-vector, and vector - pseudoscalar comparisons with BSW model. Only $\pm 60\%$ agreement exists between the models and resonance data.

Dalitz analyzes similar to those performed here have been motivated by the desire to further extend tests of factorization. Other motivations are to make detailed studies of non-spectator processes such as weak annihilation or weak exchange which could account for differences in charm particle lifetimes but have never been observed directly. This thesis is primarily concerned with the decay $D^o \rightarrow \bar{K}_o K^+ K^-$ which we will show involves a spectator mechanism involving unusual resonances. A similar mechanism is known to be at work in the analogous decay $D_s^o \rightarrow \pi^+ \pi^- \pi^0$. At present the decay $D^o \rightarrow \bar{K}_o \phi$ which is part of $D^o \rightarrow \bar{K}_o K^+ K^-$ is of great topical interest since it is conjectured that the $D^o \rightarrow \bar{K}_o \phi$ will have a substantially different lifetime than the decay $D^o \rightarrow K^+ K^-$. The Dalitz analysis presented here will be required to determine what fraction of the $D^o \rightarrow \bar{K}_o K^+ K^-$ final state is indeed a state of pure CP.

Chapter 2

The E831 Apparatus

In this chapter we review the E831 apparatus and beam line concentrating on those aspects which bear directly on the analysis presented in this thesis. The E831 experiment studies the production of charmed particles by high energy photons with wavelengths on the order of 1/500 the diameter of a proton. Photoproduction offers significant advantages in the study of charm physics over e^+e^- annihilation and hadroproduction. Charm physics was the principle goal of our experiment although there are interesting things to learn about the photoproduction process itself which tests perturbative QCD. Photoproduced charm is relatively clean with very few particles accompanying the charm-anticharm pair compared to hadroproduction. Ultimately this means a smaller data sample to reconstruct and study. Unlike charm studies at e^+e^- annihilation, the charm particle are produced at ultrarelativistic velocities. This means that the charm decay products are produced at very forward angles and our apparatus need only subtend the forward 100 miliradians. A relatively large fraction of the incident photon energy is given to the charm particles compared to hadroproduction of charm meaning acceptance tends to be greater. The high momentum of the charm particles allows us to very effectively separate them

from a very copious background of non-charm events[1] through their short but finite lifetime. The high momentum of the charm secondaries allows us to identify them using relatively inexpensive, conventional, gas , threshold Čerenkov counters.

2.1 Beam line

The FOCUS beam line is unique in the world since it is very high intensity, very high energy, and relatively free from neutral hadron contaminants such as K_ℓ^o's and neutrons.[2] The photon beam is classified as a *tertiary* beam since it is the result of three stages. In the first stage, 800 GeV protons at the rate of about 5×10^{12} per 40 second spill impinge on a liquid deuterium target and produce hadronic secondaries. The charged secondaries are swept out magnetically leaving the photon decay products of π^0's and η's. These photons are then converted to e^+e^- pairs which are transported about a neutral dump and then impinge upon a lead foil radiator. The photons that produce the charm for our experiment are from the bremsstrahlung of the converted e^+e^- pairs.

2.1.1 Proton Beam

In fixed target mode, the proton beam is extracted and sent down the fixed target beam line to the experimental areas through the following steps[12]:

- The Cockcroft-Walton provides the first stage of acceleration. Inside this device, electrons are added to hydrogen atoms. The resulting negative ions, each

[1] As a very crude guide, about 1/500 photons create hadronic final states as opposed to e^+e^- pairs and about 1% of the photohadronic cross section contains charmed particles.

[2] It is crucial to reduce such contaminants since they have roughly a factor of 100 larger cross section into hadronic final states than photons.

consisting of two electrons and one proton, are attracted to a positive voltage and accelerated to an energy of 750,000 electron volts. This is about thirty times the energy of the electron beam in a television's picture tube.

- After leaving the Cockcroft-Walton, negative hydrogen ions enter a linear accelerator called the Linac, which is approximately 500 feet long. Linac accelerator accelerates negative hydrogen ions from 750,000 electron volts to 400 million electron volts (MeV). The hydrogen ions pass through a thin carbon foil which strips off the electrons allowing for the protons to pass through. The protons are then injected into the Booster accelerator.

- Located nearly 20 feet below ground, the Booster is a rapid cycling synchrotron 500 feet in diameter. A synchrotron is a circular accelerator that uses magnets to bend electrically charged particles in a circular path so that they experience the repeated action of accelerating electric fields during each revolution. The protons travel around the Booster about 20,000 times and their energy is raised to eight billion electron volts ($8GeV$). The Booster normally cycles twelve times in rapid succession, loading twelve pulses, or bunches of protons, into the Main Ring, the next stage of the acceleration process.

- The Main Ring is another proton synchrotron which is four miles in circumference. A tunnel ten feet in diameter, buried 20 feet underground, house 1,000 conventional, copper-coiled magnets which continually bend and focus the protons. Under current operating modes, the Main Ring accelerates protons to 150 billion electron volts ($150GeV$).

- The same tunnel that houses the Main Ring also contains the 1,000 superconducting magnets which comprise the proton synchrotron known as the Teva-

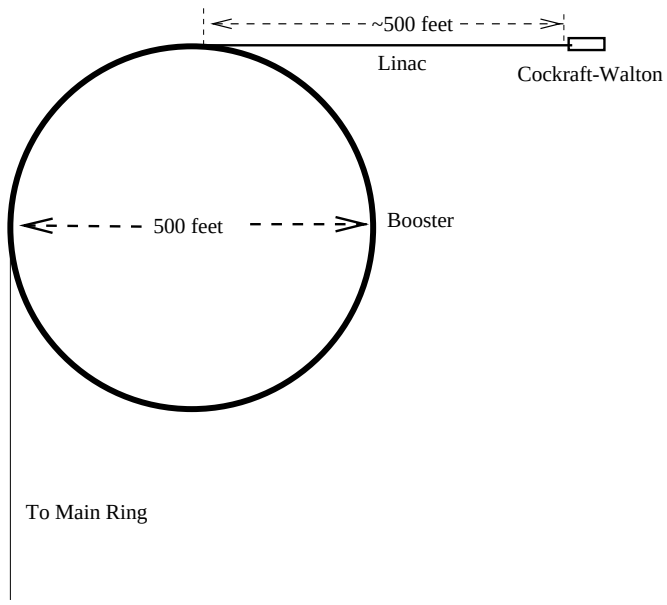

Figure 2.1: Proton production facilities. The hydrogen atoms are negatively ionized in Cockraft-Walton. They are accelerated through Linac and striped off the electrons. The protons are then injected into the Booster.

tron because of its ability to accelerate protons to nearly one trillion electron volts ($1TeV$). The super-conducting magnets form a ring directly below the Main Ring magnets and operate in the temperature range of liquid helium (-450^0F). Super-conducting magnets produce a larger magnetic field at a lower operating cost than conventional magnets. In the fixed target mode, the proton beam is extracted into the beam line and sent out to experiments in the fixed target area.

2.1.2 Photon Beam

In the fixed target mode, the proton beam is extracted into the beam lines and sent out to experiments in the fixed target area. To create photon beam the protons interact with a liquid deuterium target. At this stage the goal is to maximize the number of hadronic interactions producing π^o's and η's . The mean free path for

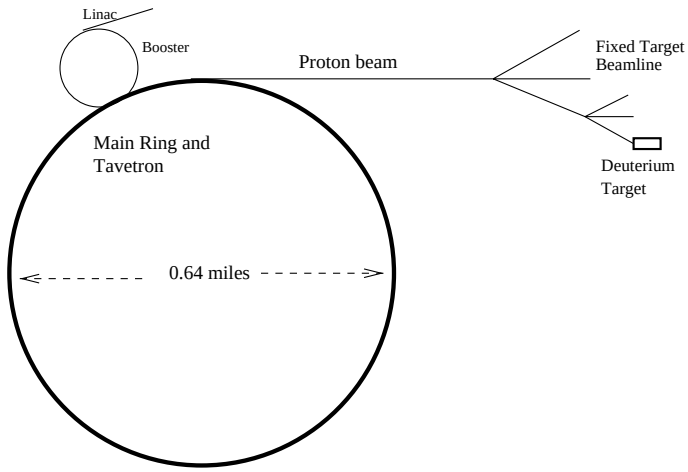

Figure 2.2: Proton beam line. The Main Ring accelerates the protons to $150\,GeV$, then injects them into the Tevatron. The Tevatron which contains 1000 super-conducting magnets, accelerates protons to $1\,TeV$ before the protons are diverted into the fixed target beam line.

π^0 and η production is given by the interaction length while the mean free path for photon absorption is given by the radiation length. Therefore the choice of the target material is based on maximizing the radiation length to interaction length ratio by maximizing the number of nucleons relative to the number of protons:

$$\frac{\sigma_{hadronic}}{\sigma_{electromagnetic}} \propto \frac{number\ of\ protons\ and\ neutrons\ (A)}{(number\ of\ protons\ (Z))^2} \tag{2.1}$$

The photons and other neutral hadrons impinge on a 60% radiation length lead foil which creates e^+e^- pairs. Lead with a very high absorption length to radiation length ratio is a good choice for this foil (called a converter) since it creates a copious supply of pairs while minimizing the unwanted hadronic interactions of the neutral hadron contaminants.

The converted e^+e^- pairs are transported around the very large neutral dump shown in Figure 2.3 using a beam line replete with magnets, collimators and beam tagging components which will be discussed shortly. The primary purpose for the double dog leg transport was to absorb neutral hadrons (such as neutrons , K_l^o's

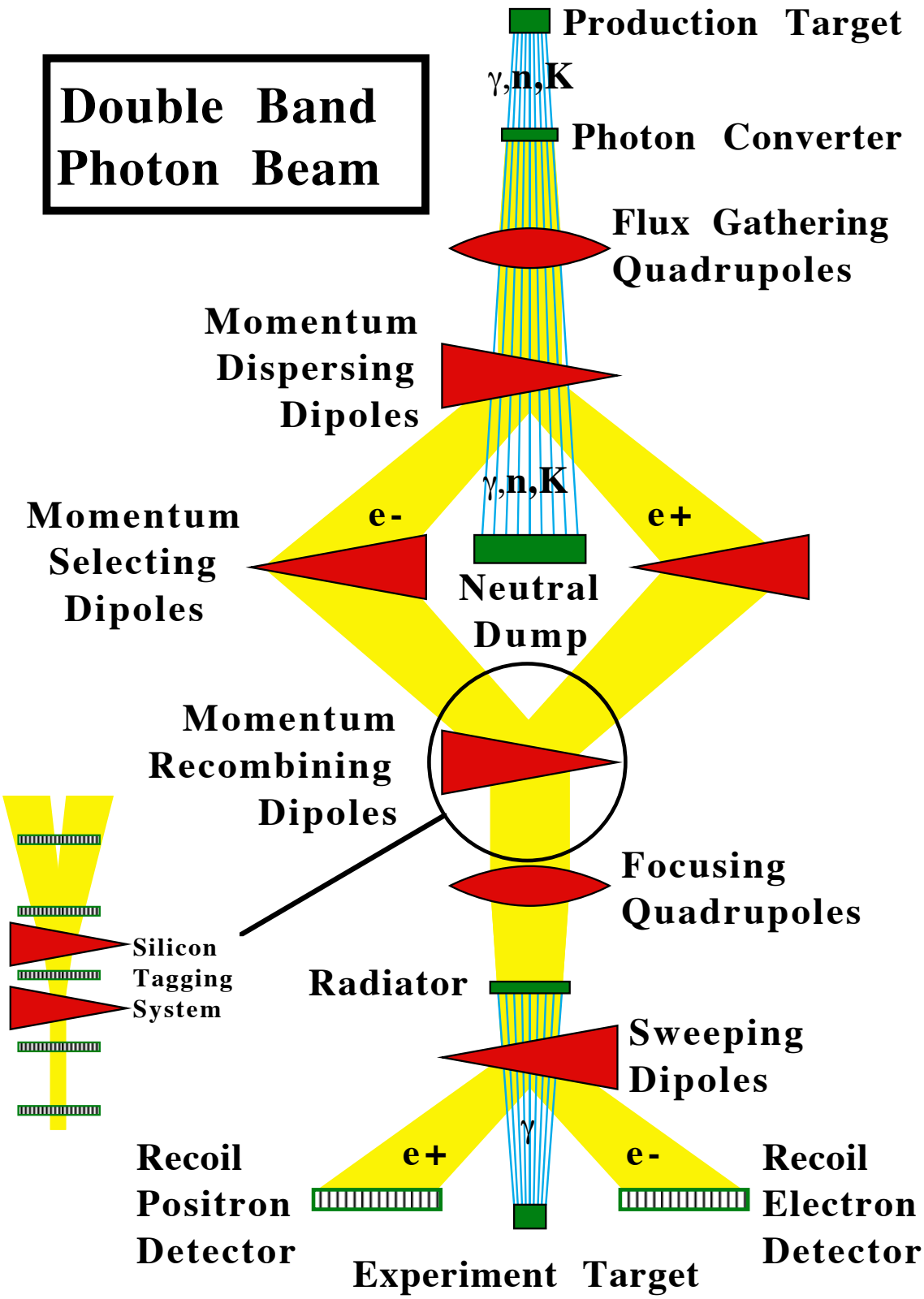

Figure 2.3: Wideband photon beam line schematic. On the lower left hand side a more detailed schematic for the tagging system is shown.

and Λ_o's) before they could interact in our experimental target. Neutral hadrons could form a serious background to the photon experiments that the experiment was designed to study since they have $\approx 100\times$ the interaction cross section with our nuclear target.

The collimators defined a central transport momentum for electrons and positrons which ultimately will be the end point energy of the bremsstrahlung spectrum of our photon beam. The transported beam has roughly a Gaussian RMS spread of 15 % about this central value. For the bulk of the data reported here, our central transport momentum (*ie* endpoint energy) was adjusted to be $\approx$ 300 GeV/c. The photons which impinge on our experimental target are derived through bremsstrahlung of the secondary electrons and positrons on a radiator consisting of a 27% lead foil. The bremsstrahlung photon spectrum is roughly of the form $dN_\gamma/dE_\gamma \propto 1/E_\gamma$ up to the endpoint energy of roughly 300 GeV meaning that the bulk of the bremsstrahlung photons are very soft. We have designed triggers to only record events from the upper end of the bremsstrahlung spectrum where both our acceptance and the cross section for photoproduced charm particles is appreciable Our typical triggered energy was $\approx$ 180 GeV.

2.2 Beam Tagging

Beam tagging system is meant to measure the energy of the interacting photon, as it is needed for measurements of the photoproduction dynamics which bear on QCD phenomenology. The tagging process is achieved in three parts. At the first stage the energy of the incoming electron or positron ($E_{e^\pm}$) is measured before it interacts with the lead radiator. This is done by the silicon tagging system (See Figure 2.1.2). The system consists of five silicon strip planes, arranged to measure the direction on the

either side of the dipole magnets. The incident lepton momentum measurement is based on its magnetic deflection. The incident electron and positron beam momentum is measured to $\pm 2\%$.

The difference of the energy of $e^{\pm}$ after it passes through the lead radiator is the energy of the radiated photon. Therefore, at the next stage the energy of the $e^{\pm}$ is measure again after it passes through the lead radiator. This is achieved by passing $e^{\pm}$ through another set of dipole magnets to measure which sweep the $e^{\pm}$ into two calorimeters called RESH (recoil electron shower) and POSH (recoil positron shower). RESH and POSH each consist of 13 counters, with alternating layers lead and lucite. By determining which counter is struck, the deflection angle of electron is determined, and its energy is calculated ($E'_{e^{\pm}}$).

Given the thickness of our 27% radiator, the impinging electrons or positrons generally produce many soft photons in addition to the hard (triggering) photon which occasionally creates the charm particles studied in our experiment. These additional photons are generally referred to as *multi-brem* photons. The experiment incorporates a forward electromagnetic calorimeter called the BGM (for Beam Gamma Monitor) to record the energy of the 0° non-interacting multi-brem photons so that they can be subtracted from the energy of the initial tagged electron or positron along with the recoil electron or positron to get a more unbiased estimate of the triggered photon energy. This device was also used to estimate the initial flux of photons.

The energy of the interacting photon is therefore:

$$E_{\gamma} = E_{e^{\pm}} - E'_{e^{\pm}} - E_{BGM} \tag{2.2}$$

2.3 Target

The FOCUS experiment uses segmented target configuration. This will help increase number of decays out of target. Based on the experience from E687, cleaner charm signals are obtained when the secondary vertices form outside the target [8]. We believe this is because a major background to charm are events with multiple interactions which can "fake" detached vertices. For example a non-charm hadronic photon interaction can produce a secondary which can undergoing a subsequent inelastic interaction within the target. The final state will have separated vertices just like a charm event and will be hard to eliminate through a detachment cut but can be easily eliminated by requiring that one vertex is in the gap between target segments.

The FOCUS segmented target was constructed from slabs of Beryllium Oxide (BeO). BeO has a fairly large radiation length to interaction length ratio and a fairly high density for such a low Z material. The large radiation length for our 15 % interaction length target both minimizes multiple Coulomb scattering within the target and the number of e^+e^- pairs created on each beam pulse which both confuses charm events and creates problems for the MWPC system by creating a large current draw. The relative high density allows us to use thin target segments which maximizes the number of very clean charm decays which take place in the air gaps between target segments.

Each target dimensions are $6.75\,mm$ thick in the beam direction and $25.4 \times 25.4(mm)^2$ in area. The targets are separated by $10\,mm$. The bulk of the data was taken by this target configuration.

In FOCUS two SSD tracking system is implemented, which are described below.

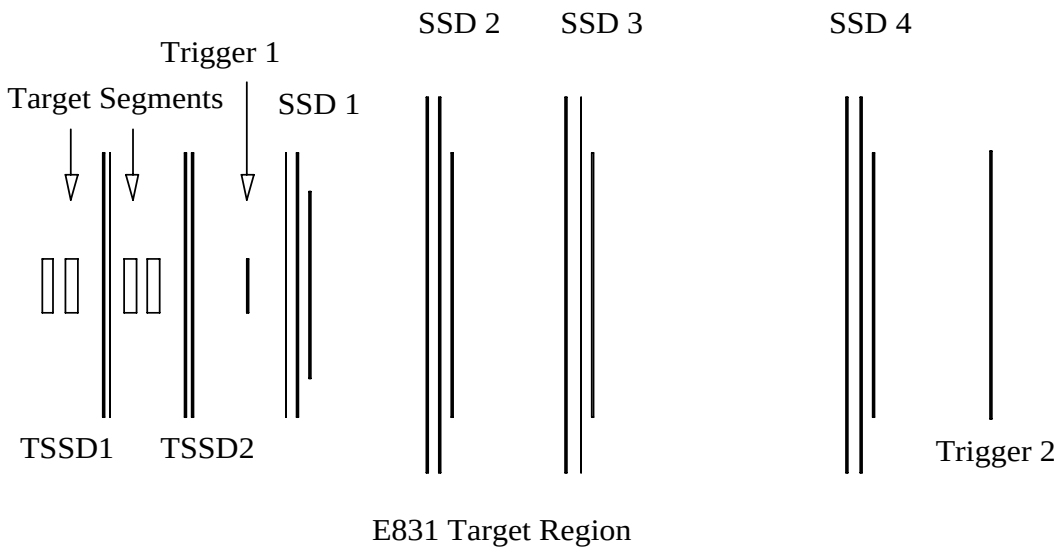

Figure 2.4: Target region and SSD configuration. Target silicon detectors (TSSD) help increase vertex resolution. Trigger 1 (TR1) and Trigger 2 (TR2) are scintillator counters used in the first level trigger.

2.4 Silicon Strip Detectors

The SSD detectors provide a spatial resolution of roughly $7 \rightarrow 14\mu m$ depending on which plane. They are composed of separate readout strips which collect charge that are freed when ionizing particles traverse through it. The thickness of the detector is usually on the order of $300\mu m$. For minimum ionizing particles, average loss in silicon is about $39\,KeV/100$

mum so that about 100 electron-ion pairs/μm are created [9]. Therefore, about 30000 ion pairs are created in the detector. This implies both high efficiency and a very good signal to noise ratio to suppress Johnson noise. Each silicon strip is pulse height analyzed.

2.4.1 Target Silicon Detector

Four planes of silicon microstrips are installed in two stations of two planes (X and Y) each to help improve the vertex resolution.[3] The components of the target silicon consist of 4 planes of 25μ pitch 300μ thick planes of silicon microstrip detector. Each silicon plane has 1024 channels, or about an inch of active area, which covers the majority of the photon beam size at the E831 target. As shown in Figure 1, these target silicon planes were interleaved between the experimental target segments. The target silicon information is present for roughly 2/3 of the FOCUS data.

2.4.2 Microstrip Detector

The microstrip detector is located about 5 cm downstream of the most down stream experimental target segment. By measuring the trajectories of charged particles with very high precision, one can exploit the lifetime of charm particles (typically 1 cm decay length for D meson) to identify charm signals. Referring to the diagram in figure 2.3, the microstrip system consists of 12 planes arranged into 4 stations of 3 planes each. In each station, one plane measures in the y-direction and two planes are titled in opposite direction from the y-axis by 45°. Each plane is divided into an inner high-resolution region and an outer lower-resolution region. The strips in the planes of the most upstream station have 25μ pitches in the inner region and 50μ pitches in the outer region. The remaining stations have 50μ and 100μ pitches, respectively. The SSD described in Table 2.1

[3]The target silicon provides a hit coordinate very close to the vertex position before a substantial lever arm for multiple Coulomb scattering gets a chance to develop.

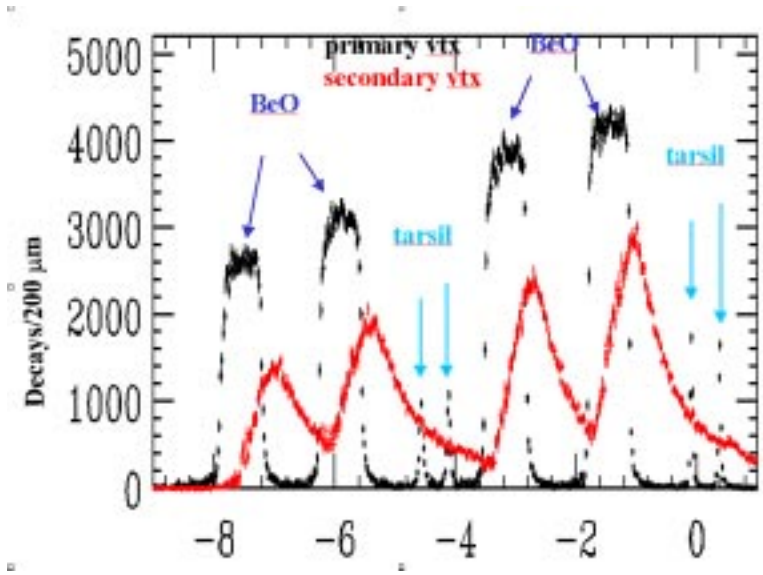

Figure 2.5: Z distribution for the primary and secondary vertices for the background subtracted Golden mode charm. The BeO segmented target and target silicon detector planes are evident

Table 2.1: SSD specifications. Each station consist of 3 planes in y, u and v views. The u and v views are titled in opposite direction from the y-axis by 45°.

Station	Total Active Area	High Res. Active Area	Strip Pitch
1	$2.5 \times 3.5cm^2$	$1.0 \times 3.5cm^2$	$25\,\mu m,\ 50, \mu m$
2	$5.0 \times 5.0cm^2$	$2.0 \times 5.0cm^2$	$50\,\mu m,\ 100, \mu m$
3	$5.0 \times 5.0cm^2$	$2.0 \times 5.0cm^2$	$50\,\mu m,\ 100, \mu m$
4	$5.0 \times 5.0cm^2$	$2.0 \times 5.0cm^2$	$50\,\mu m,\ 100, \mu m$

2.5 The Analysis Magnets

Momentum analysis of charged particles is performed by measuring the deflection in the fields of two dipole magnets M1 and M2. These magnets are used to deflect charge tracks in opposite directions. The transverse momentum kick is 0.4 GeV/c for M1 and 0.85 GeV/c for M2. The "kick" of a magnet is a measurement of the integral of the B-field such that the angular deflection of a charged particle traversing the magnet is given by the kick over momentum to leading order in 1/momentum. The ratio of the transverse kicks is such that the tracks come back to their original undeflected position toward the downstream end of the spectrometer. This ratio was chosen so that the 0° e^+e^- pairs converted in the experimental target would tend to traverse the central electromagnetic calorimeter hole rather than creating additional showers and radiation damage for the lead glass blocks located close to the central median plane.

2.6 Multiwire Proportional Chambers (MWPC's)

The multiwire proportional chamber system consists of 20 signal planes grouped into 5 stations with 4 planes per station. Each station has four views. The X view wires run vertically and measured horizontal position. The stereo angle for U and V views is 11.3^o from the Y view. The orientation of the wires is shown in Figure 2.6. The chambers P0, P1 and P2 are located between the two analysis magnets, and P3 and P4 are located downstream of the second analysis magnet. The chambers that are not located directly down stream of the analysis magnets, and therefore not limited in acceptance by magnet aperture, P1, P2 and P4 are larger to increase acceptance. The specifications of the chambers are summarized in Table 2.2.

Table 2.2: PWC specifications.

Properties	P0	P1	P2	P3	P4
Aperture (in^2)	30 x 50	60 x 90	60 x 90	30 x 50	60 x 90
Wire Spacing (mm)	2.0	3.0	3.0	2.0	3.3
No. X-view Wires	376	480	480	376	480
No. Y-view Wires	640	704	704	640	704
No. U/V-view Wires	640	768	768	640	768
Gas Used	Argon-Ethane(65/35) Bubbled through 0° C ethyl alcohol				
Voltage	2.80-3.20 kilovolts				

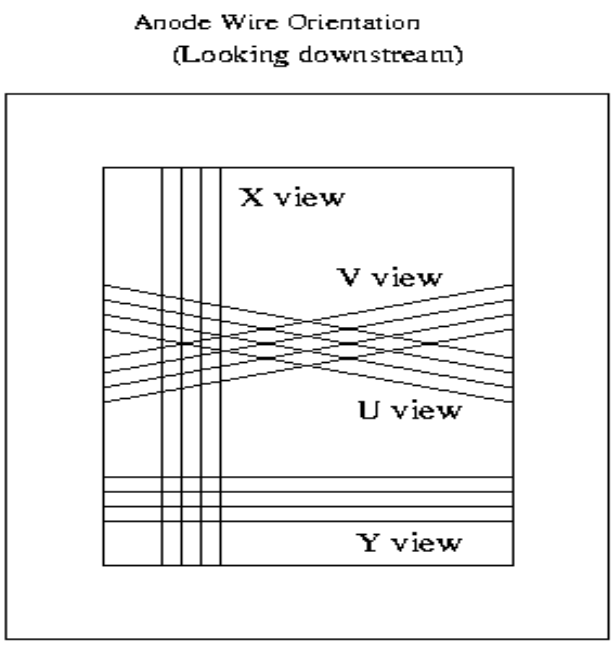

Figure 2.6: PWC orientation looking down stream. There views u and v are tilted 11.3^o with respect to the horizontal.

2.7 The Straw Tube System

Three straw tube wire chambers are used to measure tracks the high pair flux region - a vertical stripe down the center of the spectrometer – where it was thought the conventional MWPC's might be deadened. Each chamber has three views, and within each view there are three nested straw layers. All three chambers have a vertical (X measuring) view and two angle views - $\pm 11.33^o$ from vertical. In fact we did not need to deaden the central region of the MWPC's and hence the Straw Tube system was not required but does provide additional tracking information.

2.8 Čerenkov System

Čerenkov radiation in a medium occurs when a charged particle travels faster than speed of light in that medium. The speed of light in the medium is given by:

$$\beta = \frac{P}{E} \geq \frac{1}{N} \tag{2.3}$$

where N is the index of refraction of the medium. Therefore, for particle to emit Čerenkov light its speed be $v_{particle} > c/N$.

There are three multicell threshold Čerenkov detectors in the experiment, referred to as C1, C2 and C3. The detectors are operated at atmospheric pressure and in the threshold mode. The gases are chosen so that different indices of refraction (i.e. different light velocities) establishes different momentum in which pions, kaons, and protons will begin to radiate Čerenkov light, see Table 2.3.

For convenience we summarize a few useful formulae for Čerenkov counters using a gas with index of refraction $N \equiv 1 + \delta$ and the relevant approximate forms when $\delta \ll 1$. The minimum (threshold) momentum for a particle of mass m to emit

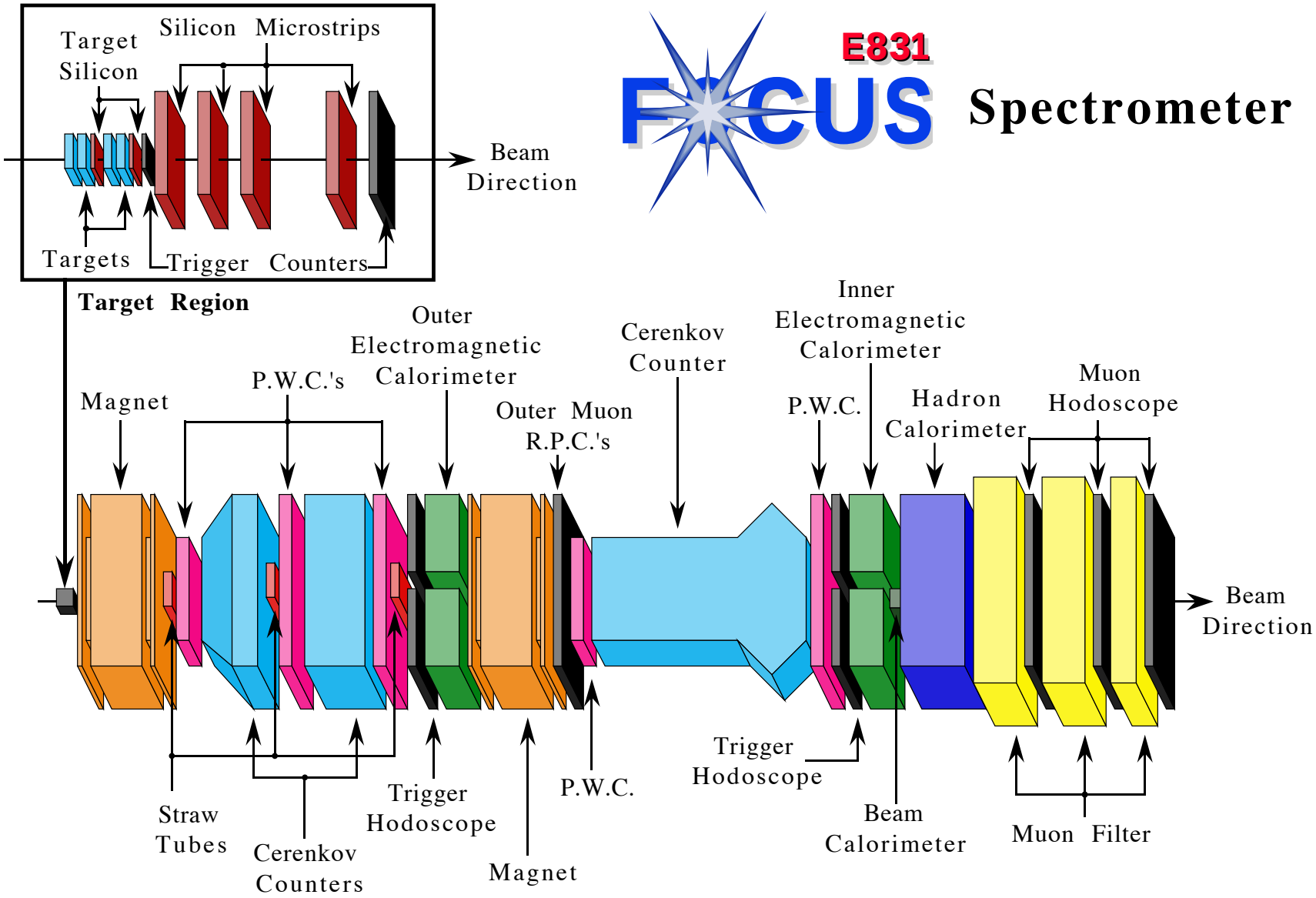

Figure 2.7: FOCUS spectrometer. In the upper left, the target region is shown.

Čerenkov light is:

$$P_{\text{Threshold}} = \frac{m}{\sqrt{1 - 1/N^2}} \approx \frac{m}{\sqrt{2\delta}}$$

and the angle of emitted Čerenkov radiation is :

$$\theta_C = \cos^{-1}\frac{1}{N\beta} \approx \frac{m}{P_{\text{Threshold}}}\sqrt{1 - \left(\frac{P_{\text{Threshold}}}{P}\right)^2}$$

Finally the number of Čerenkov photons produced per unit radiator length is proportional $\sin^2(\theta_c)$ which approaches $(m/P_{\text{Threshold}})^2$ as $P \gg P_{\text{Threshold}}$. This means that the high threshold counters need to be very long. Many of the relevant Čerenkov properties can be computed by specifying the *pion* threshold or $P_{\text{Threshold}}$ for particles of mass $m = m_\pi \approx 0.140 GeV/C^2$ and the number of photoelectrons recorded for a $\beta = 1$ track. For our system the three pion thresholds were chosen to be 4.5 , 8.4 and 17.4 GeV/c by use of appropriate gas mixtures and the photoelectron yield ranged from roughly 2.5 to 20 depending on the phototube and Čerenkov counter.

Our Čerenkov algorithm , described in depth in the next Chapter, exploited the threshold behavior , size of the Čerenkov cone and number of Čerenkov photons to identify charged particles. The approximate particle identification momentum ranges are summarized in Table 2.4.

2.8.1 C1

The Čerenkov detector C1 is the most upstream of the three Čerenkov counters, lying just beyond the first analysis magnet, between first two PWC's P0 and P1. The gas used was a helium-nitrogen mixture, and the total length of the gas volume along the beam direction is 71 inches. A schematic of the detector is shown in Figure 2.10, and side and top views are shown in Figures 2.9.

The active area of the counter spans 80 in. in the magnet bend direction and 50 in. in the transverse direction. It is divided into 90 cells by a series of mirrors

covering the downstream plane of the gas volume. The cell geometry as viewed from upstream of the detector is shown in Figure 2.8. This geometry was determined from photographic information and the results of calibration with a muon beam. The mirrors are organized into two readout system, planar and focusing. The focusing readouts use thin glass mirrors designed to focus Čerenkov light onto individual phototubes located upstream of the mirrors, just outside the fiducial volume. Each of the 40 focusing mirrors represents one cell, and all are located in the outer portions of the counter. The corresponding 40 phototubes have diameters of 3 or 5 in.; the smaller ones require additional collection cones to ensure complete light collection. All phototubes were protected from helium diffusion by flushing a fast stream of N_2 between quartz windows and the PMT face. Two glass planar mirrors, each 14 in. $\times$ 32 in., are oriented at 90° with respected to each other and 45° to the beam direction. Light reflecting off these is detected by 2 and 3 in. phototubes, 25 on each side of the counter, oriented exactly transverse to the beam direction. Light collection cones are located in front of the phototubes, and are close-packed to ensure that no light reflected from the planar mirrors escapes detection. These collection cones are constructed of specular quality *Colizak* aluminum. All reflective surfaces were coated with MgF_2 for optimum reflectivity at 350 nm.

The response of the counter can be described in terms of the average number of photoelectrons detected in a particular cell radiated by a $\beta = 1$ particle, when the Čerenkov cone is completely enclosed in the cell. The typical cell in the C1 planar section sees 3.6 photoelectrons while the focusing cells see about 2.5 photoelectrons. The C1 Čerenkov counter was built by the University of Illinois group. I was in charge of calibrating this counter, modifying its electronics[4], and maintaining its performance

[4]We moved its PMT amplifiers from "upstairs' in the counting house to a location placed locally on the counter to reduce noise from RF cable pick-up and reduce noise. We also install TDC's for

Table 2.3: Čerenkov counter specifications. The momentum threshold for the three charged particles are give for each counter.

counter	Gas	Threshold (GeV/c)			No. of Cells	Ave. Number of Photoelectrons
		pion	kaon	proton		
C2	N_2O	4.5	15.9	30.2	110	$8-11$
C1	$He-N_2$	8.4	29.7	56.5	90	$2.5-3.6$
C3	He	17.4	61.5	117	100	9

Table 2.4: Particle identification momentum ranges

Particle indent.	5-chamber track	3-chamber track
$e^{\pm}$	0 - 17.4 GeV/c	0 - 8.4 GeV/c
$\pi^{\pm}$	4.5 - 17.2 GeV/c	4.5 - 8.4 GeV/c
$e^{\pm}$ or $\pi^{\pm}$	17.2 - 61.5 GeV/c	8.4 - 29.7 GeV/c
$K^{\pm}$	17.4 - 56.5 GeV/c	17.4 - 29.7 GeV/c
P	17.4 - 56.5 60.8 - 115.5 GeV/c	17.4 - 56.5 GeV/c
$K^{\pm}$ or P	4.5 - 17.4 GeV/c	4.5 - 8.4 GeV/c

throughout the FOCUS run.

2.8.2 C2

The Čerenkov detector C2 has the lowest threshold of the three detectors with a pion threshold of 4.5 GeV/c. The gas was pure N_2O, and the total length of the counter gas volume along the beam direction is 74 in. and aperture of 64×94 in. The detector is located between P1 and P2.

The area divided into 110 cells with the geometry shown in Figure 2.8. All the

each cell in an attempt to remove out-of-time noise from pileup e^+e^- pairs

cells are organized in a planar mirror readout system similar to the central section of C1. Each of the two mirror sections measures 44×92 *in.* and is made up of 1 mm thick glass. The small vertical gap between the two mirrors sections in the center of the counter shown in the Figure was designed to reduce the material in the region of high incident photon and electron pair flux. The photoelectron yield for the 2-in. cells ranged from 8 to 16 with an average of 11 photoelectrons. For the 5-in. cells, the photoelectron yield varied from 5 to 13 with an average value of 8 photoelectrons.

2.8.3 C3

The Čerenkov counter C3 which has the cell structure shown in figure 2.8, was the most downstream of the three counters and was located downstream of the second analyzing magnet between P3 and P4. The counter was a helium threshold counter which was 277 in. long with an aperture at the upstream end of 60×93.25 *in.*. It had a pion threshold of 17.4 GeV/c – the highest in the system.

The active area of the detector spans 200 cm. in the magnet bend direction and 140 cm. in the transverse direction. The area is divided into 100 cells; all cells are defined by the boundaries of focusing mirrors located at the downstream end of the gas volume.

The photomultiplier tubes were separated from the helium volume by CaF_2 windows which were used for all the central cells and quartz windows which were used for the outer cells. The gap between the tube faces and the gas volume windows were flushed with N_2 in order to prevent helium from poisoning the tubes.

The photoelectron yield for all the cells ranged from 3 to 17 with an average of 9.

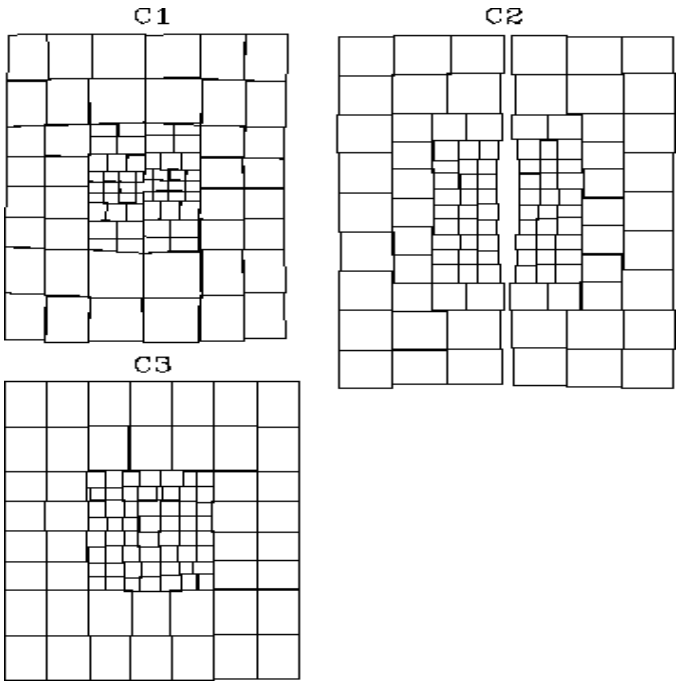

Figure 2.8: C1, C2 and C3 cell structure

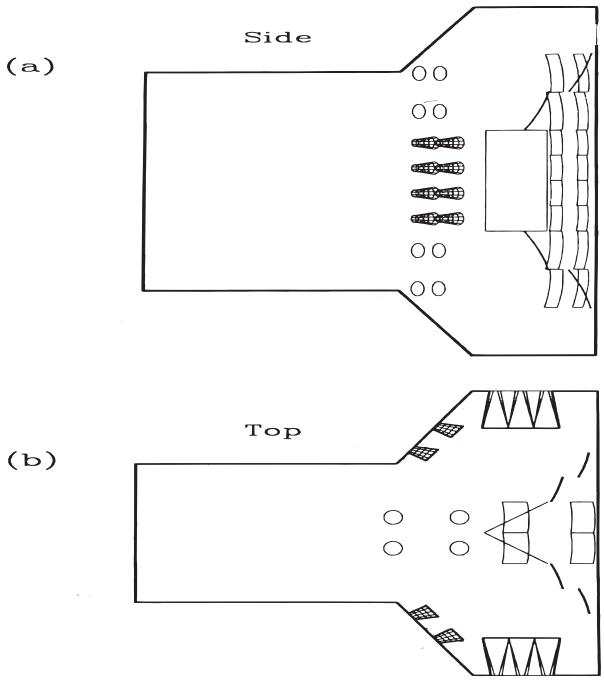

Figure 2.9: C1 side and top views

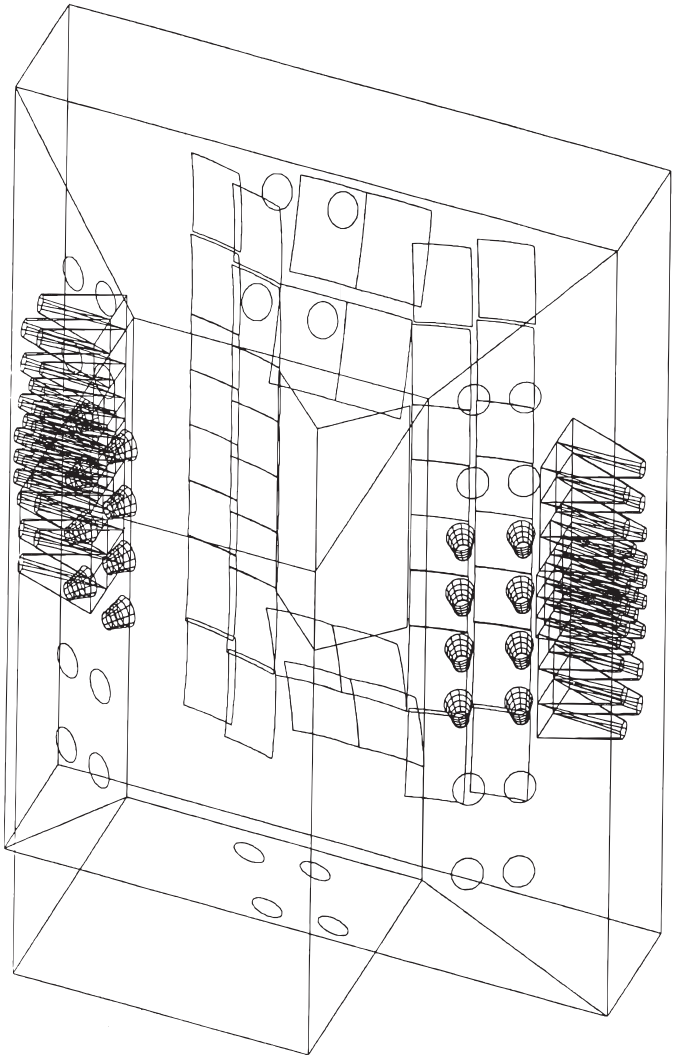

Figure 2.10: C1 schematic

2.9 Calorimetry

The electromagnetic calorimeters OE and IE were not used in this analysis. The hadronic calorimeter HC only affected this analysis through its role in the zero level trigger. The HC detects the sum of the energy of all hadrons which strike it. The hadronic energy trigger was used further suppress non-hadronic, photoproduced events such as e^+e^- pairs as well as helping to insure that we triggered on the upper end of the bremsstrahlung spectrum.

2.9.1 Outer Electromagnetic Calorimeter (OE)

The OE measures the wide angle electromagnetic particles (photons and $e^{\pm}$) that pass outside the acceptance of the second analysis magnet. It is located just downstream of the M2 magnet. The OE is a sampling calorimeter with alternating layers of lead and plastic scintillator, and it consists of x, y and z planes. In addition, there is 100 scintillator tiles plane with a fiber optics readout which is used for pattern recognition.

2.9.2 Inner Electromagnetic Calorimeter (IE)

The IE measures the electromagnetic particles that pass through the second analysis magnet.It is composed of lead glass blocks arranged in a tower geometry. There are two sides to the detector with a central gap to allow the passage of the intense beam of non-interacting photons and converted e^+e^- pairs. Again, the IE only affected this analysis due to its role in the trigger.

2.9.3 Hadron Calorimeter (HC)

The hadronic calorimeter is constructed with 18 alternate layers of $4.4\,cm$ thick Iron plates and $0.7\,mm$ think scintillating tile planes using fiber readout in tower geometry,

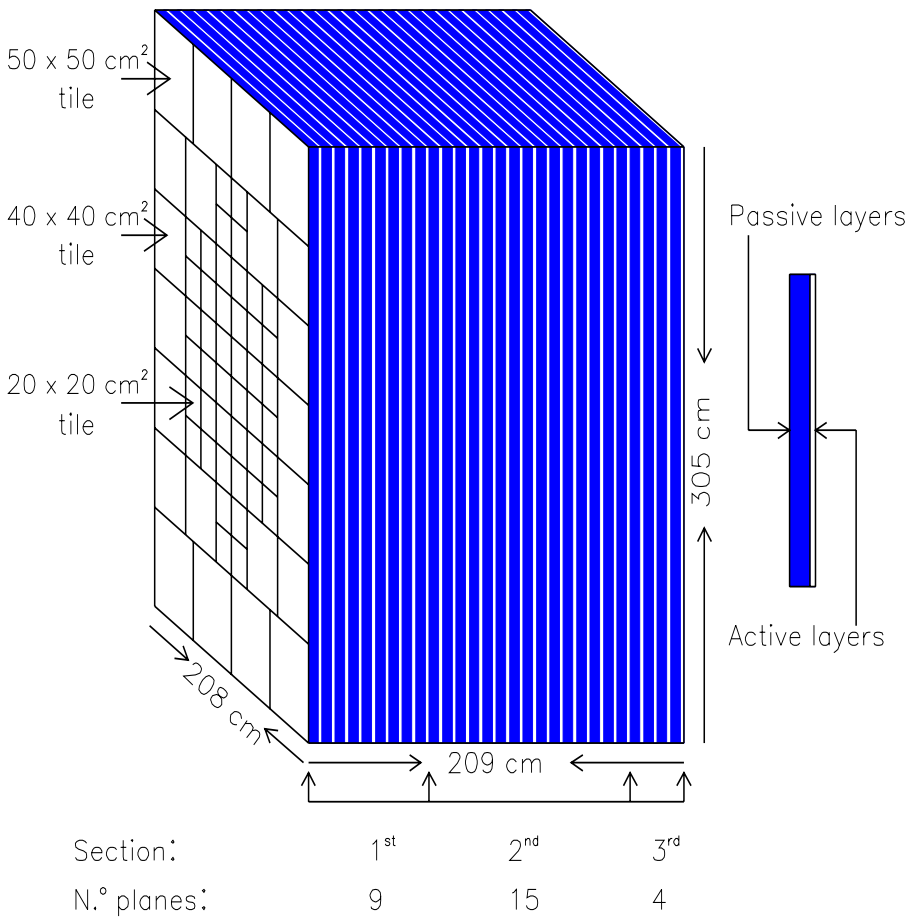

Figure 2.11: HC schematics.

with smaller tiles in the center and larger ones at the outside region. The layers are arranged into three sections, with first section having nine layers, second section having 15 layers, and third section having 4 layers. This scheme enables for deposited energy measurement as a function of depth, see Figure 2.11. The scintillators have fast response, enabling the HC to be included in the first level trigger to trigger on events with hadronic final states rather than $e^{\pm}$.

2.9.4 Beam Gamma Monitor Calorimeter (BGM)

This calorimeter measures the electromagnetic energy that passes through the hole in the IE. This was used to help tag the photon beam energy and determine our incident photon flux.

2.10 Muon Detector

Muons do not suffer significant energy loss due to ionization (or dE/dx) because of their larger mass and hadronic absorption as they don't interact strongly. Therefore, muon detectors are placed down stream of large iron blocks which act as filters to filter out electrons and hadrons, and let the muons through. There are two sets of muon detectors. The Outer Muon detector which use Resistive Plate Chamber system to detect high angle muons. The Inner Muon detector which consist of three stations made of scintillating counter arrays called MH1, MH2, and MH3. The MH1 and MH2 stations consist of x and y views and MH3 consist of u and v views. Figure shows one view from each station. MH1 and MH2 were build, designed, and commissioned by the University of Illinois group. I built and tested many of these counters.

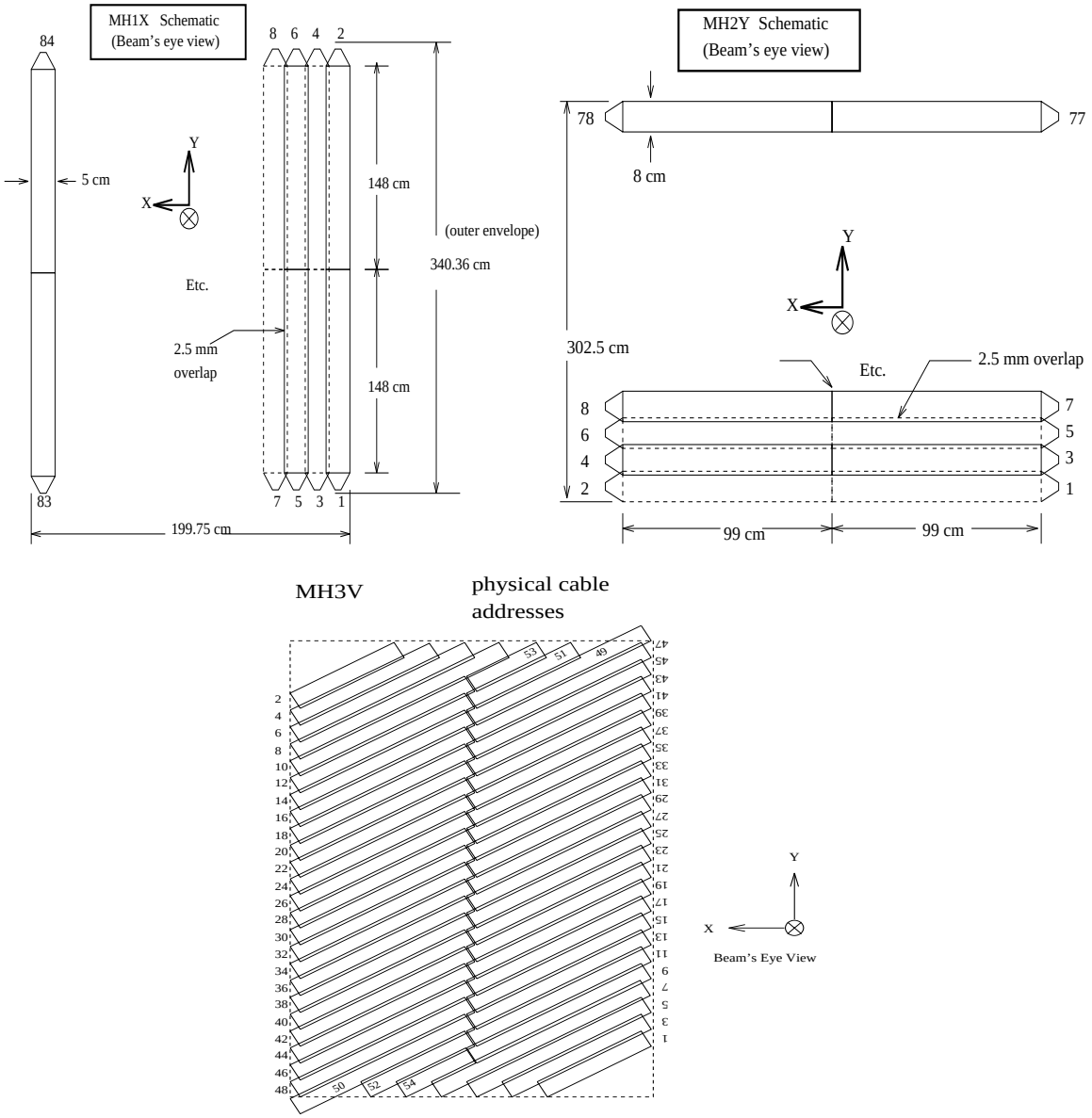

Figure 2.12: Inner Muon array schematics. The schematics for MH1Y, MH2X and MH3U are similar to MH1X, MH2Y and MH3V respectively

2.11 Trigger

The electronic logic that is required to select the interesting events from the background is called the trigger. FOCUS typically had about 10^8 interactions per spill (mostly electromagnetic) and triggered on about 30000 interactions per spill (mostly hadronic). It is known that in high energy photoproduction interactions the hadronic interaction rate is about 1/500 of the rate for pair production. The $e^{\pm}$ pairs generally are produced at a very small transverse momentum, and very low angle trajectories, whereas the hadronic interactions produce particles with larger transverse momentum, and wider trajectories. The hadrons also deposit larger energies in the hadronic calorimeter. Therefore the main purpose of the trigger is to trigger on the events with wide angles and non-negligible deposited energy in the HC.

The first level of main hadronic trigger is called the "Master Gate" (MG). The MG trigger occurs within $200\,ns$ from the time that interaction takes place. It takes about $160\,ns$ to transfer the information from the spectrometer, and the remaining $40\,ns$ is used to make a decision.

If the MG accepts the event, then the readout process and evaluation of the second level trigger begins. The second level trigger decision takes $1.2\,\mu s$. If the event is accepted by the second level trigger, writing the state of the detector to the magnetic tape for off line analysis continues, otherwise the readout electronics are reset and the process is repeated. The electronic are reset in $1\,\mu s$.

2.11.1 First Level Trigger

The first level trigger checks to ensure that the photon has interacted in the target and there charged particles pass through the target. This is achieved by $TR1$ which located at the upstream of the first SSD plane, see Figure 2.3. The $TR1$ counter

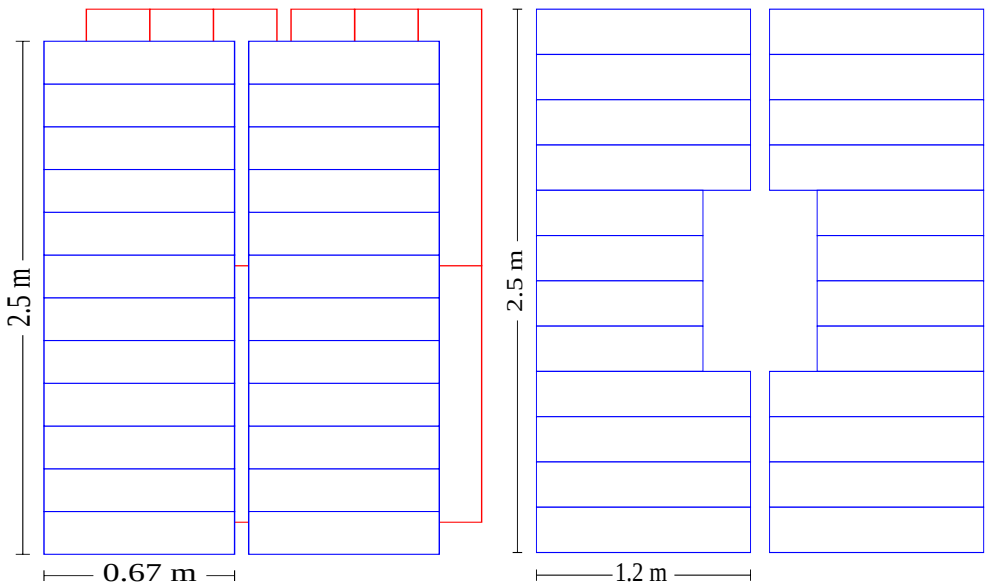

Figure 2.13: $H \times V$ and OH schematic

consists of a scintillator counter and a PMT. The TR2 counters are located down stream of the last SSD plane, and ensures that the charged particles that pass through $TR1$ also go through the microstrips. $TR2$ consists of four scintillator counters and PMT's.

A requirement is made that there are wide angle tracks in the event by using the $H \times V$ array. This set of arrays are located down stream of $M2$, after the last PWC station. A fast trigger logic module determines if the pattern of his is consistent with one charged particle, $(H \times V)_1$, or more than one, $(H \times V)_2$. The array has a central gap to let the $e^{\pm}$ pairs through without counting them.

Another set of scintillator counters called OH are located upstream of OE to assure passage of at least one particle. There is also a gap at the center of to let the $e^{\pm}$ pairs through.

The hadronic MG requirement is then:

$$MG1 = TR1 \cdot TR2 \cdot \{(H \times V)_2 + [(H \times V)_1 \cdot OH_1]\} \cdot E_{HI} \tag{2.4}$$

where E_{HI} ensures the energy deposited in HC by the hadrons is above a high threshold.

2.11.2 Second Level Trigger

The second level trigger requires that there an evidence of a minimum number of tracks outside the pair region. This is done by evaluating a logic signal with a voltage proportional to the number of hits in each plane that is derived from the PWC readout module. The information from each plane are combined, and an evidence of at least three tracks outside the pair region is required ($MULT4$).

The inner electromagnetic calorimeter (IE) is also used at the second level trigger. The electromagnetic energy deposited in IE is required to be over a threshold, and at least two hits above threshold in IE is required (E_{IE-2}).

The hadronic second level trigger requirement is then:

$$TRIG1 = MG1 \cdot E_{IE-2} \cdot MULT4 \tag{2.5}$$

Chapter 3

Data Reconstruction, Analysis Algorithm And Skim

In this section we summarize some critical aspects of our track reconstruction, vertexing, particle identification algorithms and the data reduction techniques used to skim our data down to a manageable size.

To a large extent, tracks were found independently in the microvertex detectors and the MWPC system. The two independently track segments passed a "link" cut if they were consistent with being due to a single particle consistent trajectory between the two systems. Although this strategy was primarily historical (*eg* a US group wrote the MWPC reconstruction code and built the chambers and an Italian group built the SSD system and wrote the SSD tracking code.), it turned out to be a wise decision since we discovered relative motions between the systems on the order of a millimeter due to ground motions. By comparing the the MWPC and SSD trajectories, we could correct for this motion and thus maintain a high linking efficiency over time.

In general, charm secondaries apart from long lived Vee's and kinks were required to be linked tracks. However wide angle tracks, reconstructed by the SSD system but

missing links to the PWC were allowed for tracks in the primary vertex. We believe the inclusion of unlinked primary vertex traces significantly increased the efficiency of our vertex algorithm without substantial degradation in vertex resolution.

We begin with a discussion of MWPC tracking.

3.1 MWPC Tracking

There are three major categories of tracks in FOCUS. The tracks which hit P0, pass through the downstream magnet M2,aperture and generally leave some hits in P3 and P4 are called "5-chamber" tracks.

Tracks with hits only in P0, P1, and P2 are called "stubs" or "3-chamber" tracks. These tracks generally are not able to traverse the M2 aperture either because they are wide angle, or have low momentum and are deflected too much by M1 to traverse the M2 aperture.

The third category are the "recon" tracks which are from decays downstream of of the first wire chamber which do not have hits in P0. This category includes secondaries from the long lived neutral vees decaying into two charged tracks between P0 and P2, and "kinks" that are track segments which join with other track segments but with a finite angle between the segments.

It was important to be cognizant of whether a particle was a track or a stub since tracks had significantly better fractional momentum resolution than stubs. Many of the reconstruction algorithms make use of the anticipated tracking momentum error in constructing vertices and computing quantities such as the normalized mass.[1]

[1] A normalized mass for say a $D^+ \rightarrow K^-\pi^+\iota^+$ candidate would be the difference between the reconstructed mass and the nominal mass divided by the anticipated mass error.

3.1.1 Microstrip Track Reconstruction

The algorithm for SSD track reconstruction is based on projection finding on the three separate views. Of the four planes in each view, a minimum of three planes is required to from a projection. Projections are formed into tracks if the group of projections pass the hypothesis that they are consistent with a line. If the χ^2 per degree of freedom for the hypothesis is less than 8, the projections are considered to form a track. The parameters of the fit are slope and intercept of the track in the granite block coordinate system.

The class of hits that are not used to associated with any reconstructed track are used to search for wide angle tracks and for highly multiple Coulomb scattered tracks.

The reconstruction efficiency of of the SSD tracks is proportional to momentum, with higher momentum tracks having better efficiency. The resolution of the SSD tracks is also a function of momentum, for lower momentums tracks have a larger multiple Coulomb scattering, hence a worse resolution.The resolution on the intercept of a track extrapolated to the center of our target can be expressed as:

$$\sigma_x = 11\ \mu \sqrt{1 + \left(\frac{17.5\ GeV}{P}\right)^2}\ ,\quad \sigma_y = 7.7\ \mu \sqrt{1 + \left(\frac{25.5\ GeV}{P}\right)^2} \tag{3.1}$$

where P is the track momentum. The constants $11\mu m$ and $7.7\mu m$ are the granularity of SSD strips. This equation applies to tracks which traverse the high resolution portion of each of the SSD microstrips. It includes the multiple scattering contributions in the SSD and TR1. In general we will do better than this because of the target silicon.

3.1.2 PWC Track Reconstruction

The algorithm proceeds by reconstructing projections in all views in each station. The projections in the X (non-bend) view are formed by matching the hits on the PWC hits

with the seed track extensions in the SSD. The Y, U and V (bend) view projections are formed independently from the PWC hits alone. Then, the X projection is matched to the U, V, and Y projections to form a track. After all the tracks from the SSD-extended projections are used, new projections in the X view are formed using the hits that were not used in the previous steps, these projections are in turn matched to the un-used U, V, and Y projections to form more tracks.

The reconstruction algorithm requires that the reconstructed tracks have hits in the first PWC station, P0, it also requires that the tracks can miss a maximum of four hits in all PWC stations, and that they can miss a maximum of two hits per PWC station.

At this stage a χ^2 fit is performed on all candidate tracks, where the fit parameters are the slope and intersection of each track in X and Y views in the $M2$ magnet bend plane. An additional fit parameter for the 5-chamber tracks is the change in slope in the Y view between the track segments upstream and downstream of M2 magnet. Finally A χ^2/DOF cut is applied to select the tracks.

There are tracks that leave the PWC geometrical acceptance before P2. To try to recover these tracks, the algorithm uses the SSD tack extensions to search for the unused hits in the X view of P0 and P1, which then are combined with the U, V, Y projections to form tracks. The tracks which extend only to P0 are required to have hits in all four views, and the tracks which extend to P1 are required to have at least three hits in each station.

There are higher order corrections to the linear least squares fits described above. Because of the finite length of M2 one correction is to account for the sudden bend approximation implied by the above parameterization. There also other magnetic corrections such as counting for the fringe field, and the fact that the components of the $\vec{B}$ field are not constants but are functions of x, y and z.

3.1.3 Linking of SSD and PWC tracks

Linking is performed by extending the SSD track to the M1 center and matching them with the PWC tracks. In addition, for the 5-chamber PWC tracks, bend angles inside the M1 and M2 magnetic field should be consistent. We significantly reduce backgrounds by requiring that the PWC and SSD track segments "link". Those PWC tracks which don't link can be used as possible decay products of Vee's and Kinks.

3.1.4 Vertex Reconstruction

The data reported here were both selected and reconstructing using the DVERT vertex finder developed at the University of Illinois. DVERT is a "candidate driven" rather than "topological" vertex finder which generally means it is much more efficient at short detachment distances. We illustrate the vertexing and selection philosophy with the state $D^+ \rightarrow K^-K^+\pi^+$ which is one of the states analyzed in this thesis.

Rather than searching for a primary and secondary decay vertex using pattern recognition techniques we begin by looping over all potential 4 track combinations as a possible $D^+ \rightarrow K^-K^+\pi^+$ candidate. The first cut is to require DCL or "Dee" confidence level of the $K^-K^+\pi^+$ vertex to be larger than 1%. This is found by selecting an x_o , y_o ,and z_o which minimizes the χ^2 given in Eq. (3.2). The extrapolation errors σ_{xy} are approximately those of Eq. 3.1.[2] For the $K^-K^+\pi^+$ this χ^2 would be converted to a DCL using 3 degrees of freedom.

The next skim cut we would apply would be to require the $K^-K^+\pi^+$ invariant mass to lie in the range 1.7 GeV/c^2 $< M(K^-K^+\pi^-) < 2.1$ GeV/c^2 which is a range large enough to allow plenty of background on either side but narrow enough to

[2]However, we include information from the target silicon, and weight points appropriately for being in the high versus low resolution region of the SSD system.

significantly reduce our data and increase our skim fraction. In applying this cuts, we first cut down on combinatorics by requiring the kaons to satisfy a loose "kaonicity" cut of $\Delta W_K > 0.5$ (See section 3.2).

The last cut (which is the most CPU intensive to compute) is the presence of a high quality primary vertex which is sufficiently detached from the "Dee" vertex. We do this by creating a "seed" track for the "Dee" which passes through the secondary vertex and is directed against the D^+ momentum vector. Generally the seed track has much better measurement error than any of its constituent tracks because its intercept is averaged. We then for all intersections of the seed track with any of the tracks left over in the event. The DVERT algorithm, tries to form the largest multiplicity primary vertex with a PCL (Primary vertex Confidence Level) in excess of 2 %). If a primary vertex is found, we construct the detachment or the 3 dimensional separation between the primary and secondary vertex divided by the anticipated, event-by-event RMS resolution , σ. Then, l/σ becomes an good measure of the detachment of secondary vertex from the primary vertex. This cut improves the signal to noise ratio by requiring larger l/σ usually at the cost of some signal. The event satisfies the skim as long as the ℓ/σ exceeds a minimum cut of 2.5.

Isolation cuts are often used to greatly suppress non-charm and charm reflection backgrounds. The first type of cut which we will call the primary isolation cut or CL1 is basically a cut that no charm secondary track is consistent with pointing to the primary vertex. For the case of $D^+ \rightarrow K^-K^+\pi^+$, we would form the highest confidence level vertex with constructed from the primary vertex tracks and each of the $K^-K^+\pi^+$ tracks put the vertex in one track at a time. A cut would be placed on the maximum confidence level returned for the 3 trial vertices.

The second type of isolation cut requires that the confidence level that the remaining tracks (i.e. primary and secondary tracks excluded) form a vertex with the

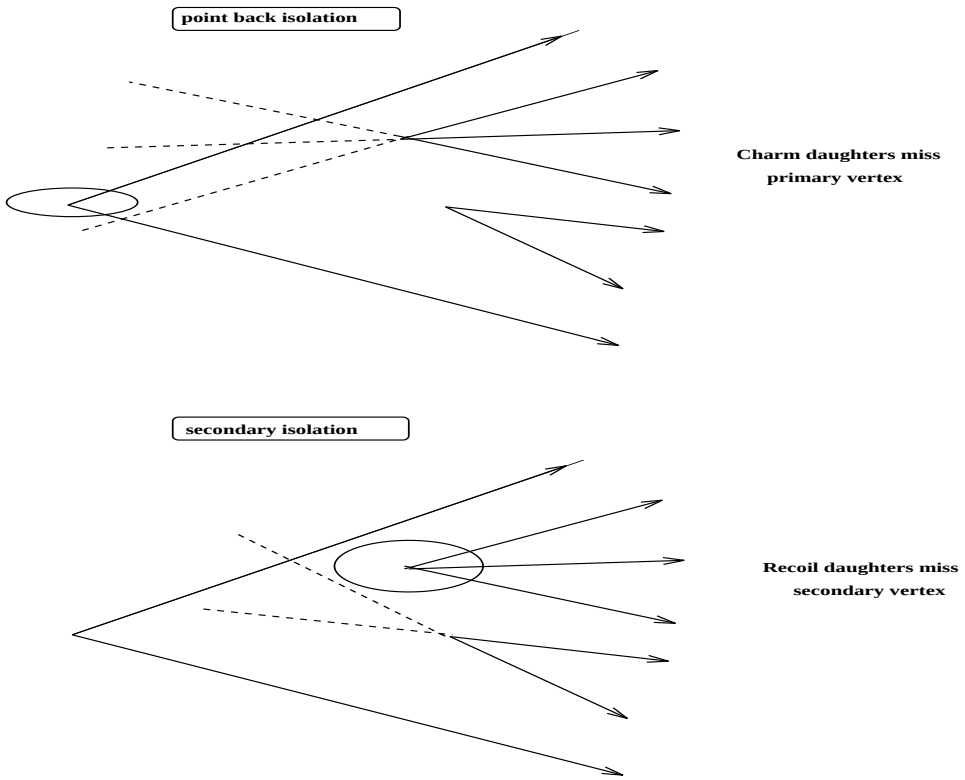

Figure 3.1: Schematic representation of isolation cuts Cl1 and CL2

secondary vertex tracks is less than certain cut (This cut is called exclusive secondary isolation cut, or CL2). This cut is very effective in suppressing backgrounds from higher multiplicity charm final states.

3.1.5 Momentum Determination

The momentum associated with a track is calculated by the bend angle of the track in M1 and M2 magnets. Depending on the type of the track different methods are used to calculate the momentum. For example, for the 5-chamber tracks the bend angle in M2 is calculated using the track parameters upstream and downstream of M2. For the 3-chamber tracks, the SSD and PWC portions of the track is used for calculating the bend angle in M1. The algorithm takes into account the magnetic field corrections. The following expressions give our approximate momentum resolution in M1:

$$\frac{\sigma}{P} = 3.4\% \left(\frac{P}{100\,GeV}\right) \sqrt{1 + \left(\frac{17\,GeV}{P}\right)^2} \tag{3.2}$$

and in M2

$$\frac{\sigma}{P} = 1.4\% \left(\frac{P}{100\,GeV}\right) \sqrt{1 + \left(\frac{23\,GeV}{P}\right)^2} \tag{3.3}$$

where the second terms inside the square root account for the multiple Coulomb scattering.[3]

[3]These are correct expressions in the absence of adjacencies. One gets an adjacency when several adjacent MWPC wires fire for a given track due to the presence of δ-rays, or sharing of the ionization cloud.

3.2 Čerenkov Identification Algorithm

In this section we will describe the algorithm used to identify charged tracks in FOCUS. We begin by describing the new algorithm and contrast this approach with that used in our preceding experiment – E687. We next illustrate the algorithm's performance using physics signals. Finally we briefly describe some of the methods used to monitor the quantum efficiency and noise of the Čerenkov cells.

3.2.1 The CITADL Algorithm

FOCUS uses a considerably modified Čerenkov algorithm than that used in E687. This new algorithm will be referred to throughout this article by the acronym CITADL (for Čerenkov Identification of Tracks by an Algorithm using Digital Likelihood). Before describing the new algorithm, we briefly describe the previous algorithm known as LOGIC. For a more complete description of this algorithm see [17].

Unlike CITADL, whose decision is based on the individual firing pattern of all 300 cells comprising the FOCUS/E687 Čerenkov system, LOGIC based its identification on the overall firing status of C1, C2, and C3. LOGIC rendered a single identification indicating whether or not the track was consistent with the electron, pion, kaon, and proton hypothesis. [4] This decision was based on the track momentum and the Čerenkov light observed in the three threshold Čerenkov counters. A counter was declared "on" if any of the cells within the track's Čerenkov cone fired. A counter was declared "off" if no cells within the cone fired and a total, minimum number of expected photoelectrons (typically 2.5) was expected under the pion hypothesis.[5]

[4]Muons can only be effectively separated from pions over a narrow momentum range just below each counter's pion threshold. Both E687 and FOCUS had a separate muon detection system to provide high quality muon identification.

[5]In order to save time, LOGIC computed the expected number of photoelectrons on each cell

Otherwise the firing status for that counter was declared unknown and its information was removed from the final decision. The observed "on" or "off" firing status was then compared to whether or not the counter should have fired under a given hypothesis. This prediction was based solely on whether or not the track momentum exceeded an "effective" momentum threshold for that hypothesis. [6]

Although the LOGIC algorithm was very effective at helping to isolate charm particles in E687, it did have shortcomings. LOGIC was biased to discriminate strongly against pions when one required positive kaon and protons identification. Much of LOGIC's bias towards light particle identification was intended given the goal of strongly suppressing pion backgrounds to the kaons used in constructing Cabibbo favored charm final states. For example, any cell firing within the Čerenkov cone sufficed to declare a counter on. But if no cells fired, a significant amount of predicted light was required before that counter would be declared off.

A major , unintended, bias was due to accidental firings of the Čerenkov cells due to "noise". The noise was either due to RF noise on cables, tube noise, and light from untracked, charged particles such as electromagnetic spray and photon conversions produced in the very intense photon beam. The electromagnetic noise source could be very serious for Čerenkov cells located in the center of the system approaching at times 25-50 %. Both biases tended to assign Čerenkov light to tracks making them inconsistent with "heavy" particles such as kaons and protons.

LOGIC's bias towards light particle identification both reduced the efficiency for

---

under the pion hypothesis unless the track was under the pion threshold for the Čerenkov counter. If a track were below pion threshold, the light yield was computed under the electron hypothesis. This allowed the Čerenkov system to help in the identification of electrons.

[6]The "effective" threshold was slightly higher ($\approx$ 10%) than the actual threshold in order to crudely take into account the gradual rise in the expected light yield with momentum above threshold.

kaon identification in Cabibbo favored decays and significantly increased backgrounds for rarer Cabibbo suppressed decays such as $D^o \rightarrow \pi^+\pi^-$ or $D^o \rightarrow \pi^-\mu^+\nu$. In order to suppress the copious backgrounds from $D^o \rightarrow K^-\pi^-$ or $D^o \rightarrow K^-\mu^+\nu$, one would typically require that the pion had a Čerenkov response which was inconsistent with that for a kaon.

While studying Cabibbo suppressed states ,we used D^o's skimmed from a sample of $D^{*+} \rightarrow D^0\pi^+$ with no Čerenkov cuts to measure the fraction of kaons which passed the pion cuts. Typically 5% of kaons were misidentified as pions in E687 by the LOGIC Čerenkov algorithm. Because of the basic inflexibility of the LOGIC algorithm, one would need to redesign the internal cuts to minimize the misidentification of kaons as pions and re-run the algorithm from tapes that had the required Čerenkov ADC information. Although, in principle, LOGIC could be re-run with other internal cuts, it was not a practical option since data summary tapes typically did not contain the Čerenkov ADC information.

CITADL was primarily motivated by the desire to produce a more flexible Čerenkov identification algorithm than LOGIC. In fact, overall performance in CITADL was significantly better in LOGIC primarily due to its ability to include the possibility of accidental firing of Čerenkov cells due to tube noise or untracked, electromagnetic debris. Rather than making a hard decision, on whether or not a track was consistent with a given hypothesis, CITADL returned relative likelihoods that the track had a Čerenkov pattern similar to that expected for the electron, pion, kaon, or proton hypothesis. One could then, for example, put a minimum cut on the likelihood ratio that the kaon hypothesis is favored over pion hypothesis in order get sufficiently clean kaons to do the required physics. Unlike LOGIC, very few cuts, or arbitrary parameters, were required to be "hardwired" in the CITADL algorithm.

Like LOGIC, CITADL only uses the on-off status of Čerenkov cells rather than

their pulse height in identifying particles. This decision made the computation of likelihoods simple since a cell's firing probability is given by the Poisson probability $(1 - \exp(-\mu))$ where μ is the expected number of photoelectrons under the given particle hypothesis.[7]

CITADL constructed a log likelihood variable based on the firing probability for all Čerenkov cells that a given track could potentially affect – all cells within the track's $\beta = 1$ Čerenkov cone. If the cell fired, and μ photoelectrons were expected, the log likelihood was incremented by $\log(1 - \exp(-\mu))$; if the cell failed to fire the log likelihood was incremented by $\log(\exp(-\mu))$. Cells which overlapped more than one track's Čerenkov cone were considered "confused" and excluded from the sum. The likelihood returned by CITADL is similar in spirit to the traditional continuous likelihood used in fitting. The only difference is that each event has only two outcomes – on or off. For this reason, we call it a "digital" likelihood.

CITADL returns its identification in the form of χ^2 like variables which we will call W_e , W_π, W_K, and W_P. They are defined by $W_i = -2\sum_i \log P_i$ where P_i is the probability for the observed outcome (on or off) for that cell under each of the 4 particle hypotheses. One would typically require that potential charm decay kaons pass a minimum cut on a likelihood difference variable such as $\Delta W_K \equiv W_\pi - W_K$. A large ΔW_K implies that the kaon hypothesis is significantly favored over the pion hypothesis. Unlike the case in LOGIC, there is no need to introduce "effective" thresholds , since the μ dependence on momentum is explicitly taken into account. There is also no need to declare a minimum number of photoelectrons required for a

[7]This assumes that the gains and thresholds are set such that a single photoelectron will produce an ADC count in excess of the threshold required to call a cell on. Under this assumption a cell will fire unless 0 photoelectrons are observed when μ are expected. The Poisson probability of getting zero photoelectrons is $\exp(-\mu)$.

Čerenkov decision. If a very small number of photoelectrons discriminated the two hypotheses, CITADL returns likelihood differences close to zero.

One cannot literally follow the prescription for incrementing the log likelihood described above since often cells will fire which are below the Čerenkov threshold under for the particle being considered. For example, consider the case where one is incrementing W_K for a firing Čerenkov cell in a counter with a kaon threshold larger than the track momentum. The probability that a Čerenkov light from a kaon could fire this cell is zero and by the above prescription one would need to increment the log likelihood by $\log(0)$. The algorithm concludes that if the only way a cell can fire is from the Čerenkov light from the given track, one detected photon is enough to exclude a sub-threshold hypothesis with an infinite likelihood. We initially solved the problem of divergent likelihoods on the computer by assigning a small nominal sub-threshold firing probability of 10^{-10}. The resultant likelihoods differences between the kaon and pion hypotheses would consist of a series of spikes at multiples of $-2\log(10^{-10}) = 46$ since W_π would be incremented by this amount for every cell expected to fire under the pion hypothesis but not the kaon hypothesis.

We later determined the accidental firing rate by measuring the fraction of times a Čerenkov cell would fire, even if it were outside of the $\beta = 1$ Čerenkov cone of all observed tracks. A typical plot of the accidental rate as a function of cell number for one of the runs is shown in Figure 3.2. The accidental rate varied considerably and for central cells was very large. It is very easy to incorporate accidental firing rates in the firing probability. The prescription is $P_{fire} = a + (1 - \exp(-\mu)) - a\ (1 - \exp(-\mu))$ where a and μ are the accidental rate and the number of photoelectrons expected

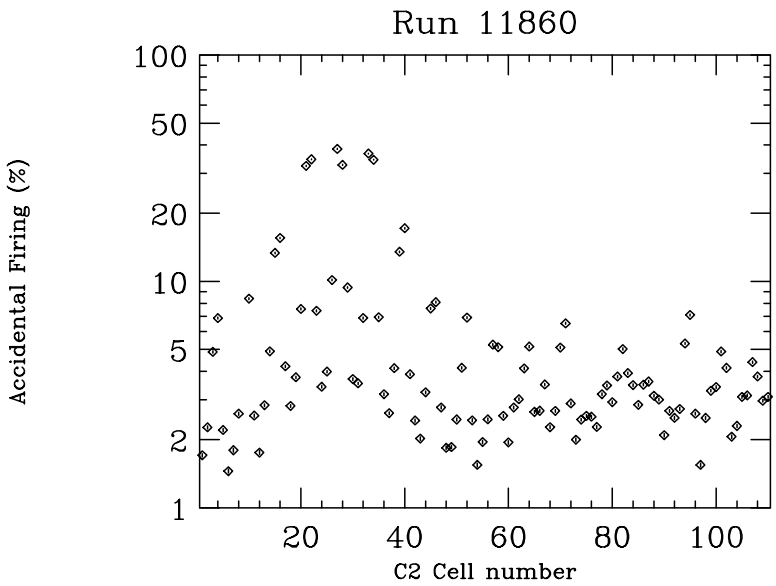

Figure 3.2: The fraction of times (in percent) that a cell in C2 fires when no detected track's $\beta = 1$ Čerenkov impinges on the cell. These data were accumulated over a single run. Although most of the cells have an accidental rate of a few percent, cells located near the beam axis have accidental rates as high as 40%.

for the given cell.[8] [9] The inclusion of accidental rates, significantly improved the performance of our new algorithm relative to LOGIC.

3.2.2 CITADL Performance

The very high statistics FOCUS data set provided numerous checks of the performance of the Čerenkov system and the CITADL algorithm – often on a run-by-run basis. These checks relied on using the decays of final state into known daughters. The decays $K_s \rightarrow \pi^+\pi^-$ provided a very pure and highly copious source of pions, consisting of 15,000 decays in each of our nearly 6000 runs. This sample was large

[8] This form assumes that the accidental firing and Čerenkov firing are statistically independent and thus the firing probability is given by De Morgan's Law

[9] We also found that a was often proportional to the beam intensity – especially for cells near the beam axis. CITADL included this effect as well.

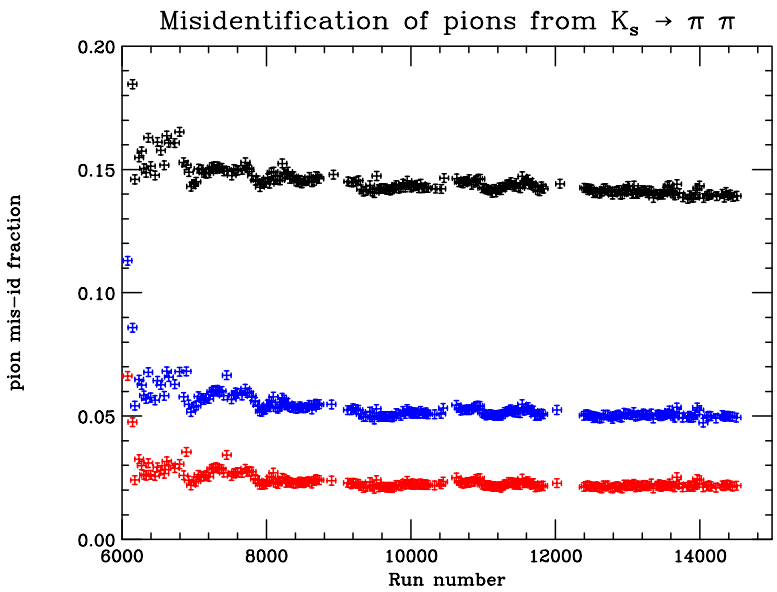

Figure 3.3: The fraction of times that a pions from $K_s \to \pi^+\pi^-$ is misidentified as a kaon, proton, or electron for three different CITADL cuts. Each point is averaged over 25 runs.

enough to provide an accurate photoelectron re-calibration for nearly all of the 300 cells in the Čerenkov system.

Although not nearly as copious as our K_s sample, the decay $\Lambda \to P\pi^-$ provided an clean sample of proton and low momentum pion decays. Finally the decay $\phi \to K^+K^-$ was used to measure the Čerenkov identification of kaons on a run by run basis.[10] The run-by-run fraction of misidentified daughters from the K_s , Λ and ϕ decays for several Čerenkov cuts was used as a stability monitor of the Čerenkov system. Figure 3.3 and 3.4 show examples of these "misidentification" monitors.

We also found that it was possible to use golden mode charm as a monitor of Čerenkov performance. Figure 3.5 shows a 405,000 golden mode charm sample obtained (using about 75% of our data) without any Čerenkov cuts. [11] A selection of

[10]To obtain a clean enough ϕ sample to make a meaningful background subtraction, we required that one of the two kaons was Čerenkov identified.

[11]This data does not include some of the corrections required to put the D^o at its actual mass of

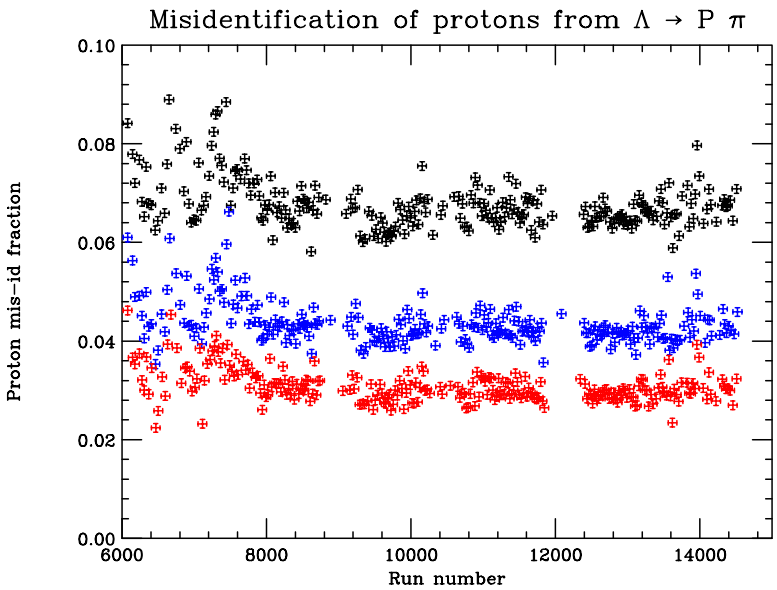

Figure 3.4: The fraction of times that a proton from $\Lambda \rightarrow P\pi^-$ is misidentified as a light particle for three different CITADL cuts. Each point is averaged over 25 runs.

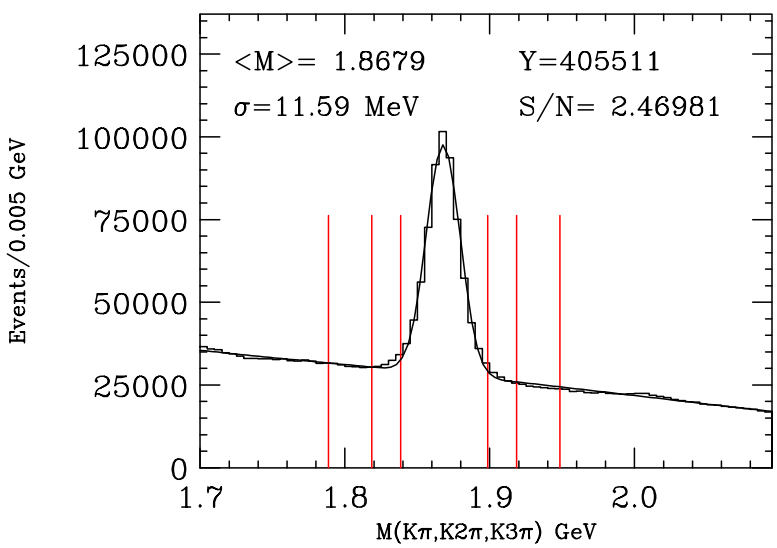

Figure 3.5: Invariant mass plot for three golden mode decays $D^0 \rightarrow K^-\pi^+, K^-\pi^+\pi^+\pi^-$, and $D^+ \rightarrow K^-\pi^+\pi^+$. The reconstructed D^+ mass was shifted by 5 MeV so that its peak will reconstruct in the same place as the peak of the D^0. This data has vertex quality, and kinematic cuts only. No Čerenkov cuts were used. The vertical lines denote signal and sideband regions which will be used to make a background subtraction.

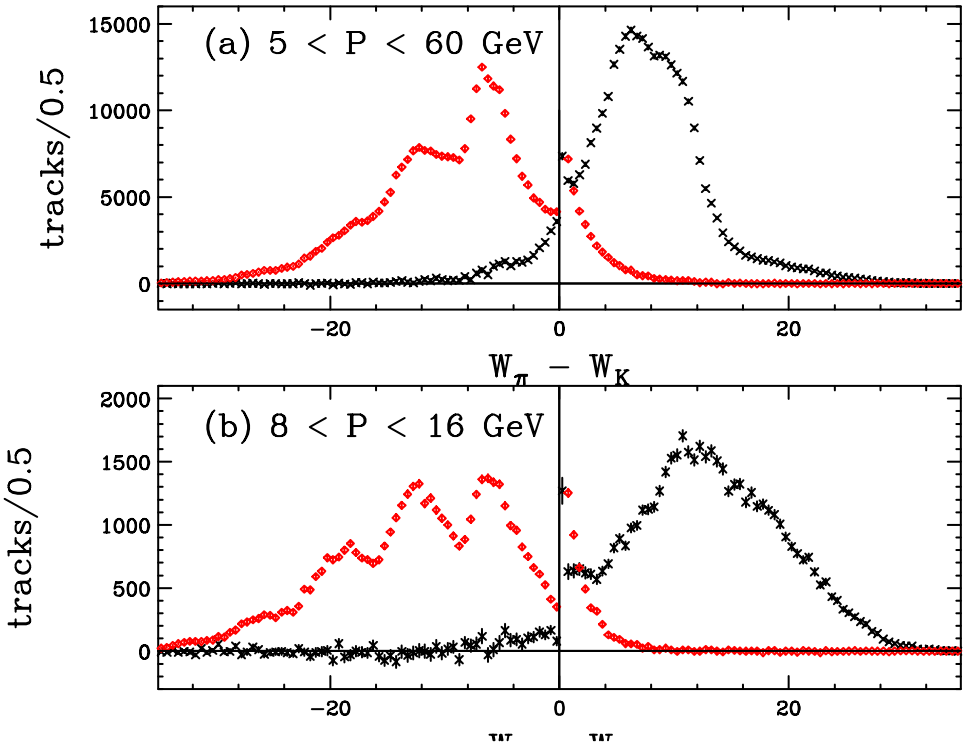

Figure 3.6: The log likelihood difference $W_\pi - W_K$ distribution obtained from background subtracted kaons and pions from golden mode charm signal shown in Figure 3.5. The pion distributions were rescaled to have the same area as the kaon distributions. Fig. (A) is for tracks with momenta in the range 5 < P < 60 GeV. Fig. (B) is for tracks with momenta in the range 9 < P < 16 GeV. There are off scale spikes in the 0 bin consisting of 20,000 and 4,500 events for Fig. (A) and (B).

cuts on vertex detachment, and isolation, the $D^{*+} - D^0$ mass difference, and momentum were used to obtain this reasonably clean sample. Also shown are sideband regions used for background subtraction. Figure 3.6 shows the likelihood difference $\Delta W_K = W_\pi - W_K$ for the kaon and pion daughters from these background subtracted charm decays for tracks with two ranges of momentum. For convenience, we will call the variable $\Delta W_K \equiv W_\pi - W_K$ "kaonicity". A positive kaonicity implies that a given track is more likely to be a kaon as opposed to a pion.

Figure 3.6(a) shows the kaonicity distribution for charm kaons and pions in a momentum range above the pion threshold of C2 (the lowest threshold counter) but below the kaon threshold of C3 (the highest threshold counter). Outside of this momentum range, the FOCUS Čerenkov system is incapable of much K-π separation and the kaonicity distribution is strongly peaked near zero.[12] Figure 3.6(b) shows the kaonicity distribution in the more restricted range from 9 to 16 GeV. In this range kaon-pion discrimination is particularly effective since it lies above the pion threshold for C1 but below the kaon threshold of C2.

Figure 3.6 shows that even though the likelihoods are constructed from the discrete firings of Čerenkov cells, the kaonicity distribution for kaons is reasonably continuous except near $\Delta W_K = 0$. As Figure 3.6(a) shows, averaged over the accepted charm momentum spectrum, pion backgrounds to kaons can be very effectively eliminated while still maintaining high efficiency for charm kaons. A cut just above kaonicity of zero rejects a large fraction of pions. The fraction of background pions then dies away exponentially for $\Delta W_K > 0$ beyond zero. Over the more restricted range from

1.864.

[12] But CITADL offers some slight K-π discrimination outside of this range since it can exploit the momentum dependence of photoelectron yield beyond the C3 kaon threshold: *ie* the threshold is not infinitely sharp.

9 to 16 GeV, where cells from both C1 and C2 discriminate pions from kaons, the ΔW_K distribution for kaons broadens considerably. One can make a very stringent kaonicity cut to suppress pion backgrounds and still maintain good efficiency for real kaons.

The situation for pion identification is essentially the mirror image of that for kaons. The contamination of kaons into the $\Delta W_K < 0$ region falls off exponentially in ΔW_K, while the pion spectrum extends below $\Delta W_K < -20$. In the region from 9 to 16 GeV, where both C1 and C2 discriminate pions from kaons, the kaonicity distributions significantly broaden out allowing to one to make more stringent cuts to reduce misidentification.

Using Čerenkov Information to Reduce Charm Backgrounds

As Figure 3.5 shows, it was indeed possible to get reasonably clean charm signals without the use of Čerenkov information. However, many FOCUS analyses employed Čerenkov cuts as an effective way of increasing signal to noise, while maintaining reasonable efficiency. Figure 3.7 illustrates the effectiveness of kaon and pion Čerenkov cuts for $D^0 \to K^-\pi^+\pi^+\pi^+$ events selected using an $\ell/\sigma > 9$ detachment cut but without any Čerenkov cuts. The kaon cut is on "kaonicity" or the log likelihood difference $\Delta W_K \equiv W_\pi - W_K$ discussed previously. The pion cut is based on a variable which we will call "piconicity" or $\Delta W_\pi \equiv W_{\rm min} - W_\pi$. The ΔW_π cut is placed on all D decay pions and is meant to insure that no pion being considered as a charm daughter is grossly inconsistent with the pion hypothesis.[13] A cut such as $\Delta W_\pi > -2$

[13] We generally use a consistency cut rather than demanding that the pion is favored over both the kaon and electron hypothesis since the momentum range at which pions can can be distinguished from electrons is below 17 GeV for tracks traversing all three Čerenkov counters and below 8.5 GeV for 3 chamber pions which traverse only C1 and C2.

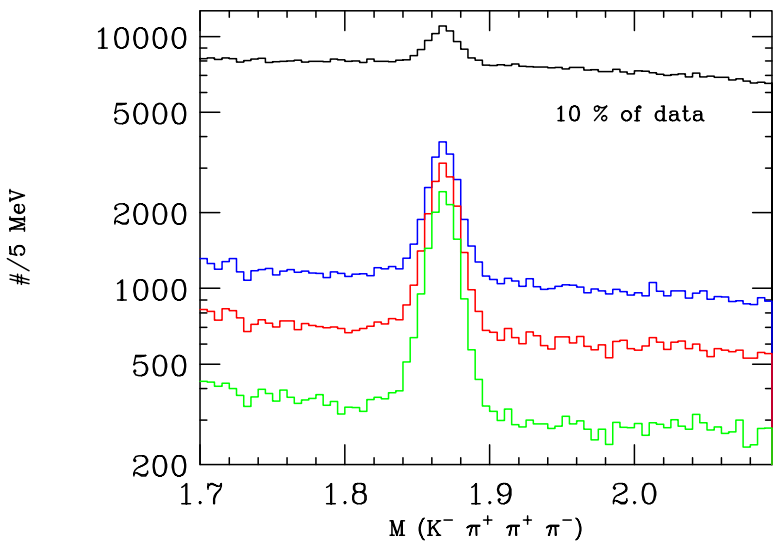

Figure 3.7: Illustration of the effectiveness of Čerenkov cuts in reducing backgrounds to $D^0 \to K^-\pi^+\pi^+\pi^-$. Note the logarithmic scale. The upper curve has no Čerenkov cuts. The second histogram requires $\Delta W_K > 0$. The third requires $\Delta W_K > 2$. The fourth histogram requires $\Delta W_K > 2$ and $\Delta W_\pi > -2$. The fitted signal yields in these plots are 15307, 12783, 11699, and 9996 respectively.

means that none of the other 3 particle hypotheses is favored over the pion hypothesis by more than a factor of $\exp(2/2) = 2.71$. For the $D^0 \to K^-\pi^+\pi^+\pi^+$ sample the requirement that $\Delta W_K > 0$ preserves 84 % of the yield while increasing the signal to noise by a factor of 6.2.The more stringent $\Delta W_K > 2$ and $\Delta W_\pi > -2$ preserves 75% of the uncut signal yield but increases the signal to noise by a factor of 16.

One of the goals of the CITADL algorithm, was to be much more efficient than LOGIC in suppressing the number of kaons which are misidentified as pions to enable us to more effectively study Cabibbo suppressed decays. An example of such a process is the $D^0 \to \pi^+\pi^-$ which is plagued by a large misidentification background from misidentified $D^0 \to K^+\pi^-$ decays which occur with approximately 25 times the branching ratio as $D^0 \to \pi^+\pi^-$. Figure 3.8 compares the dipion mass spectrum from the published E687 signal to a version from half of the FOCUS data set. The E687

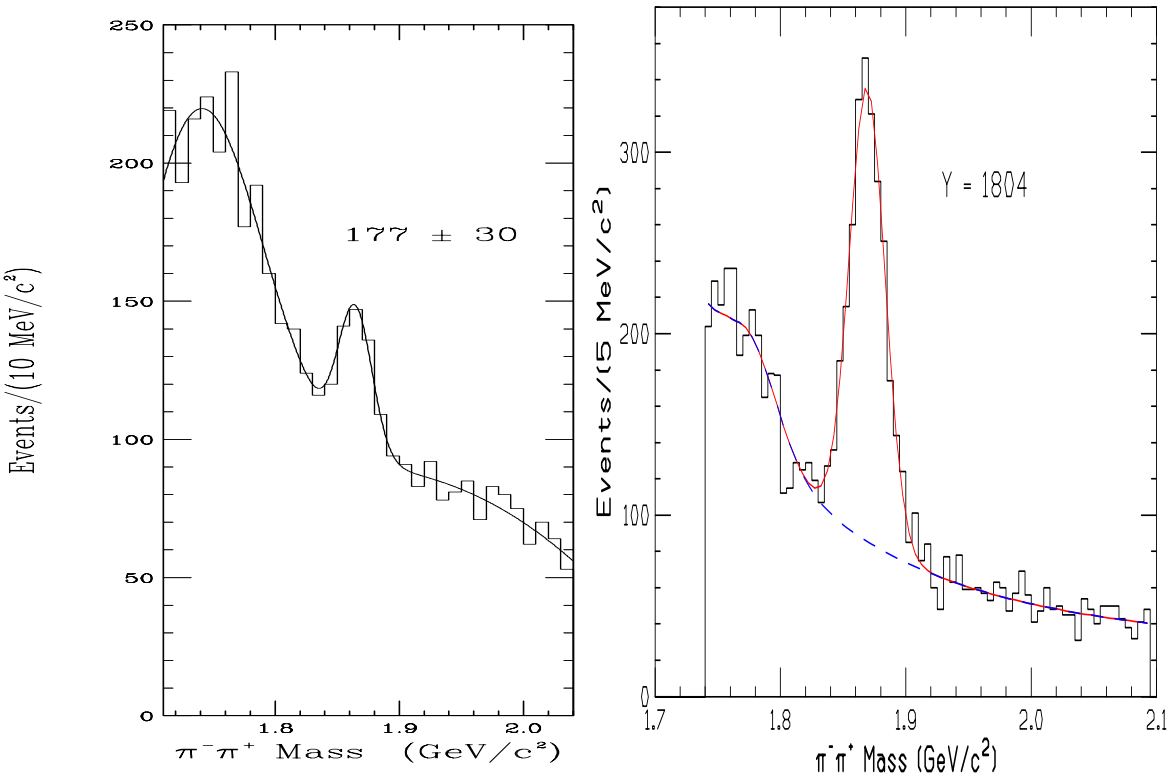

Figure 3.8: (Left) E687 signal for $D^0 \to \pi^+\pi^-$ from Reference [15]. The massive distortion in the background at lower masses is due contamination from misidentified $D^0 \to K^+\pi^-$. (Right) FOCUS signal for $D^0 \to \pi^+\pi^-$ from half of our data set.

sample used LOGIC. The FOCUS sample required $W_K - W_\pi > 3$ for both pions in order to significantly reduce $D^0 \to K^+\pi^-$ contamination. Much of the improvement in event yield is due to the fact that FOCUS took roughly a factor of 15 times the E687 data set. We also have required that the dipion vertex is outside of the FOCUS target material to further increase our signal to noise relative to E687.

Figure 3.9 is an example of a plot used to gauge the effectiveness of a set of Čerenkov cuts on the pions and kaons from a very small sample of $D^+ \to K^-\pi^+\pi^+$ decays. The data satisfied our standard skim cuts for this mode: a good quality vertex intersection (CL > 1 %) , a kaon cut of $\Delta W_K > 0.5$, and a secondary to primary detachment exceeding 2.5 standard deviations ($\ell/\sigma > 2.5$). This particular plot used

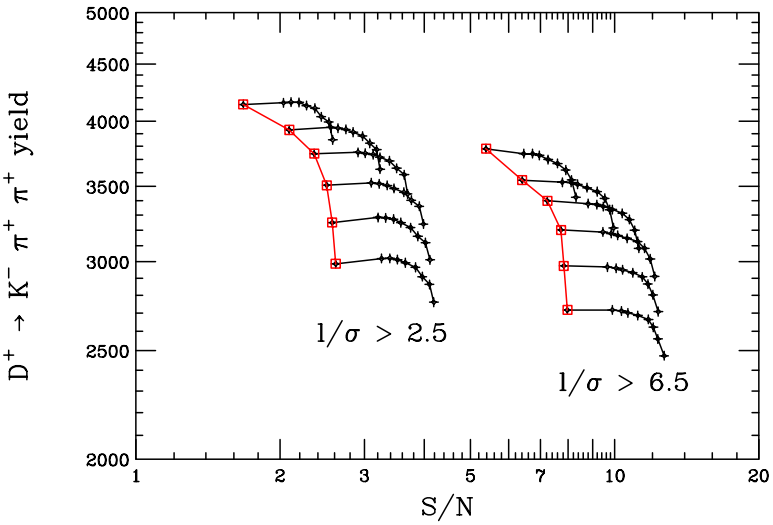

Figure 3.9: Illustration of the effectiveness of Čerenkov cuts in reducing backgrounds to $D^+ \to K^-\pi^+\pi^+$ which verticize outside of the target microscrips and target material. We plot the signal yield versus S/N for two different detachment cuts and several cuts on kaonicity and pioconicity. The kaonicity cuts (red) range from $\Delta W_K > 0.5, 1, 2, 3, 4, 5$. The piconicy (black) cuts are no cut, $\Delta W_\pi > -10, -9, ..., -3$. Only 2 % of the our complete data was used for this plot.

the sample of D^+ decays which verticized outside of the target material and target microstrip system to remove backgrounds from multiple interactions. We show the yield versus signal to noise for 2 detachment cuts, and a sequence of Čerenkov cuts on the kaons and pions. [14] Figure 3.9 shows that the "piconicity cut" is essentially as effective a cut as the kaonicity cut. Figure 3.9 also shows that the Čerenkov cuts increase the signal to noise by a nearly constant factor at the two detachment cuts being considered.

[14]Both the yields and signal to noise were based on fits to a Gaussian signal over a polynomial background. We define the signal to noise ratio as the ratio of the fitted number of signal events at the peak over the fitted number of background events at the peak mass.

3.3 Vee Reconstruction

Neutral Kaon, K^0 and its charge conjugate $\bar{K}^0$ decay to the K_s about 50% of the time and K_L another 50%. The K_s meson is called a vee and decays to two charged particles, primarily (about 69% of the time to π^+ and π^-.) These charged tracks may first be detected in the SSD or MPWC system. The K_s vees are classified primarily into four classes, each having a unique vee-finding algorithm depending on the topology of the decay.

3.3.1 SSD Vees

The "SSD vees" decay upstream of microstrip vertex. These vees are searched for using the DVERT algorithm. Each track is assigned a pion mass and the invariant mass is required to be consistent with the K_s mass. The SSD vees are the highest resolution vees because they verticize upstream of the microstrips and therefore have low momentum and thus by virtue of Eq. 3.2 and 3.3 have very good momentum resolution. This is also the only vee class with good vertex resolution since the SSD vees contain microvertex (SSD) information.

3.3.2 MIC Vees

The "MIC vees" decay inside the microstrip vertex, in the region between the second and fourth stations. The search for "MIC vees" is performed by projecting unlinked PWC tracks to to the 4th and 3rd SSD stations. Unused triplets in each stations are tested with the extrapolated PWC track. If the triplets are found for the PWC track, the track parameters are refit. For each PWC track there may be more than one triplet candidates in which case a global fit is performed to all the hits that are associated with the track and the candidate with the smaller χ^2 is selected. Again,

Each track is assigned a pion mass and the dipion invariant mass is required to be consistent with the K_s mass.

3.3.3 M1 Vees

The "M1 vees" decay inside the M1 magnetic field, between the microstrip vertex detector and the first PWC station. These vees lack SSD information but have complete PWC track information. The "M1 vees" fall in three topologies, track-track (TT) which consist of two 5-chamber tracks, track-stub (TS) which consist of one 5-chamber and one 3-chamber tracks, and stub-stub (SS) which consist of two 3-chamber tracks. The construction of all three classes of vees is performed by tracing the track's X-view projections to get an estimated vertex position of the vee in x-z plane. Except for the TT vees, the vertex position comparisons can only be made for the x track (non-bend) projections using the magnetic field. For the TT vees both track momentum are known and an invariant mass test can be performed. For the TS vees the momentum of the 5-chamber track is known, and the momentum of the 3-chamber track can be determined by using the y position of the vertex which is constructed using the momentum of the 5-chamber track. For SS vees, it is assumed that the vee is originated from the highest multiplicity vertex which is formed using SSD tracks with no MCS information. Using the position of primary and secondary vertex information the momentum for both tracks can be determined. After the best momentum and vertex positions are obtained, the tracks are fit using full track covariance matrix. The χ^2 include a contribution that requires the vee point back to the primary vertex.

3.4 Data Reconstruction and Skims

During the 1996-97 run, FOCUS collected about 6.5 billion photon triggers on about 6000 $8mm$ magnetic tapes. Because of a large amount of data the reconstruction and skimming process of data consisted of three stages, as described below.

3.4.1 Pass1

The Pass1 reconstruction process consisted of analyzing the raw data and writing the reconstructed data on another set of 6000 $8\,mm$ magnetic tapes. Pass1 reconstruction required running the reconstruction algorithms for all the detectors.

A Fermilab software product called CPS (Cooperative Process Software) was employed to construct a "farm" consisting of a "server" node and about 10 "worker" nodes. This increased the computing power substantially allowing the Pass1 processing to occur in parallel.

Up to eight computing "farms" at Fermilab consisting of up to 90 worker nodes were employed for the Pass1. The types of workstations used included SGI workstations based on the MIPS R5000 CPU and IBM workstations based on the IBM/Motorola PowerPC CPU.

3.4.2 Skim1

The purpose of skim1 is to divide the data into smaller data set, each set containing data based on various classes of physics, see Table 3.1. This skim divided the pass1 data set to six super-streams. Each super-stream consisted of 200-500 $8\,mm$ magnetic tapes.

University of Colorado and Vanderbilt University ran the skim1 on two computer clusters of about 4000 MIPS each, which began in October, 98 and finished in Febru-

Table 3.1: Super-stream Descriptions

Superstream	Description	Skim2 Institution
1	Semi-leptonic	Puerto Rico
2	Global Vertex and K_s	Illinois
3	EM Neutrals and ϕ Skims	CPBF, Brazil
4	Baryons	Fermilab
5	Diffractive, Leptonic and Out-of-Target	California, Davis
6	Fully Reconstructible Charm Decay Modes	California, Davis

ary 99.

3.4.3 Skim2

Skim2 constitutes the final skimming stage, where the skim1 output tapes were further split into smaller skims with a more specific physics topics. Generally, 5-12 sub-streams were written from each super-stream. The skim2 was done in five institutions, listed in Table 3.1, and it began in January 99 and were completed by June 99. In this analysis the sub-stream one from super-stream 6 (general meson sub-stream)is used.

Super-stream 6 uses DVERT to reduce the sample size by about a factor of 20. The selection is very efficient for specific all charged meson final states.[15] The specific skim cuts varied somewhat as a function of final states but for most final states with a final state kaon the criteria was a detachment cut of $\ell/\sigma > 2.5$, kaonicity of $\Delta W_K > 0.5$, and reconstructed mass between 1.7 and 2.1 GeV/c^2. Somewhat loser cuts were used for D^0 states consistent with arising from $D^{*0} \to D^0\pi^+$ decay. States

[15] Although some baryon modes were included as well.

featuring s K_s^o were included only if the K_s^o satisfied an additional set cuts known as the "GOODKS" cuts. These include a tight cut on the χ^2 of the Vee fit and a tighter cut on the "normalized" K_s^o mass.[16]

In order to save subsequent reprocessing time, much of the skimming information was saved on tape in a SEZDEE block which included information on the primary vertex, and secondary vertex. The SEZDEE block along with a DST (Data Summary Tape block) formed the bulk of the information saved on skimmed data for further processing. The DST included the CITADL particle identification information, as well as momentum information for all reconstructed tracks in the event.

[16]The normalized mass is the reconstructed mass minus the nominal mass divided by the event-by-event RMS mass resolution.

Chapter 4

The $D^+, D_s^+ \to K^+K^-\pi^+$ Dalitz Analysis

Results from D^+ and $D_s^+ \to K^+K^-\pi^+$ (and charge conjugate) Dalitz analysis are presented and compared with the $E687$ analysis [2]. For both the D^+ and D_s^+ we show that the K^+K^- spectrum is dominated by intermediate ϕ resonances and $K^-\pi^+$ spectrum is dominated by $\bar{K}^*(892)^0$ resonance. This dominance is especially strong for the D_s^+ while the D^+ has a larger fraction of broad resonance contributions. In both cases there is evidence for a contribution from $f_0(980)\pi^+$ and the $f_J(1710)\pi^+$ – two states that were included in the E687 fit of the D_s^+ Dalitz plot but **not** originally included in the E687 fit of the D^+ Dalitz plot. A very visible interference pattern is evident in the D^+ Dalitz plot which is due to the interference of a $\bar{K}^*(890)K^+$ and a broad scalar resonance which E687 attributed to the $\bar{K}^*(1420)K^+$. We also get reasonable fits with this choice although the exact phase and amplitude depends critically on the choice of additional resonances. We find a clear pattern of discrepancy between the data and our best model indicating an incomplete understanding of this decay. In both FOCUS and in E687, the particular resonance choice is based on a

visual inspection of the Dalitz density.

We begin by describing the nature of the analysis cuts used to obtain the D^+ and D_s^+ signals and the reasons for some of these cuts. Next, we present a description of the analysis formalism followed by a discussion of the background parameterization method and method we use for efficiency correction. We next present the two Dalitz plots and argue for our particular resonance choice and conclude by presenting our fit results on $D^+, D_s^+ \to K^+K^-\pi^+$. A treatment of additional sources of statistical and systematic errors will be discussed in Chapter 6 and 7.

4.1 The $D^+, D_s^+ \to K^+K^-\pi^+$ Signal

We began by making a local skim of the SEZDEE skim tapes (see 3.4) with somewhat tighter cuts on detachment and kaonicity. We specifically took $K^+K^-\pi^+$ events satisfying a kaonicity of $W_K > 1$ and a detachment of $\ell/\sigma_\ell > 3$ and someone tighter secondary vertex confidence level (DCL) cut of greater than 1%. This initial skim was made to allow us to keep our data on disk in the form of n-tuples.

Our "standard" D^+ signal required a relatively tight detachment cut of $(\ell/\sigma_\ell > 9)$ and a tight kaonicity cut of $\Delta W_K > 3$. Increasing the detachment cut is our primary way of reducing non-charm backgrounds. A tight kaonicity cut was motivated by the desire to suppress charm reflections such as those from such copious, misidentified, Cabibbo allowed decays as $D^+ \to K^-\pi^+\pi^+$ which have only a single kaon in the final state. The confidence level that the tracks from the secondary vertex form a vertex with the primary vertex tracks is required to be less than 0.1%(CL1). This cut is very effective in eliminating the contamination from the decay chain $D^{*+} \to D^0\pi^+ \to (K^+K^-)\pi^+$ which has the same final state as this analysis along with incompletely

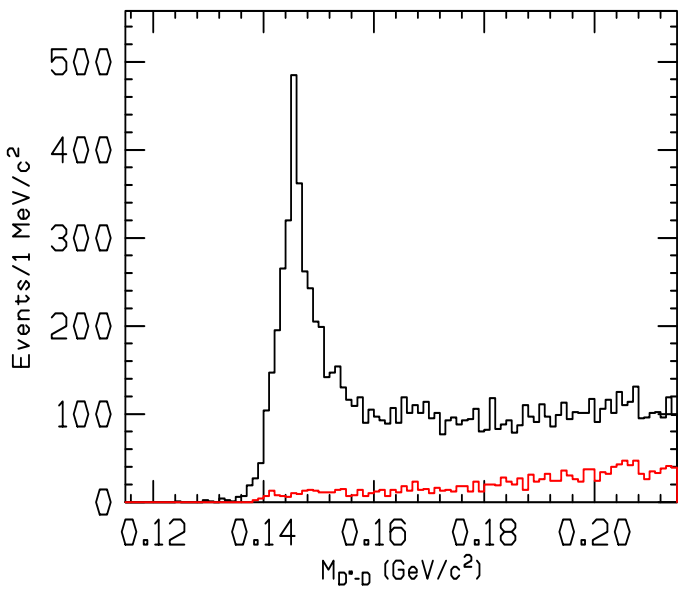

Figure 4.1: The black plot shows the $D^{*+} - D^{+}$ mass histogram and the red plot shows the same mass histogram after the primary isolation (CL1) cut is applied. These combinations satisfy our standard D^{+} cuts and are reconstructed in the broad mass range $1.7 < M(K^{+}K^{-}\pi^{+}) < 2.1\ GeV/c^{2}$

reconstructed D^{*} decays into states such as $D^{*+} \rightarrow D^{0}\pi^{+} \rightarrow (K^{+}K^{-}\pi^{0})\pi^{+}$.[1] Figure 4.1 demonstrates this fact by showing the mass difference plot of D^{*+} and D^{+}. The peak in black histogram near $0.15\,GeV/c^{2}$ represents background form the D^{*+} decay chain. The red histogram shows that the primary isolation cut effectively eliminates this background.

To further insure that the secondary vertex is well isolated, a confidence level that any other track that is not in primary, forms a vertex with the secondary to be less than 0.01% (CL2). This cut eliminates backgrounds from higher multiplicity final states such as $D^{0} \rightarrow (K^{-}K^{+}\pi^{+})\ \pi^{-}$ where the tracks within parenthesis are of our desired topology. In order to reduce proton as kaon misidentification, we demand a

[1] In spite of the missing π^{0} such a reflection will contribute to a somewhat broader peak in the $D^{*} - D$ mass difference.

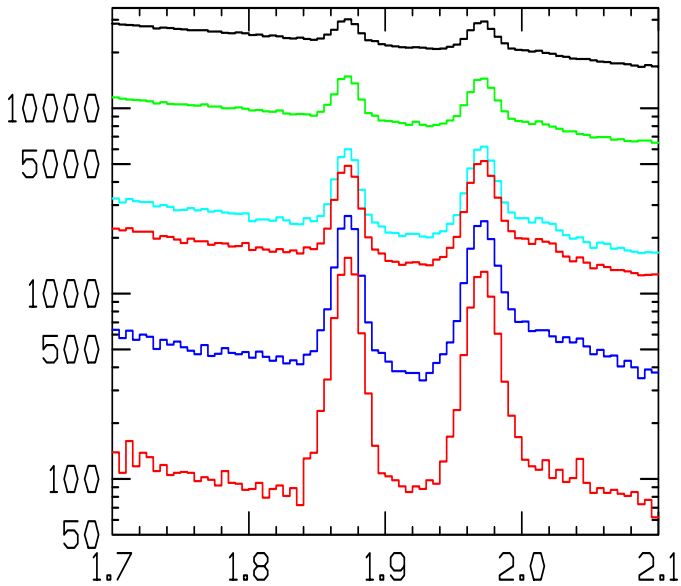

Figure 4.2: Signal development for $D_s^+ \rightarrow K^+K^-\pi^+$ starting with no cuts, $l/\sigma > 9$, # of $\sigma\, OOT > 3$, $CL2 < 0.01$, $CL1 < 0.001$, and $\Delta W_k > 5$

very loose "kaon not proton" cut of greater than -6, $\Delta W_P = W_P - W_K > -6$. We are able to exploit our segmented target, and massively reduce non-charm background by requiring that the secondary vertex be outside of the target material by at least 3 σ.

Figure 4.2 shows the signal as cuts are successively applied to the sample in our original skim. These additional cuts create a factor of ≈ 250 reduction in the background level. Comparison of the two lowest histogram demonstrates the effectiveness of a $\Delta W_K > 5$ cut in removing the "tail" due to Cerenkov mis-identified $D^+ \rightarrow K^-\pi^+\pi^+$ events which populates the high side of the D_s^+ peak. The mass histograms for $D^+ \rightarrow K^+K^-\pi^+$ with and without the "out of material cut" shown in Figure 4.3 illustrates the effectiveness of the "out of material cut" by contrasting a clean $K^-\pi^+\pi^+$ signal with and without the OOT cut.

Table 4.1 summarizes properties of the two signals obtained using our standard

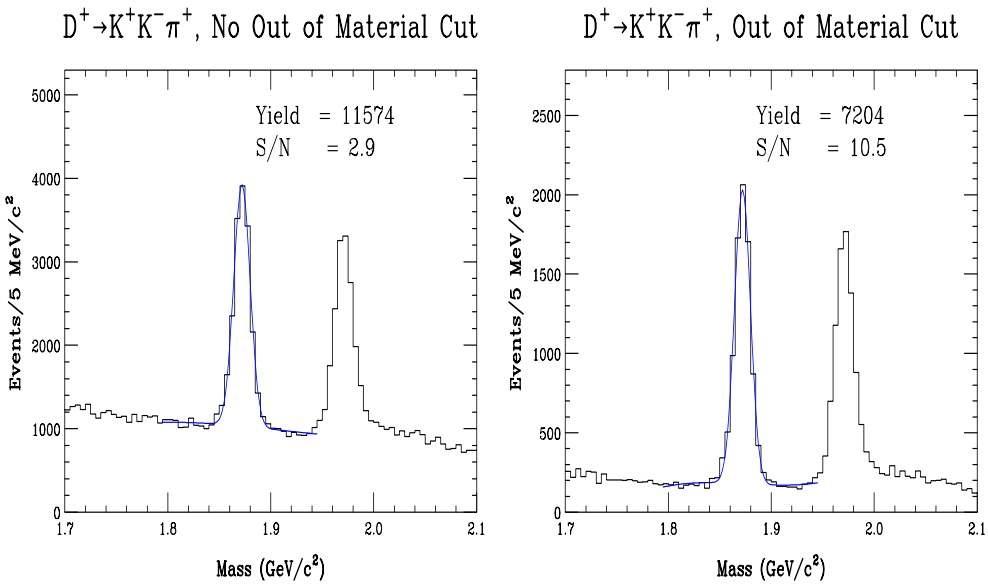

Figure 4.3: Mass histograms of full data set for $D^+ \rightarrow K^+K^-\pi^+$ with and without "out of material cut".

Table 4.1: D^+ and D_s^+ signal properties

Parameter	D^+	D_s^+
Fitted Yield	7098 ± 109	6827 ± 117
Fitted Mass (GeV/c^2)	$1.8721 \pm .0001$	1.9711 ± 0.0001
Width σ $GeV/c^2)$	0.00753 ± 0.00012	$0.00886 \pm .00015$
Signal Fraction F_0	0.89	0.80

Table 4.2: Signal and Sideband Region Limits

Region	Mass cut (GeV/c^2)	events
D^+ low sideband	$1.805 < m < 1.837$	1093
D^+ signal region	$1.8592 < m < 1.885$	7457
D^+ high sideband	$1.893 < m < 1.925$	1110
D_s^+ low sideband	$1.905 < m < 1.941$	1190
D_s^+ signal region	$1.956 < m < 1.986$	7591
D_s^+ high sideband	$2.004 < m < 2.040$	1749

cuts. The yield, mass[2], and width are obtained by fitting each sample to a Gaussian plus a polynomial. The signal fraction F_o is defined as the integral of the signal peak, divided by the total number of events in a signal region which is defined in Table 4.1. To characterize the background, each sample is subdivided to sideband and signal regions and the sidebands are fit. The limits for the signal and sideband regions are specified in Table 4.2.

4.2 The D^+ and $D_s^+ \to K^+K^-\pi^+$ Analysis Formalism

We illustrate the formalism using one of our $D^+ \to K^+K^-\pi^+$ fits.

In this fit, the decay amplitude is described as a coherent superposition of $\bar{K}^*(890)^0$,

[2]Because of low-level alignment and magnetic problems present in our code during our primary data reconstruction, we have a slight (3 MeV/c^2) shift in our average masses compared to the world's average. Although "correction" routines which put our peaks at the correct mass exist, they were not applied in this work.

$f_0(980)$, ϕ, and $\bar{K}^*(1430)$ amplitudes as follows:

$$\begin{aligned}
\mathcal{A}(D^+ \to K^+K^-\pi^+)_s &= a_{\bar{K}^*(890)^0} e^{i\delta_{\bar{K}^*(890)^0}} P(\pi^+K^-K^+|\bar{K}^*(890)^0) \\
&+ a_{f_0(980)} e^{i\delta_{f_0(980)}} S(K^+K^-\pi^+|f_0(980)) \\
&+ a_\phi e^{i\delta_\phi} P((K^+K^-\pi^+|\phi) \\
&+ a_{\bar{K}_0^*(1430)} e^{i\delta_{\bar{K}_0^*(1430)}} S(\pi^+K^-K^+|\bar{K}_0^*(1430))
\end{aligned} \tag{4.1}$$

Where S and P stand for s-wave (orbital angular momentum of zero) and p-wave (orbital angular momentum of one) resonances. The amplitude for $D^- \to K^-K^+\pi^-$ is obtained in Equation 4.1 by replacing particles with their respective anti-particles. This assumes that the CP violation is negligible for D mesons [3]:

$$\begin{aligned}
\mathcal{A}(D^- \to K^-K^+\pi^-)_s &= a_{K^*(890)^0} e^{i\delta_{k^*(890)^0}} P(\pi^-K^+K^-|K^*(890)^0) \\
&+ a_{f_0(980)} e^{i\delta_{f_0(980)}} S(K^-K^+\pi^-|f_0(980)) \\
&+ a_\phi e^{i\delta_\phi} P((K^-K^+\pi^-|\phi) \\
&+ a_{\bar{k}_0^*(1430)} e^{i\delta_{k_0^*(1430)}} S(\pi^+K^-K^+|k_0^*(1430))
\end{aligned} \tag{4.2}$$

Note that CP invariance implies that the relative phase shifts δ_ϕ and $\delta_{k_0^*(1430)}$ are not changed in going from particle to antiparticle and the amplitudes are the same as well. We have argued in Chapter 1 that these phase shifts are actually the strong phase shifts from final state interactions.

The goal of the fit is to determine the phases δ_i and amplitudes a_i. The observed signal probability density function PDF_s is the product of A_s with its complex conjugate A_s^*:

$$\mathrm{PDF}_s(m^2_{K^-K^+}, m_{K^-\pi^+}) = \epsilon(m^2_{K^-K^+}, m_{K^-\pi^+}) \times \frac{\mathcal{A}_s\mathcal{A}_s^*}{\mathcal{N}_s} \tag{4.3}$$

where $\epsilon(m^2_{k^-k^+}, m_{k^-\pi^+})$ is the efficiency function as described below, and $\mathcal{N}_s$ is the the normalization constant which is obtained by integral of $\epsilon \times \mathcal{A}_s\mathcal{A}_s^*$ over the Dalitz plot:

$$\mathcal{N}_s = \int_{DalitzPlot} \epsilon(m^2_{K^-K^+}, m_{K^-\pi^+})\ \mathcal{A}_s\mathcal{A}_s^*\ dm^2_{k^+K^-}\ dm^2_{K^-\pi^+} \tag{4.4}$$

The best estimate for phases δ_i and amplitudes a_i are obtained using maximum likelihood method. The likelihood is the product of probabilities for each observation in the entire Dalitz plot:

$$\mathcal{L}_{sr}(\vec{x};\vec{\alpha}) = \prod_{i=1}^{\mathcal{N}_s+\mathcal{N}_{bg}} \mathrm{PDF}_i. \tag{4.5}$$

In this equation, the signal region likelihood is the function of observed variables $\vec{x}$ which are $\{m^2_{K^+K^-}, m^2_{K^-\pi^+}\}$ and the fit parameters α_i which are the phases δ_i and amplitudes a_i. We find those amplitude parameters which maximize $\mathcal{L}_{sr}$. Because the probability of observing any particular event is far less than unity, the product of a large number of such probabilities (one for each event) may be very small number, and perhaps too small for the computer to handle. To avoid problems like this, we minimize the $w_{sr} = -2ln\mathcal{L}_{sr}$ to obtain the fit parameters. The -2 is included in the definition of w_{sr} so that it resembles a χ^2-like variable in the sense that minimizing w_{sr} maximizes the likelihood. The factor of two is included so that the standard definition of error corresponds to a $\Delta w_{\mathrm{sr}} = 1$.[3]

The likelihood function that is minimized includes both the signal and background events in the signal region. This is because the events in the signal region could be from the $D^+ \to K^+K^-\pi^+$ or they could just be background events. Therefore, to account for this we a term for the background events in the probability distribution function is included:

[3]This correspondence becomes apparent if one applies it to a Gaussian likelihood: $w = -2\ln\left(\exp(-.5 * (x - x_o)^2/\sigma_o^2)\right) = (x - x_o)^2/\sigma_o^2 = \chi^2$.

$$\mathrm{PDF}(m^2_{K^-K^+}, m_{K^-\pi^+}) = \epsilon(m^2_{K^-K^+}, m_{K^-\pi^+})\mathcal{F}\frac{\mathcal{A}_s\mathcal{A}_s^*}{\mathcal{N}_s} + (1-\mathcal{F})\frac{\mathcal{I}_{bg}}{\mathcal{N}_{bg}} \tag{4.6}$$

The observation that identifying an event as "signal" or "background" are mutually exclusive occurrences is used here. Therefore, these contributions to the PDF must separately be normalized and modified by the probability that an event is signal $\mathcal{F}$ or background $1-\mathcal{F}$. Also note that the efficiency correction ϵ only modulates the signal part of the PDF. Because the parameterization of $\mathcal{I}_{bg}$ is made directly from the data, there is no need to include an efficiency correction in the second term $(1-\mathcal{F})\frac{\mathcal{I}_{bg}}{\mathcal{N}_{bg}}$. The normalization integral $\mathcal{N}_{bg}$ is explicitly written as:[4]

$$\mathcal{N}_{bg} = \int\limits_{DalitzPlot} \mathcal{I}_{bg}\ dm^2_{K^+K^-}\ dm^2_{K^-\pi^+} \tag{4.7}$$

Parameterization of the background involves fitting the sideband events to $\mathcal{I}_{bg}$.

The function that is minimized then takes the following form:

$$\begin{aligned} w_{sr} &= -2ln\mathcal{L}_{sr} \\ &= -2\sum_{i=1}^{\mathcal{N}_s+\mathcal{N}_{bg}} \ln\left[\epsilon_i\mathcal{F}\frac{\mathcal{A}_{s,i}\mathcal{A}^*_{s,i}}{\mathcal{N}_s} + (1-\mathcal{F})\frac{\mathcal{I}_{bg}}{\mathcal{N}_{bg}}\right] \end{aligned} \tag{4.8}$$

In order to allow for the inflation of statistical error bars due to background fluctuations, the fitter is allowed to adjust the background parameters. We handle the background in a variety of ways in this thesis. In one method, which we will call "guided" fits, a separate fit is performed for events in sideband regions in order to get

[4]Because the fit parameters are essentially multiplicative factors to fixed functions of the Dalitz variables, one can write the normalization in terms of amplitude products and pre-stored double integrals over products of S and P functions within the domain of the Dalitz boundary. These integrals are computed only once – at the beginning of the fit. It is not clear that one would have a practical fitting procedure if this were not the case.

an initial background parameterization. We next perform a fit to events in the signal region where both the signal, background, and signal fraction $\mathcal{F}$ are allowed to vary. Information from the previous background fit and the level for $\mathcal{F}$ is communicated to this fit through the use of likelihood penalty terms which appear in the last line of Eqn. 4.10.

$$\begin{aligned} w_{sr} &= -2ln\mathcal{L}_{sr} + \chi^2 terms \\ &= -2\sum_{i=1}^{\mathcal{N}_s+\mathcal{N}_{bg}} \ln\left[\epsilon_i \mathcal{F}\frac{\mathcal{A}_{s,i}\mathcal{A}^*_{s,i}}{\mathcal{N}_s} + (1-\mathcal{F})\frac{\mathcal{I}_{bg}}{\mathcal{N}_{bg}}\right] \\ &\quad + \sum_{\lambda,\kappa}(\beta_\lambda - \beta_\lambda^{(sb)})E^{-1}_{\lambda\kappa}(\beta_\kappa - \beta_\kappa^{(sb)}) + \left[\frac{\mathcal{F}-\mathcal{F}_0}{\sigma\mathcal{F}_0}\right]^2 \end{aligned} \tag{4.9}$$

The sum is over all the signal region events $\mathcal{N}_s + \mathcal{N}_{bg}$. The function shown in Eqn.. 4.10 is minimized by the fitter to determine the optimal values for phases δ_i and amplitudes a_i, $\mathcal{F}$ and β_i. The parameters $\beta^{(sb)}$ and their error matrix $E_{\lambda\kappa}$ are obtained from the sideband fits.

An alternative method, which we can use to assess systematics is to leave out either or both of the likelihood penalty terms in Eqn. (4.9) and derive all values from the fit to the signal region. Generally this "unguided" fit will produce larger error bars on the fit parameters.

4.2.1 Background Parameterization

The background in our final sample is due both to charm and non-charm sources. The sideband Dalitz plots of D^+ and D_s^+ show an increase in accumulation of points at ϕ and $K^*(892)^0$ mass regions, see Figure 4.5 and 4.7. Although the presence of the ϕ resonance is clear, most of the events in this region lack the clear nodal structure observed for the signal region in Figure 4.12. To a large extend the zero expected in the

middle of the ϕ band is populated. Our interpretation of this phenomena is that this background is due to ϕ's combined with random pions and therefore lack the quantum mechanical coherence to form states of definite angular momenta which ultimately creates the nodal structure. However, there do appear to be a remnants of the nodal structure in the sideband 3-D plots (Figures 4.4 and 4.6) which are reminiscent of the signal region (Figure 4.12) both in the presence of the Zemach lobes and their approximate asymmetry pattern. We attribute these events to signal charm events which smear into the sideband regions due to measurement error. Roughly 10 – 20 % of the ϕ region background is apparently due to this smearing.

We model the sideband intensity function by an incoherent sum of a phase space term and Breit-Wigner terms with no S or P (angular) factors:[5]

$$\begin{aligned} \mathcal{I}_{bg} &= 1 + |a_1\, BW_{\phi}(q)|^2 \\ &\quad + \left|a_2\, BW_{\bar{K}^*(890)^0}(q)\right|^2 \end{aligned} \tag{4.10}$$

The expression for the background intensity can be normalized as follow:

$$\mathrm{PDF}_{bg} = \frac{\mathcal{I}_{bg}}{\mathcal{N}_{bg}} \tag{4.11}$$

where $\mathcal{N}_{bg}$ is determined as follow:

$$\mathcal{N}_{bg} = \int\limits_{Dalitz\,Contour} \mathcal{I}_{bg}\left(m^2_{K^+K^-}, m^2_{K^-\pi^+}\right)\; dm^2_{K^+K^-}\; dm^2_{K^-\pi^+} \tag{4.12}$$

To obtain the starting values for the background parameters a_ia joint log likelihood fit to the high and low sideband data is performed. Therefore in the normalization Equation 4.12 the region of integration is determined by the Dalitz boundary calculated according to the central mass of the respective sideband. The sideband likelihood

[5]Admittedly since there is some nodal structure in the resonances this is a slightly imperfect modeling.

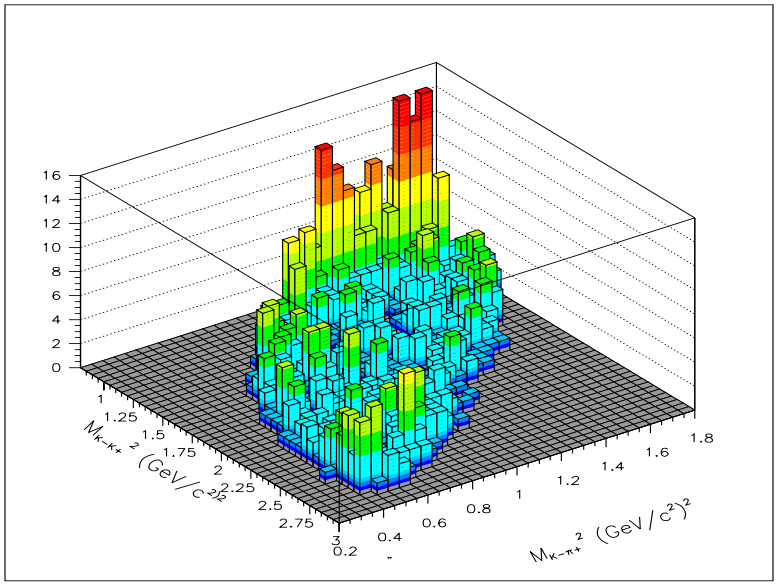

Figure 4.4: The 3-D dalitz plot of the Low sideband. The ϕ lobes are probably coming from the tail of the signal where it overlaps with sideband regions.

function has the form:

$$\mathcal{L}_{sb} = \prod_{i=1}^{\mathcal{N}_{sb}} \mathrm{PDF}_{bg,i} \tag{4.13}$$

The $-2ln\mathcal{L}_{sb}$ is minimized.

After a fit is done to the sidebands, the same form of background intensity function $\mathcal{I}_{bg}$ is used in Equation 4.10 and the fit is done to the signal region (with and without the likelihood penalty terms). When the fit is done to the signal region the normalization background integral 4.12 over the Dalitz boundary is calculated with respect to the central $KK\pi$ mass of the signal.

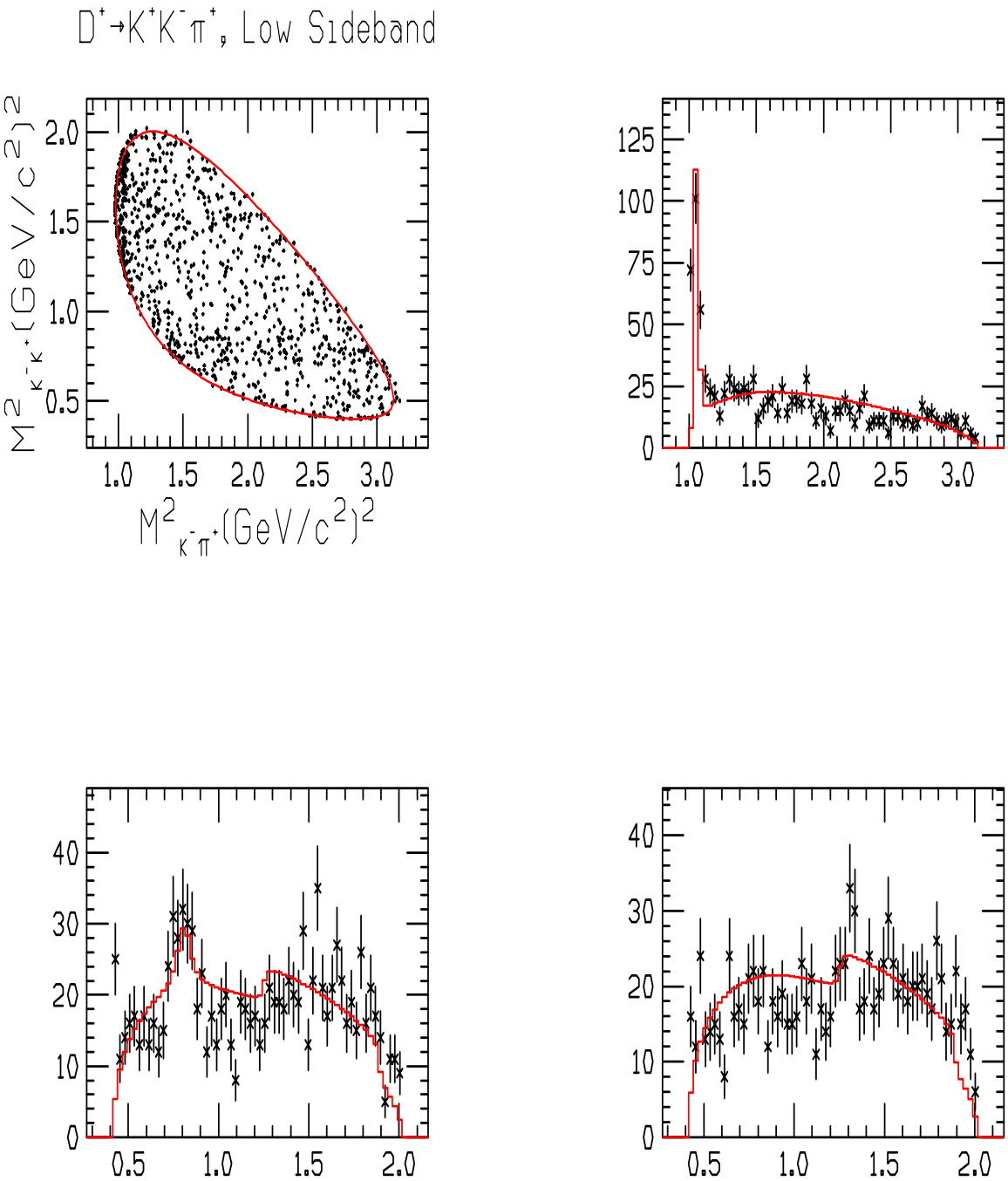

Figure 4.5: Low sideband Dalitz plots and projections for $D^+ \to K^+K^-\pi^+$. Points with error bars are data and the histograms in red are the predictions from a joint fit to low and high sideband. Observations of a nodal structure in the ϕ scatter plot is not expected from an incoherent source. The observed ϕ's lobes are probably due to tail of the signal where it overlaps with sideband regions.

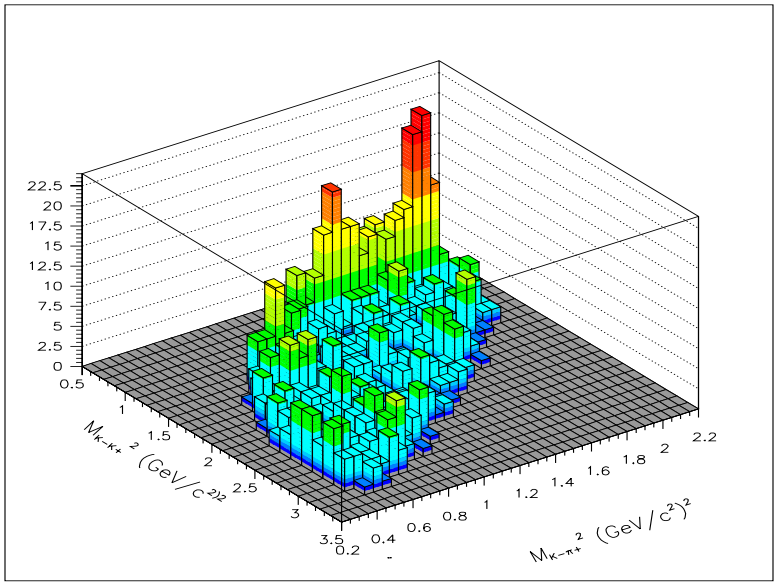

Figure 4.6: The 3-D dalitz plot of the high sideband. The ϕ lobes are probably coming from the tail of the signal where it where it smears into the sideband regions.

4.2.2 Efficiency Correction

The term $\epsilon(m^2_{K^-K^+}, m_{K^-\pi^+})$ in Equation 4.3 is included to correct for imperfect geometrical acceptance and reconstruction efficiency. A high statistics phase space Monte Carlo sample is used to compute the acceptance, where the particle is propagated through the simulated spectrometer and the output is analyzed using the FOCUS analysis software.

The mass histograms for the MC samples are shown in Figure 4.8. Each MC sample contains at least ten times the amount of data.[6]

Deviations from a uniform distribution of MC data on the Dalitz plot is attributed

[6]The Monte Carlo simulation was generated with a *uniform* acceptance rather than with the multi-resonant distribution observed in the data. As a result, in high intensity regions, the ratio of Monte Carlo intensity to data intensity may be far less than 10. We examine how finite Monte Carlo statistics effects the true statistical error in Section 6.

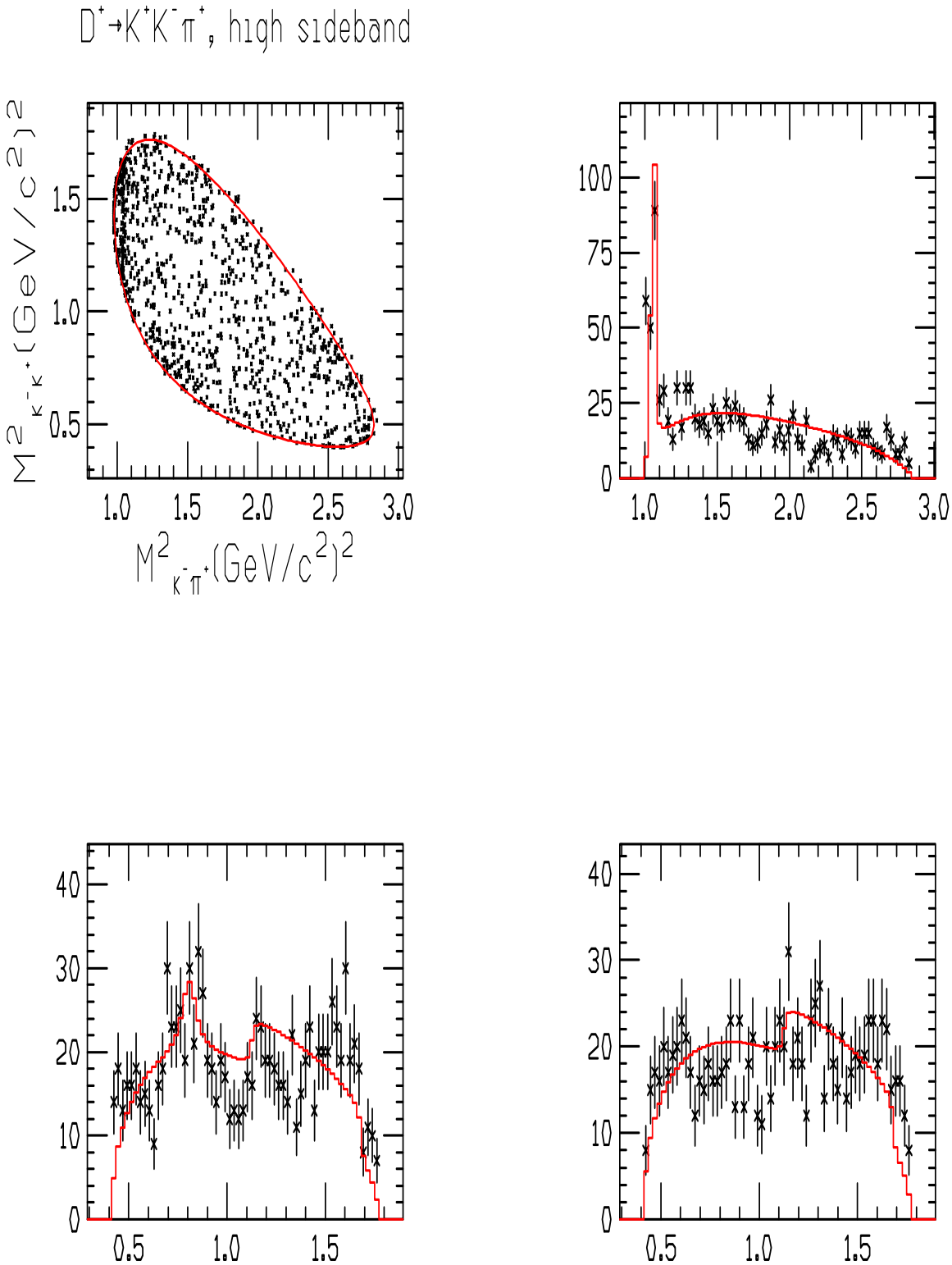

Figure 4.7: High sideband Dalitz plots and projections for $D^+ \to K^+K^-\pi^+$. Points with error bars are data and histograms in red are the predictions from a joint fit to low and high sideband.

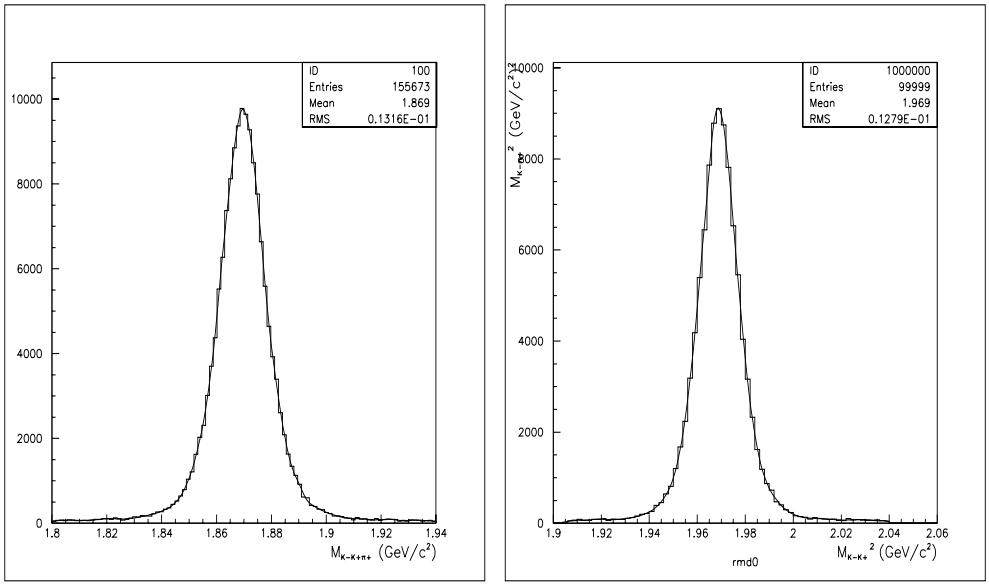

Figure 4.8: Phase space Monte Carlo signals and statistics for D^+ and $D_s^+ \rightarrow K^+K^-\pi^+$

to imperfect geometrical acceptance and reconstruction efficiency. The variations in intensity on the Dalitz plots in Figure 4.9 demonstrates the non-uniformities on the Dalitz scatter plots.

To obtain a non-parametric description of the efficiency, the Dalitz plot is subdivided into square bins. The efficiency of a given bin i, ϵ_i, is the number of reconstructed events over the area of the bin. The values for ϵ_i are shown is Figure 4.10 for the D^+. In the analysis program the ϵ_i's are stored in an array and a value is assigned to an event if it falls in the corresponding bin. Note that we do not need to worry about the absolute efficiency scale, since the normalization integral shown in Equation 4.4 contains the the ϵ as well.

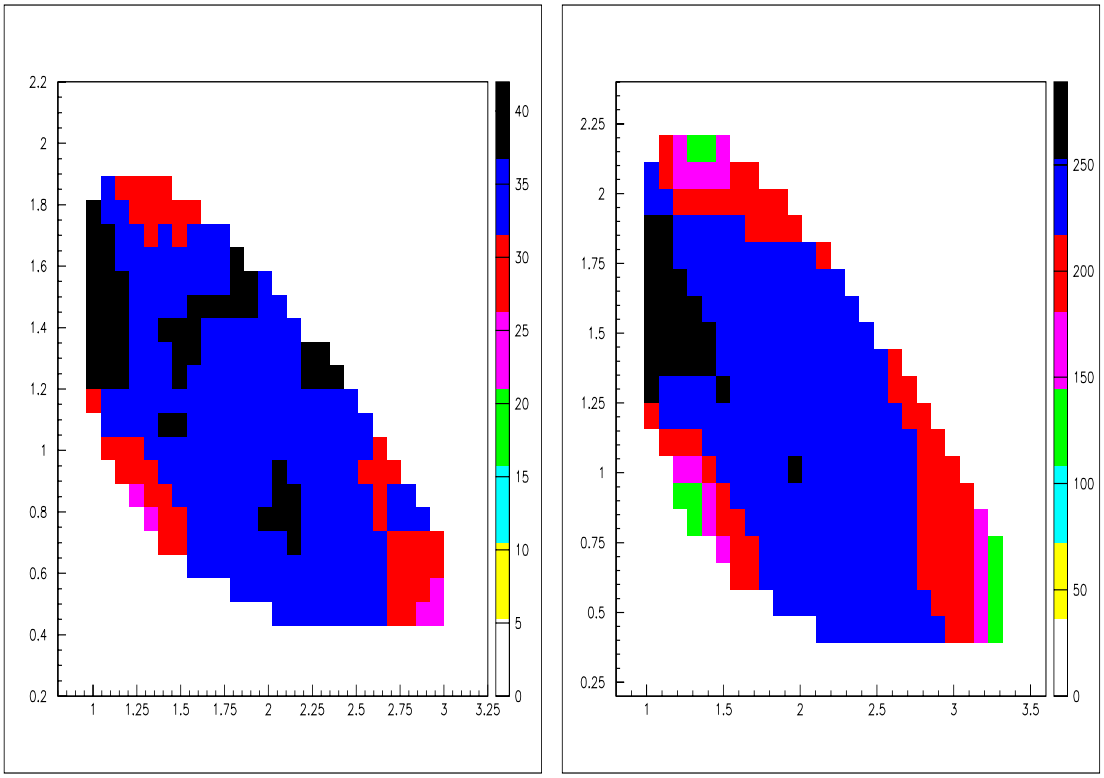

Figure 4.9: D^+ and D_s^+ efficiency plots (The plot is not normalized, in other words the numbers are relative). The higher efficient regions are darker.

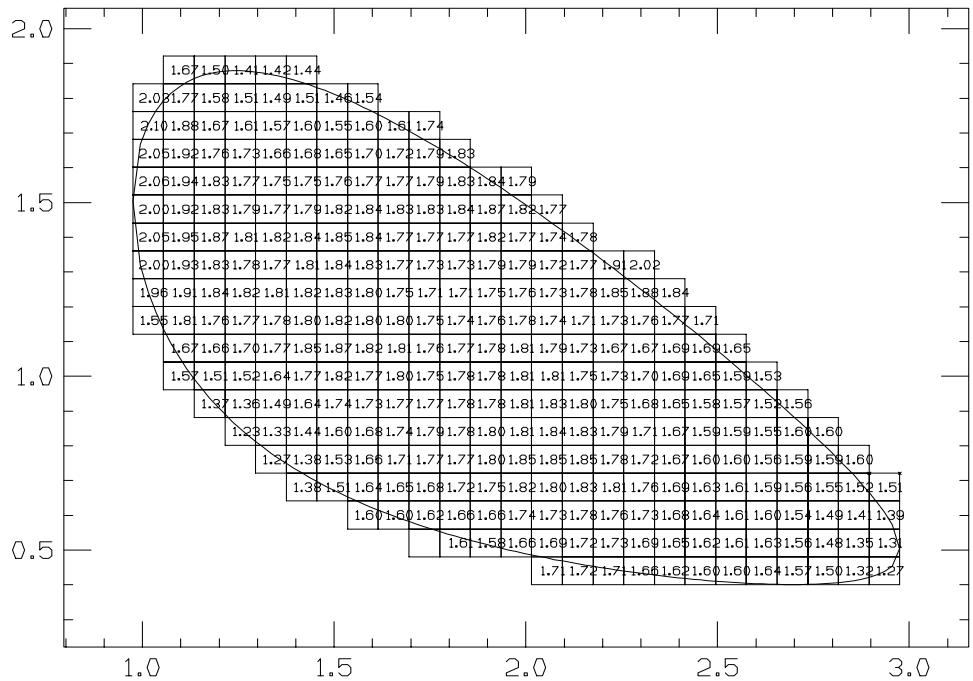

Figure 4.10: The D^+ binned efficiency plot.

4.3 Fit Results

Based on the discussion of the analysis formalism given in section 4.2, the goal is to minimize the the likelihood function given in Equation 4.10 of section 4.2:

$$
\begin{aligned}
w_{sr} &= -2ln\mathcal{L}_{sr} + \chi^2\text{terms} \\
&= -2\sum_{i=1}^{\mathcal{N}_s+\mathcal{N}_{bg}} \ln\left[\epsilon_i\mathcal{F}\frac{\mathcal{A}_{s,i}\mathcal{A}^*_{s,i}}{\mathcal{N}_s} + (1-\mathcal{F})\frac{\mathcal{I}_{bg}}{\mathcal{N}_{bg}}\right] \\
&\quad + \sum_{\lambda,\kappa}(\beta_\lambda - \beta_\lambda^{(sb)})E^{-1}_{\lambda\kappa}(\beta_\kappa - \beta_\kappa^{(sb)}) + \left[\frac{\mathcal{F}-\mathcal{F}_0}{\sigma\mathcal{F}_0}\right]^2
\end{aligned}
\tag{4.14}
$$

The minimization of the likelihood function is done using the CERN minimization utility MINUIT[5].

A joint fit to the sidebands are performed first. The sideband fits are then used to construct the background likelihood penalty term in Equation 4.15. A number of

possible resonant candidates are selected and used in the fit for the signal region. The selected criterion as to which fit to select is four fold.

1. Visual inspection of Dalitz plot created by mini Monte Carlo[7] simulation where the fit amplitude is simulated using the rejection method.

2. Close visual inspection of overlays of predicted and data Dalitz projections. By investigating the overlays, local mismatches between the model and data can be investigated.

3. Gauging the goodness of the fit by measuring χ^2 for each fit. To obtain a χ^2, the Dalitz plot is subdivided into square bins and the χ^2 is calculated for each bin.

4. Occam's Razor: the simplest of competing theories is preferred to the more complex

The fit results for D^+ and D_s^+ are describe in the following sections.

4.3.1 Fit Results for $D^+ \to K^+K^-\pi^+$

We begin by summarizing our analysis and then argue our choice for the resonances included in our standard fit.

Analysis cuts and D^+ signal

The fitted mass histogram of the sample that is used for this analysis is shown in Figure 4.11. The mass histogram is divided into the signal and side band regions shown by the vertical lines.

[7]The Mini-Monte Carlo method is described in detail in chapter 6

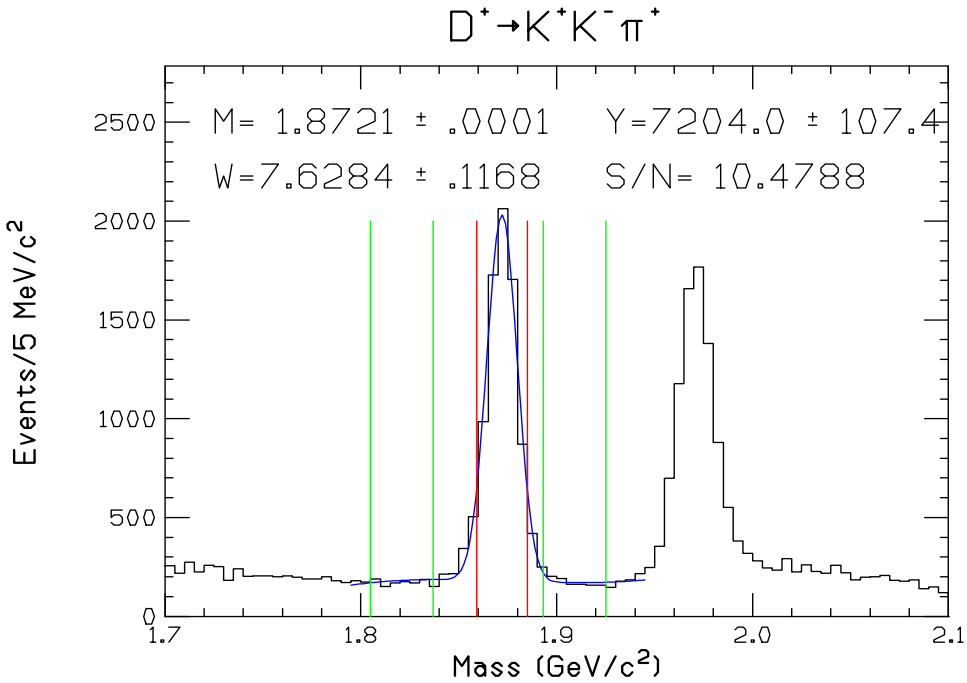

Figure 4.11: The D^+ signal and yield.

The cuts that are used in addition to the skim level cuts in SEZDEE to obtain the D^+ sample are given in Table 4.3.

Resonance Choices

The Dalitz plot for D^+ shown in Figure 4.12 is dominated by the presence of a sharp resonance at around $m^2_{K^+K^-} = 1.040\,(GeV/c^2)^2$, due to the decay chain $D^+ \to \phi\pi^+ \to (K^+K^-)\pi^+$. The ϕ resonance has spin one, a mass of $1.020 MeV/c^2$ and a width of $0.00443 MeV/c^2$ [1]. The band near $m^2_{K^+K^-} \approx 0.8\,(GeV/c^2)^2$ is due to the decay chain $D^+ \to \bar{K}^*(890)^0 \to (K^-\pi^+)\,K^+$. The $K^*(890)^0$ resonance has spin one, a mass of $0.896 MeV/c^2$ and a width of $0.0505 MeV/c^2$. The relative depopulation in the center of both the ϕ and $\bar{K}^*(890)^0$ bands is due to a node in the angular wave function describing the decay of the vector meson resonance to two pseudoscalars. The ϕ node is somewhat populated by what appears to be a broader resonance. We show that

Table 4.3: D^+ Cuts

Cut Name	Cut Value
l/σ	> 9
ΔW_k	> 3
Kaon not Proton	> -6
Primary ISO	< 0.001
secondary ISO	< 0.01
# of σ OOT	> 3

a possible candidate for this resonance is $f_0(980)$ which has a mass of $0.980 MeV/c^2$ and a width of about 50 MeV/c^2. This resonance was not included in the previous analysis [2]. However, we will present clear evidence that including this resonance improves the projections overlays significantly.

Figure 4.13 compares the $K^-\pi^+$ projections with the E687 resonance choice, and with the $f_0(980)$ and $f_J(1710)$ included. The fit without the $f_0(980)$ overshoots the data significantly at the high end of the $K^-\pi^+$ projection. Figure 4.14 compares the $K^+\pi^+$ projections with the E687 resonance choice, and with the $f_0(980)$ and $f_J(1710)$ included. Inclusion of the $f_0(980)$ dramatically improves the agreement between the model and observed projections in the region near 0.9 $(\mathrm{GeV/c^2})^2$ and 1.5 $(\mathrm{GeV/c^2})^2$.

Generally, in the absence of quantum mechanical interferences, one would expect symmetric ϕ and $K^*(890)^0$ lobes. The asymmetry in the $K^*(890)^0$ lobes is seen as an indication of interference with the broader scalar resonance. The $E687$ group [2] used $K^*(1430)$ as this broad resonance. In this analysis, we have shown that besides this resonance, other established resonances can be included in this set such as $f_J(1710)$ which dramatically influences the fraction of $K^*(1430)$ while leaving the

phases and amplitudes of landmark resonances relatively unchanged. In particular one can get significant interference between these scalar resonances which changes their fit fractions dramatically.

Comparison of the fit results with and without $f_J(1710)$ added to the mix is shown in Table 4.4, and the corresponding overlays are shown in Figure 4.15, 4.16, and 4.17. Table 4.4 suggests the ironic conclusion that the $f_J(1710)$ can have a huge effect on other scalar resonances while exhibiting a remarkably small fit fraction of less than 3% for itself. We believe that this is essentially an illustration of quantum mechanical interference between the broad scalar resonances. Although the $f_J(1710)$ intensity is small, its amplitude which is proportional to the square root of this intensity is not negligible. According Table 4.4 the modified amplitude for a resonance such as the $f_0(980)$ is indeed consistent with the usual triangle inequality: $|a_{f0} - a_{fJ}| < |a'_{f0}| < |a'_{f0} + a_{fJ}|$. It is somewhat surprising this interference is nearly complete for the case of the $K^*(1430)$. Interference of the $f_J(1710)$ with the narrow vector amplitudes is evidently much smaller.

The prediction and data overlays shown in Figure 4.14, indicates that all of our fits produce a big mismatch in the wrong sign projection in the region of 0.5 to 1.0 GeV/c^2. The data has a clear maximum near 0.7 GeV/c^2 which none of our models is unable to reproduce with any resonances from the set $\bar{K}^*(890)^0$, $\phi(1020)$, $K^*(1430)$, $f_0(980)$ and $f_J(1710)$. Other resonances which were added to the amplitude but dropped later because they did not substantially improve fit quality of overlays are $a_0(1450)$, $f_0(1500)$, and $a_2(1320)$, these are further discussed in the systematics, in chapter 7. The bin by bin contribution to the χ^2 for the D^+ fit corresponding to the projections of Figure 4.16 is shown in Figure 4.18.

One possibility is that we just have too crude a model for the strong interaction dynamics which govern charm decay. Another possibility is that new (unestablished)

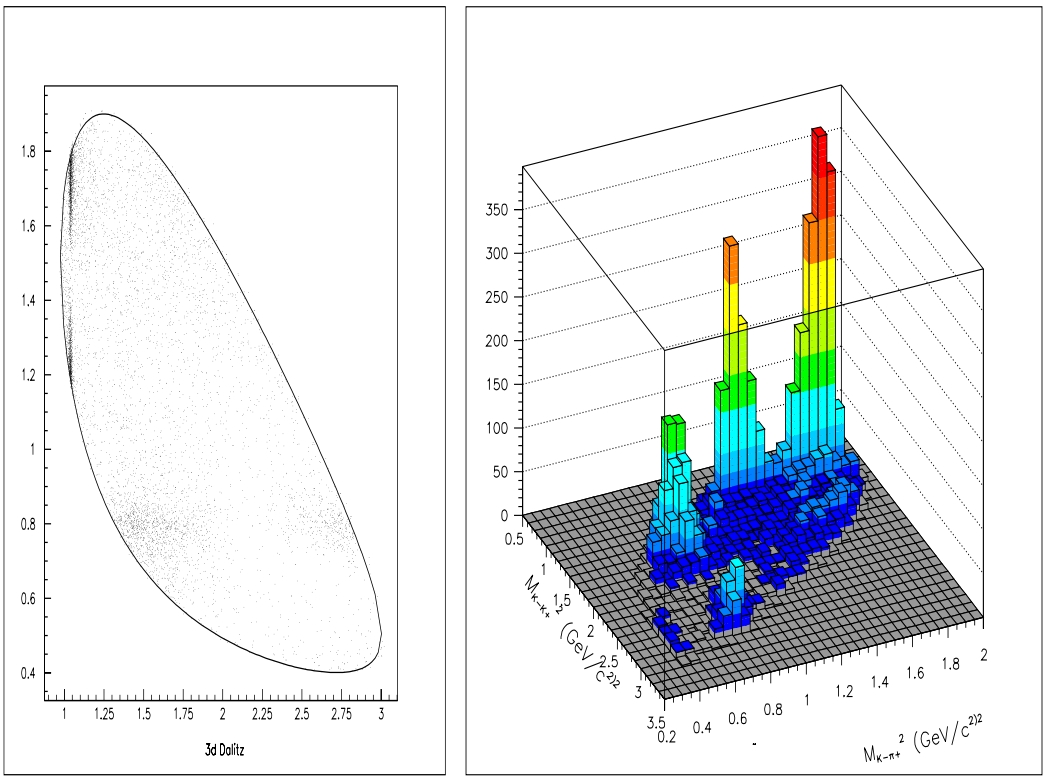

Figure 4.12: Dalitz scatter plot and the corresponding 3-D plot of $D^+ \to K^+K^-\pi^+$.

resonances might be present. For example in $E687$ [18] an $S(1500)$ resonance was required to fit the 3π Dalitz plot. Our data, which is perhaps the best in the world is still insufficient to disentangle the underlying dynamics at this point.

The fit results and errors in Table 4.4 are those obtained directly from the fit and include statistical errors only. In the next two Chapters we will investigate possible fit biases, underestimates of the statistical errors, and evaluation of systematic errors. The final values with our best estimate of the true error appears in the Summary Chapter.

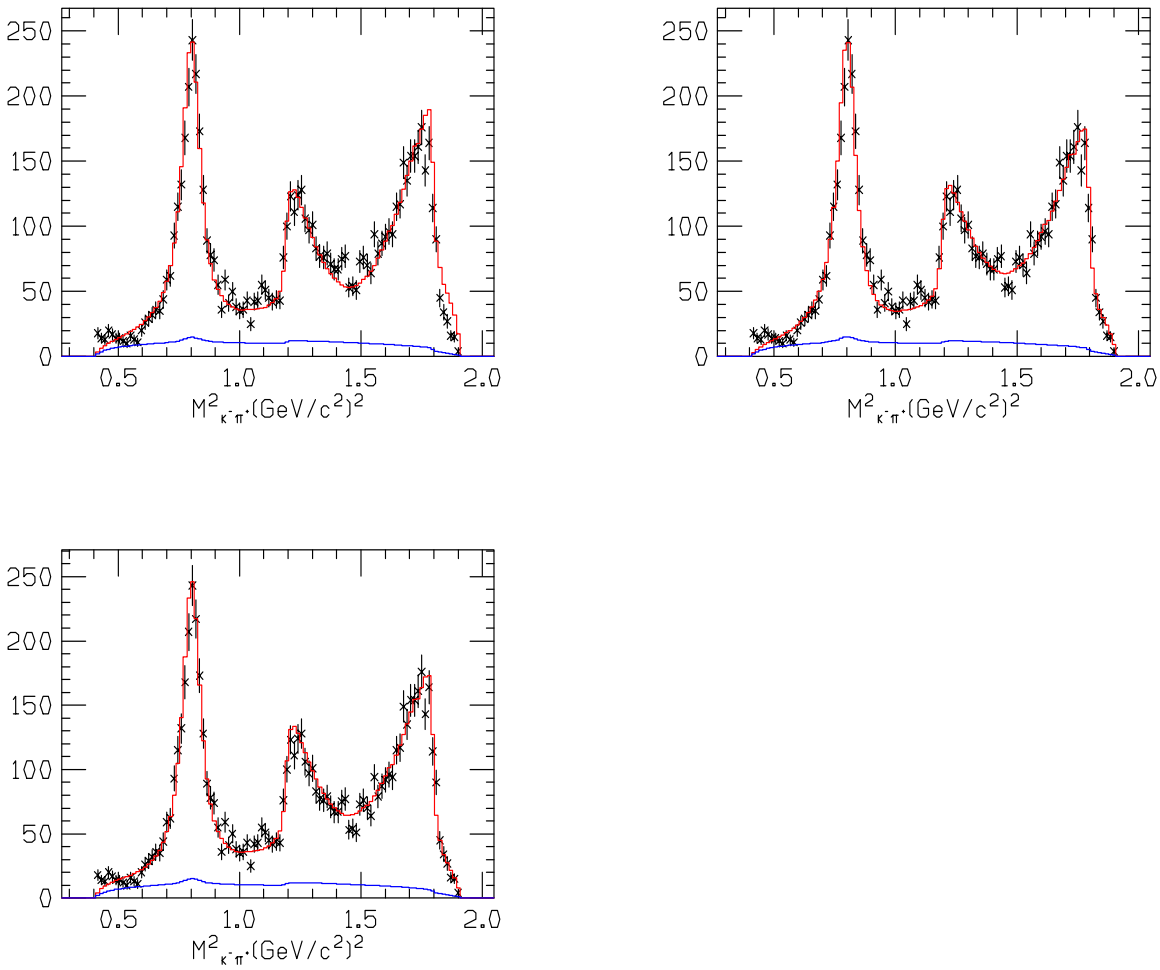

Figure 4.13: The $K^-\pi^+$ projections of D^+. The upper left projection includes $K^*(890)^0$, ϕ, and $K^*(1430)$ resonances. The upper right plot also includes $f_0(980)$. The lower plot includes $f_J(1710)$ as well.

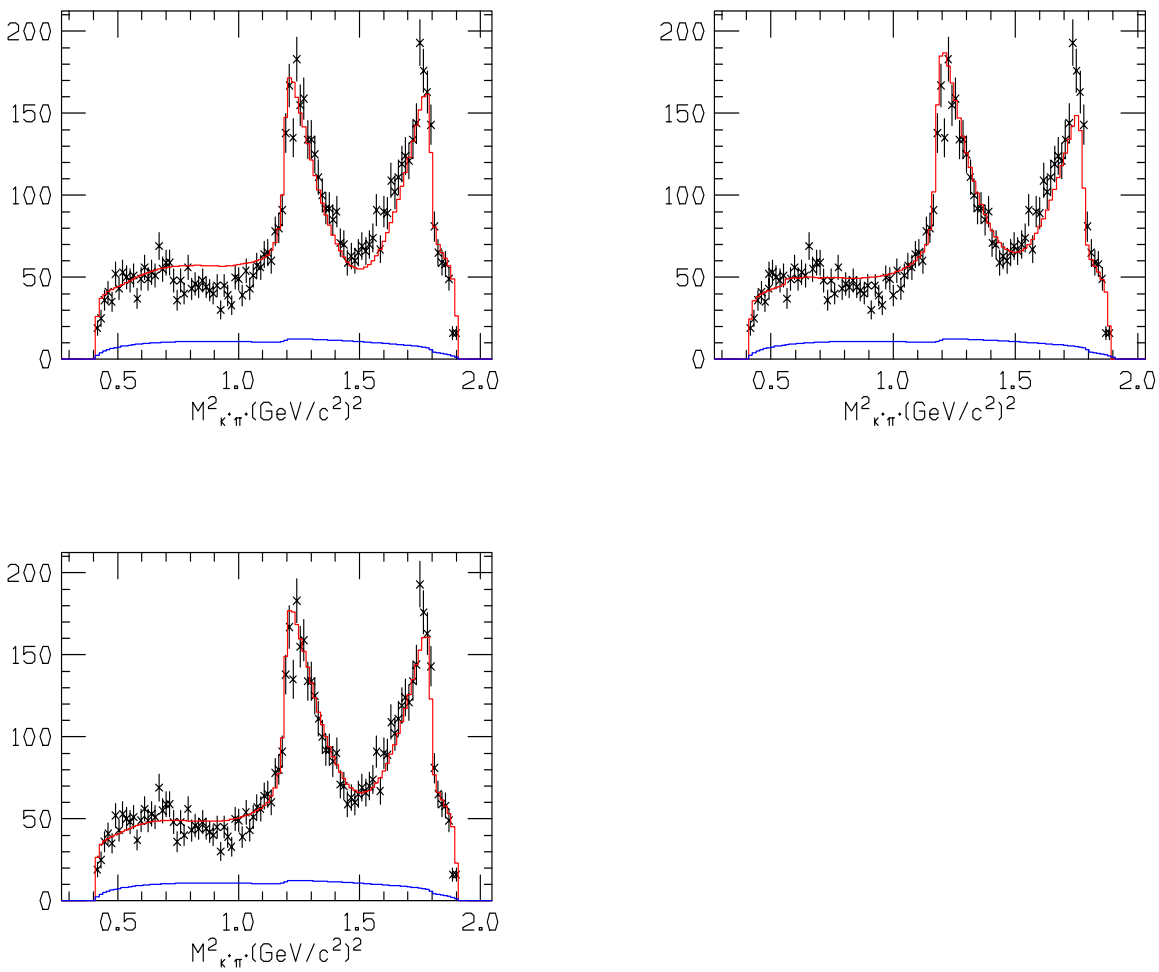

Figure 4.14: The $K^+\pi^+$ projections of D^+. The upper left projection includes $K^*(890)^0$, ϕ, and $K^*(1430)$ resonances. The upper right plot also includes $f_0(980)$. The lower plot includes $f_J(1710)$ as well.

Table 4.4: D^+ Fit Results

Parameter	Fitted Value $\pm\sigma_{stat}$ Without $f_J(1710)$	With $f_J(1710)$
$a_{\bar{K}^*(890)^0K^+}$	1.0 (fixed)	1.0 (fixed)
$a_{f_0(980)\pi^+}$	1.724 ± 0.0140	1.923 ± 0.061
$a_{\phi\pi^+}$	1.113 ± 0.014	1.128 ± 0.014
$a_{K^*(1430)K^+}$	2.313 ± 0.064	2.938 ± 0.087
$a_{f_J(1710)\pi^+}$		0.616 ± 0.048
$\delta_{\bar{K}^*(890)^0K^+}$	0° (fixed)	0° (fixed)
$\delta_{f_0(980)\pi^+}$	-78.3 ± 1.9^o	-100.3 ± 1.8^o
$\delta_{\phi\pi^+}$	117.9 ± 2.2^o	119.2 ± 2.7^o
$\delta_{K^*(1430)K^+}$	95.3 ± 2.1^o	109.4 ± 1.8^o
$\delta_{f_J(1710)\pi^+}$		-59.6 ± 4.0^o
$f_{\bar{K}^*(890)^0K^+}$	0.2838 ± 0.0077	0.285 ± 0.013
$f_{f_0(980)\pi^+}$	0.2409 ± 0.0013	0.301 ± 0.021
$f_{\phi\pi^+}$	0.2730 ± 0.0089	0.281 ± 0.015
$f_{K^*(1430)K^+}$	0.2180 ± 0.0095	0.353 ± 0.024
$f_{f_J(1710)\pi^+}$		0.024 ± 0.005

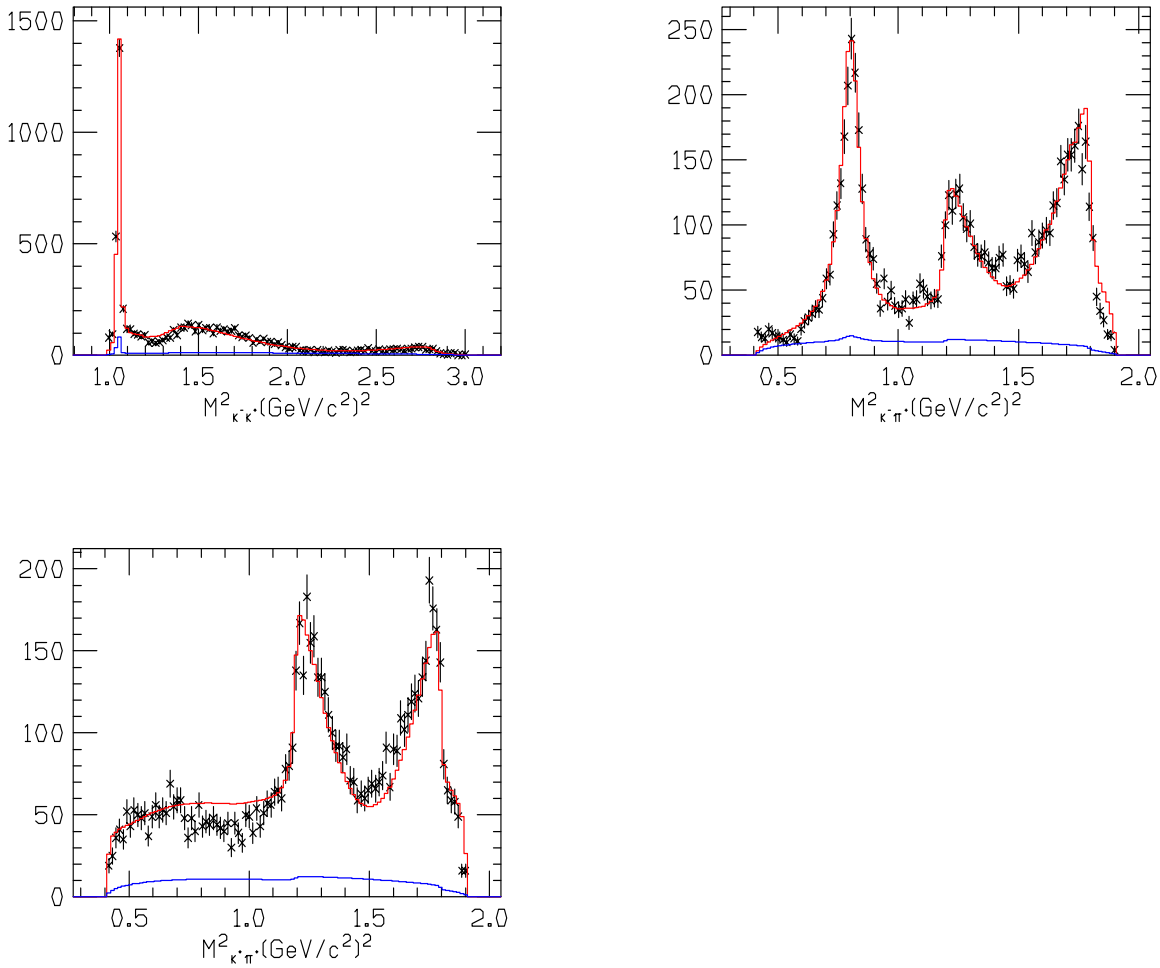

Figure 4.15: The D^+ projections with K^*, ϕ, and $K^*(1430)$ contributions only. Points with error bars are data, red is the signal.

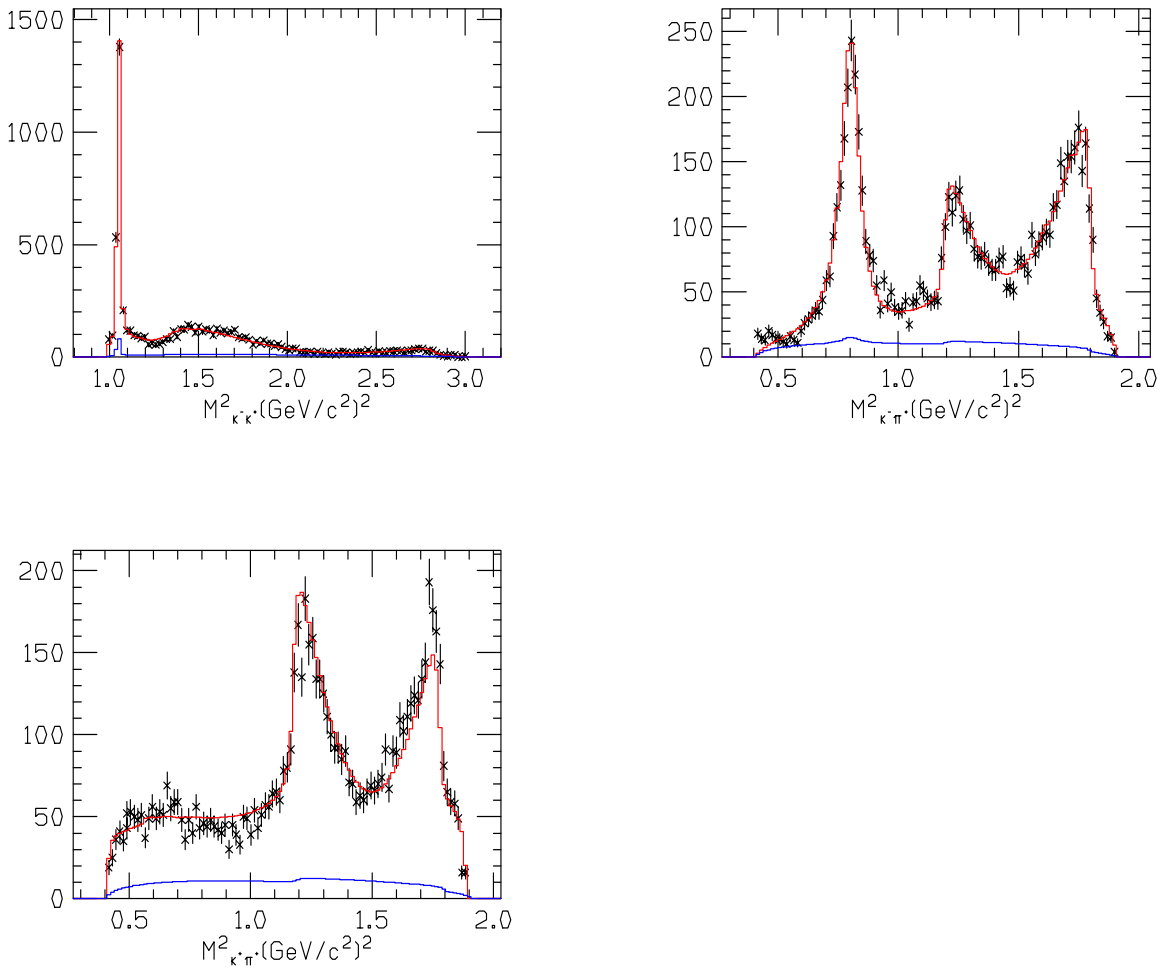

Figure 4.16: The D^+ projections with with K^*, ϕ, $K^*(1430)$, and $f_0(980)$ contributions. Points with error bars are data, red is the signal prediction and blue is background prediction.

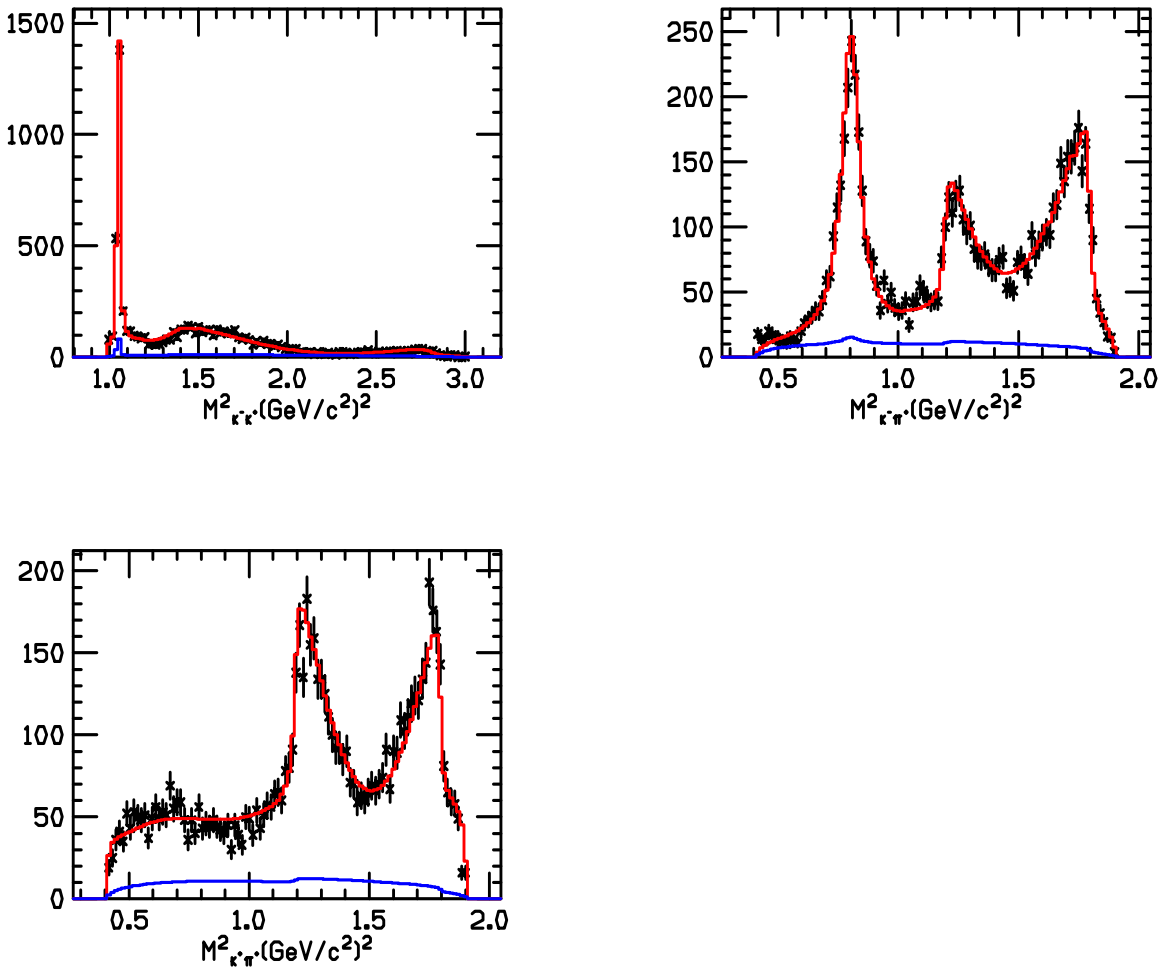

Figure 4.17: The D^+ projections with K^*, ϕ, $K^*(1430)$, $f_0(980)$, and $f_J(1710)$ added. Points with error bars are data, red is the signal.

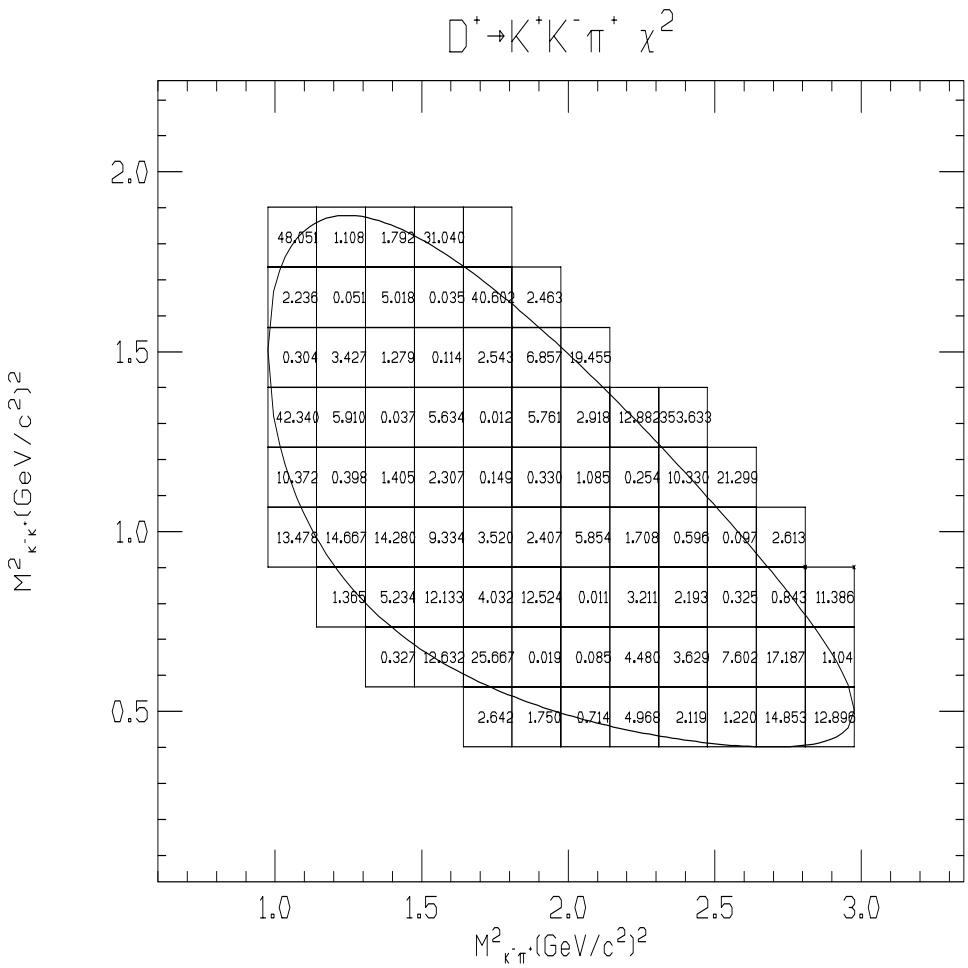

Figure 4.18: Bin by bin contribution to the χ^2 for the D^+

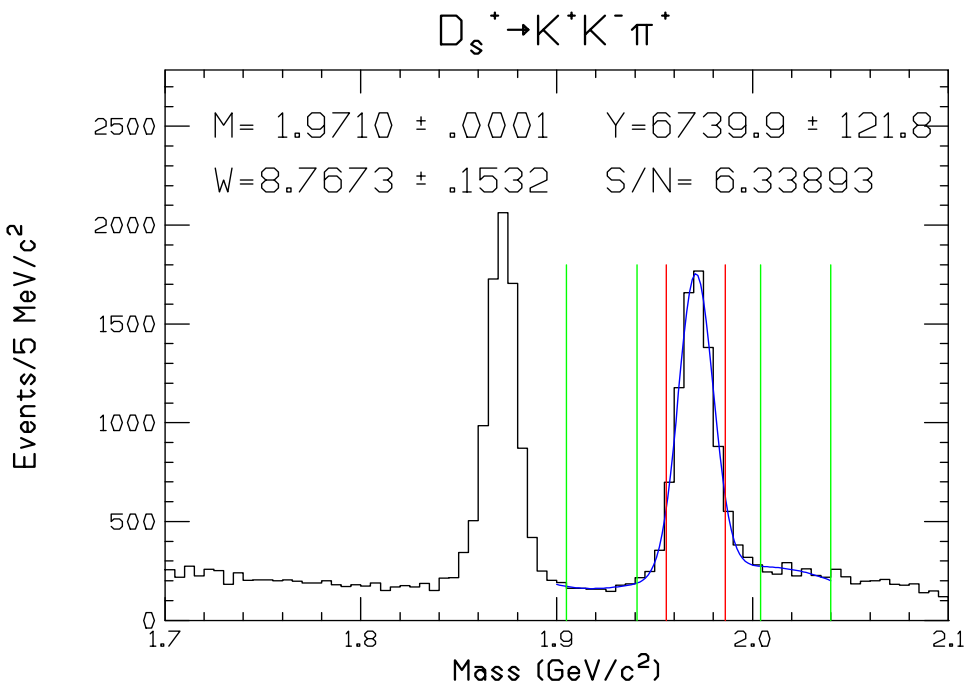

Figure 4.19: The D_s^+ signal and yield.

4.3.2 Fit Results for $D_s^+ \to K^+K^-\pi^+$

The Dalitz plot for D_s^+ is shown in Figure 4.20. In D_s^+ Dalitz plot both the ϕ and $K^*(890)^0$ lobes are present. What is different in this decay mode, is the absence of strong asymmetries in $K^*(890)^0$ lobes, which is an indication of smaller interference with $K^*(1430)$. It is shown that in addition to the resonances in D^+ Dalitz plot, a $a_0(980)$ resonance through the decay chain, $D_s^+ \to a_0(980) \to (K^-\pi^+)\,K^+$ is also seen.

The fitted mass histogram of the sample that is used for this analysis is shown in Figure 4.19. The mass histogram is divided into the signal and side band regions shown by the vertical lines.

The cuts that are used in addition to the skim level cuts in SEZDEE to obtain the D^+ sample are given in Table 4.5.

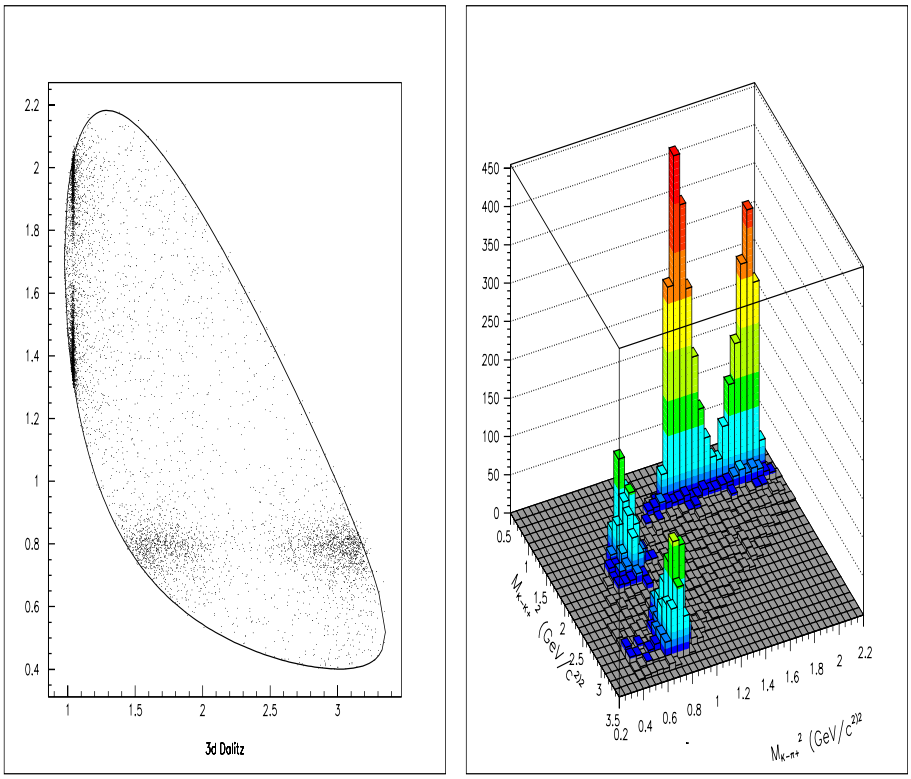

Figure 4.20: Dalitz scatter plot and the corresponding 3-D plot of $D_s^+ \rightarrow K^+K^-\pi^+$.

Table 4.5: D_s^+ Cuts

Cut Name	Cut Value
l/σ	> 9
ΔW_k	> 5
Kaon not Proton	> -6
Primary ISO	< 0.001
secondary ISO	< 0.01
# of σ OOT	> 3

The total amplitude for this fit consists of amplitudes for $\bar{K}^*(890)^0$, $\phi(1020)$, $K^*(1430)$, $f_0(980)$ and $f_J(1710)$ resonances. The fit results are shown in Figure 4.6. The $\delta_{K^*(1430)K^+}$ phase is $\approx 120^o$ and the fit fraction is $\approx 5\%$ that is an order of magnitude smaller than the corresponding amplitude for D^+. Hence the large asymmetries in $\bar{K}^*(890)^0$ lobes are absent for this decay mode. There is strong presence of $\bar{K}^*(890)^0$ and $\phi(1020)$ resonances in this mode, in contrast to D^+ where each intermediate resonance contribution for the decay amplitude is comparable.

The fit results and errors in Table 4.6 are those obtained directly from the fit and include statistical errors only. In the next two Chapters we will investigate possible fit biases, underestimates of the statistical errors, and evaluation of systematic errors. The final values with our best estimate of the true error appears in the Summary Chapter.

The prediction and data overlays are shown in Figure 4.21.

Table 4.6: D_s^+ Fit Results

Parameter	Fitted Value $\pm\sigma_{stat}$
$a_{\bar{K}^*(890)^0K^+}$	1.0 (fixed)
$a_{f_0(980)\pi^+}$	1.199 ± 0.040
$a_{\phi\pi^+}$	1.001 ± 0.013
$a_{K^*(1430)K^+}$	0.851 ± 0.053
$a_{f_J(1710)\pi^+}$	0.381 ± 0.030
$\delta_{\bar{K}^*(890)^0K^+}$	0° (fixed)
$\delta_{f_0(980)\pi^+}$	129.7 ± 3.5^o
$\delta_{\phi\pi^+}$	147.4 ± 3.7^o
$\delta_{K^*(1430)K^+}$	128.7 ± 6.8^o
$\delta_{f_J(1710)\pi^+}$	82.8 ± 7.6^o
$f_{\bar{K}^*(890)^0K^+}$	0.5134 ± 0.0153
$f_{f_0(980)\pi^+}$	0.1543 ± 0.0108
$f_{\phi\pi^+}$	0.3844 ± 0.0134
$f_{K^*(1430)K^+}$	0.0624 ± 0.0075
$f_{f_J(1710)K^+}$	0.0198 ± 0.0033

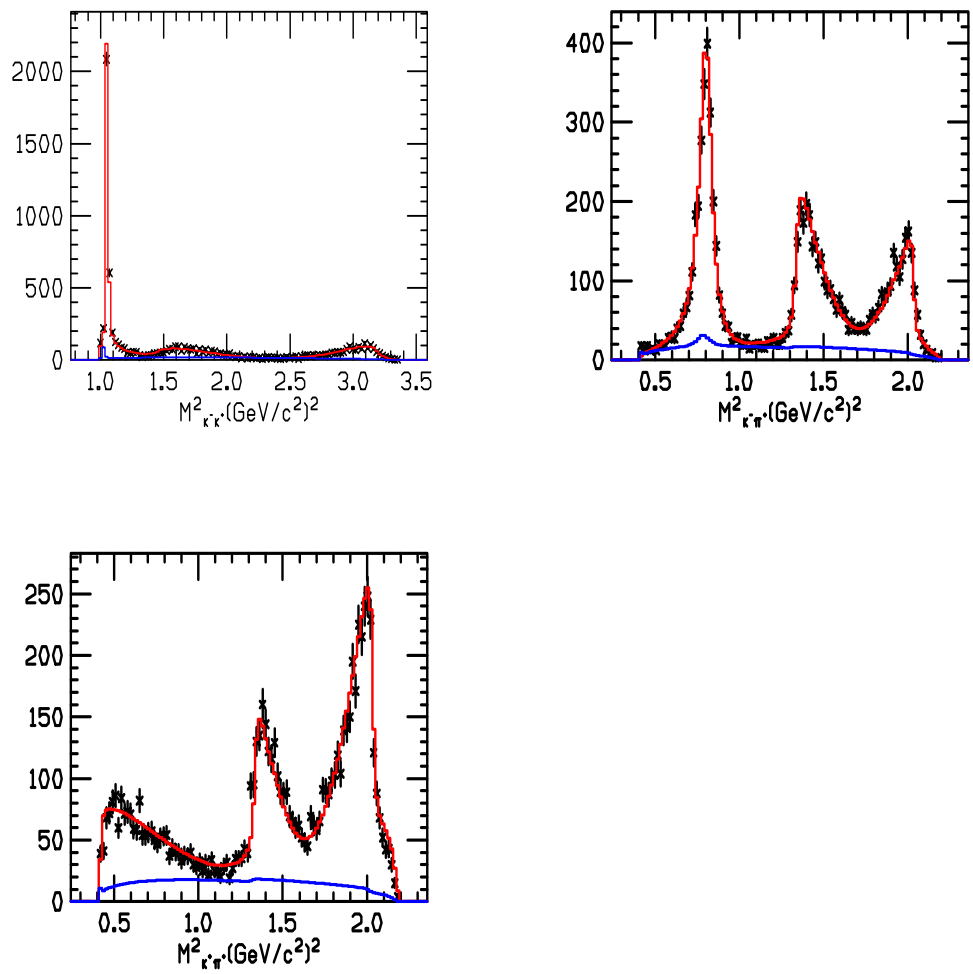

Figure 4.21: The D_s^+ projections. Points with error bars are data, red is the signal prediction and blue is background prediction.

Chapter 5

The $D^0 \to K_S K^+ K^-$ Dalitz Analysis

In this chapter the Dalitz analysis of $D^0 \to K_s K^+ K^-$ is discussed. First the cuts for obtaining a very clean signal is presented. The $D^{*\pm}$ tagging technique is described which is used to both obtain a nearly background free signal, and to determine the strangeness of the K_s, which is needed for this Dalitz analysis. Next the fit results and projection overlays are shown. The intermediate resonances that are found to contribute to this decay mode are $a_0^{\pm}(980)$, $f_0(980)$, and $\phi(1020)$. There is some evidence of quantum mechanical interference between ϕ and $f_0(980)$ in ϕ region. With a broad ϕ cut approximately, $63 \pm 3\%$ of the events are found to be ϕ which is an odd eigenstate of CP symmetry and $37 \pm 2\%$ are $f_0(980)$ (or possibly $a_0^{+}(980)$) which is an even eigenstate state of CP symmetry. With a narrower cut, the $\pi^+ f_o(980)$ contribution drops significantly. This study bears on the suitability of using the $D^0 \to K_s^o \phi$ decay mode to compare the lifetime of this CP odd eigenstate to that for $D^0 \to K^+ K^-$ which is a CP even eigenstate. The fact that a large fraction of $D \to K_s^o K^+ K^-$ events where the dikaon is in the ϕ region are actually CP even states from $K_s^o f_o(970)$ decay can complicate the use of this mode as a CP even state for this purpose.

5.1 The $D^0 \to K_s K^+ K^-$ Cuts and Signal

The signal to noise ratio is improved by almost six fold by requiring that D^0 is formed through a $D^{*\pm}$ decay, see Figure 5.1. Besides allowing us to significantly reduce backgrounds, the D^* tag allows us to tag the strangeness of the neutral kaon which emerges as a $\bar{K}^0$ since the $D^0 \to K_s^0 K^- K^+$, given its relatively large branching fraction, is much more likely to be a Cabibbo favored than doubly Cabibbo suppressed decay. The $\Delta S = \Delta C$ rule implies that Cabibbo favored charm decay final state has $S = 1$ which implies that the K_s^o originates from a $\bar{K}_o$. Hence the $K_s^0 K^- K^+$ final state is either $\bar{K}^0 K^- K^+$ if it is tagged in association with a π^+ from $D^{*0} \to D^0 \pi^+$ or $K^0 K^- K^+$ if it is tagged in association with a π^- in $\bar{D}^{*0} \to \bar{D}^0 \pi^-$. This information is very important in studying the $D^0 \to K_s^0 K^- K^+$ Dalitz plot since, for example, one can only form dikaon resonances (which must be zero strangeness) such as the $a_o^+(980)$ of the form $\bar{K}^0 K^+$ or $K^0 K^-$ The D^{*+} candidate is reconstructed by combining the four momentum of the D^0 and a pion from the primary vertex. The D^* cut variable is then defined as:

$$|\Delta(M_{D^*} - M_{D^0})| = \left|(M_{D^0\pi^+} - M_{D^0}) - \left(M_{D^*}^{pdg} - M_{D^0}^{pdg}\right)\right| \tag{5.1}$$

Where $M_{D^*}^{pdg}$ and $M_{D^0}^{pdg}$ are the D^0 and D^* masses obtained from the PDG[1]. For this decay mode, we use a nominal D^* mass cut of $|\Delta(M_{D^*} - M_{D^0})| \leq 2MeV$.[1] Figure 5.1 shows the mass histograms with and without the D^* cut. A kaonicity cut of $\Delta W_K > 3$ for dikaon is applied to further clean up the signal, as it excludes events with tracks that are pions. The detachment cut ℓ/σ isn't as effective for this decay

[1]We put the cut on the mass difference rather than the D^{*+} mass since it is typically better resolved by a factor of 5. This is because the smearing of the D^0 mass essentially "subtracts out" in the mass difference.

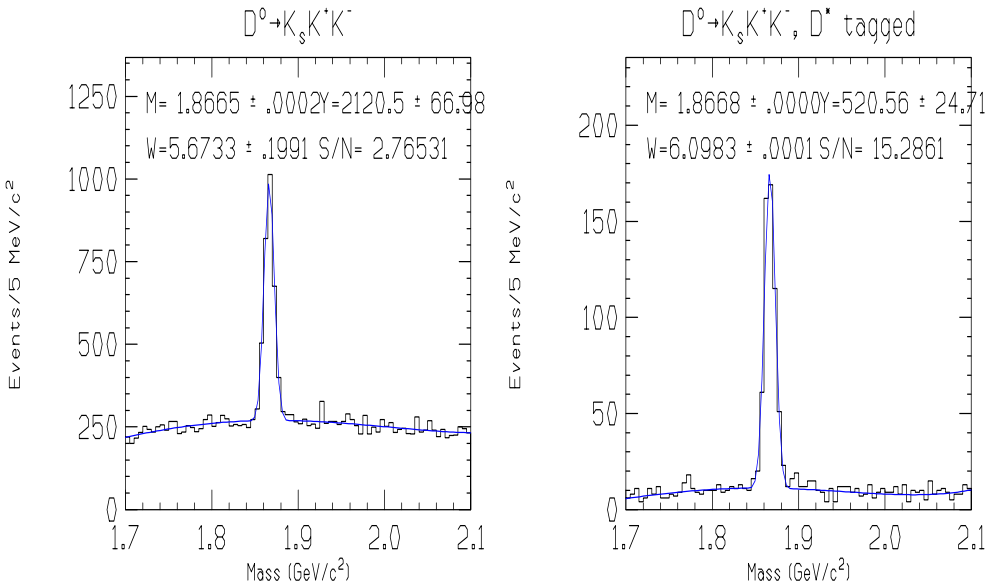

Figure 5.1: The D^0 signal with and without the D_0^* tagging.

mode, because the dikaon system has very small Q value as the sum of the masses is very near the ϕ mass, giving the kaons a small opening angle and thus a poorly formed secondary vertex. Signal properties are shown in Figure 5.1.

The summary of the cuts are shown in Tables 5.2 and 5.3.

Table 5.1: $D^0 \to K_s K^+ K^-$ signal properties

Parameter	D^0, untagged	D^0 tagged
Fitted Yield	2120 ± 67	521 ± 25
Fitted Mass (GeV/c^2)	$1.8665 \pm .0002$	1.8668 ± 0.0000
Width σ $GeV/c^2)$	0.00567 ± 0.00020	$0.0060983 \pm .00000$
Signal Fraction F_0	0.65	0.92

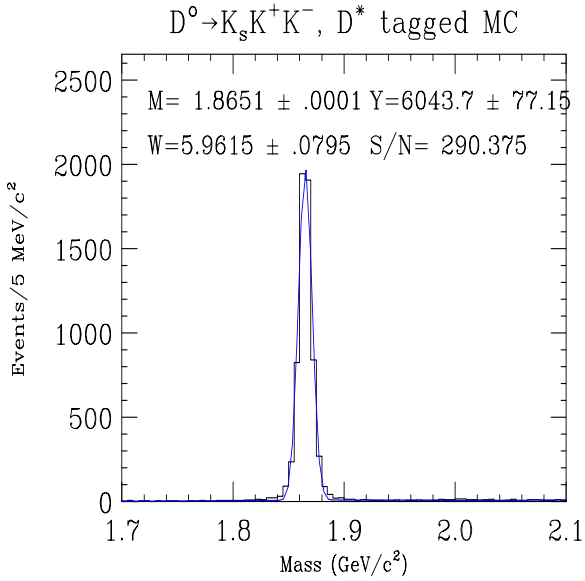

Figure 5.2: The D^0 Monte Carlo sample with D^* tag

Table 5.2: D^* tagged D^0 Cuts

Cut Name	Cut Value
l/σ	> 4
ΔW_k	> 3
$\lvert\Delta(M_{D^*} - M_{D^0})\rvert$	$\leq 2MeV$
secondary ISO	< 0.01
good kshort	$= 2$

Table 5.3: non-tagged D^0 Cuts

Cut Name	Cut Value
l/σ	> 4
ΔW_k	> 2
Kaon not Proton	> -2
Primary ISO	< 0.01
secondary ISO	< 0.001
good kshort	$= 2$

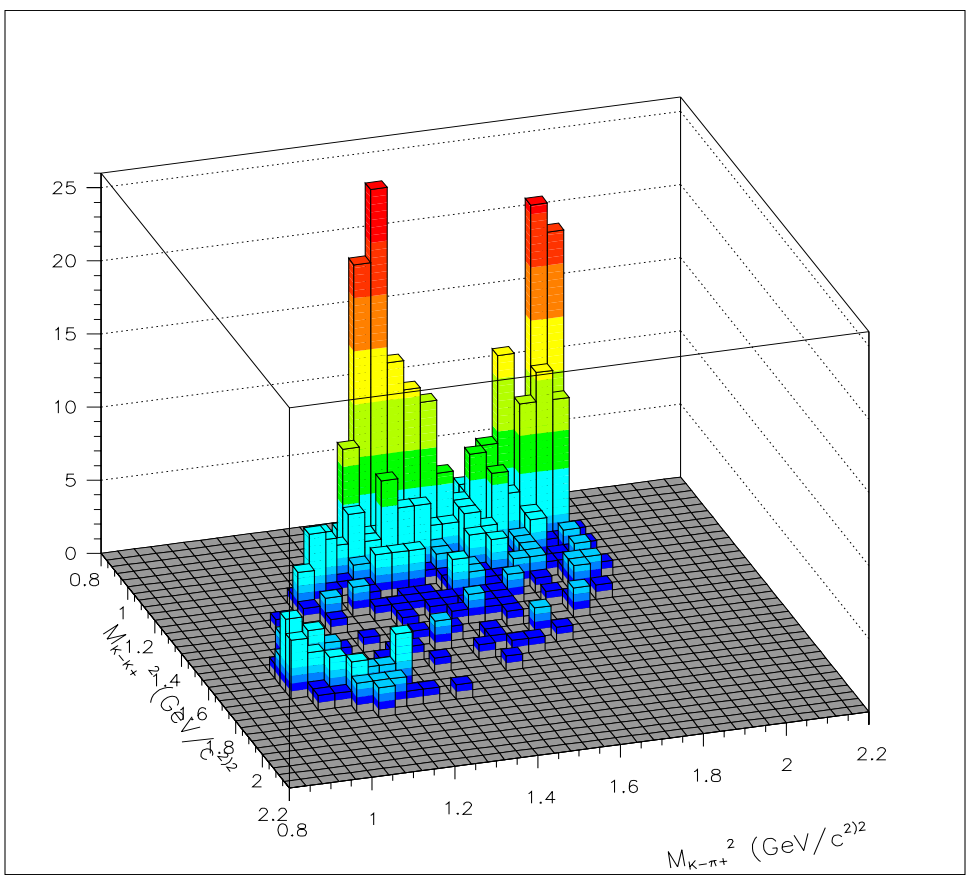

Figure 5.3: Dalitz 3-D plot of $D^0 \to K_s K^+ K^-$.

5.2 The $D^0 \to K_s K^+ K^-$ Dalitz Plot

The Dalitz plot for this mode is shown in Figure 5.3. It is constructed by plotting the invariant mass of the K^+K^- on one axis and $\bar{K}^0K^+$ (or K^0K^-) on another. The strangeness of the neutral kaon is determined by tagging the charm of the D^0 from the D^* decay. The, by now familiar, ϕ lobes have dominated the low K^+K^- mass region. There are some accumulation of events in the ϕ node, which extends further along the K^+K^- axis. We expect, and the data is well fit, by the broad resonance $f_0(980)$. There is also an accumulation of events at the lower $\bar{K}^0K^+$ (or K^0K^-) region which we expect is the $a_0^{\pm}(980)$.

5.3 The $D^0 \to K_s K^+ K^-$ Fit Results

Using the same formalism discussed in Chapter 4, a fit for $D^0 \to K_s K^+ K^-$ Dalitz plot is performed. The total decay amplitude is the coherent superposition of $f_0(980)$, $a_0(980)$ and ϕ amplitudes. The fit results are shown in Table 5.4. The phase shift between $f_0(980)$ and ϕ is -83 ± 7°. This a relatively imaginary phase which indicates a Final State Interaction and maximal interference asymmetry between the two ϕ lobes.

The overlays of the predicted intensity and the data are shown in Figure 5.4.

It is interesting to measure lifetime differences between CP even and CP odd final states. A primary candidate for accessible CP odd decay is $D^0 \to K_s\phi \to K_s K^+ K^-$. It is important to have a pure $K_s\phi$ sample for such an analysis. Dalitz analysis of $D^0 \to K_s K^+ K^-$ can be employed to determine if the ϕ region is free from other decay channels, particularly channels which may be CP even states.

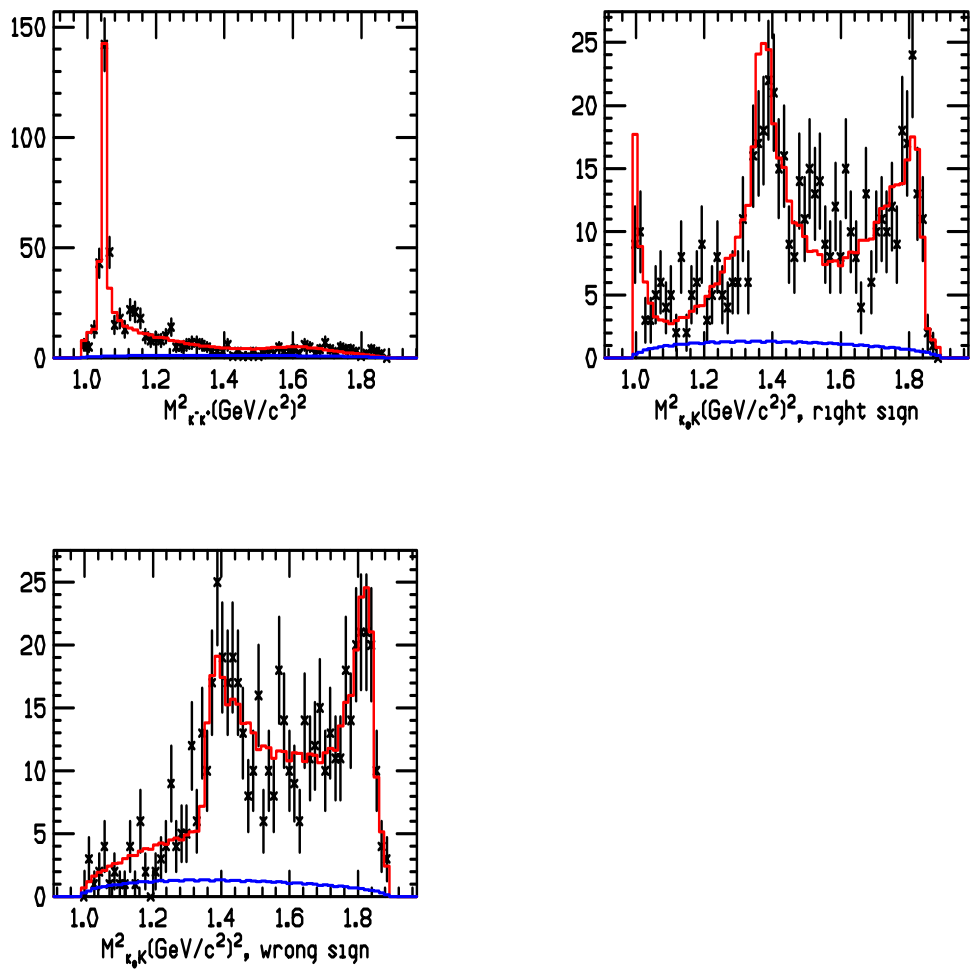

Figure 5.4: The D^0 projections. Points with error bars are data, red is the signal prediction and blue is background prediction.

Table 5.4: D^0 Fit Results

Parameter	Fitted Value $\pm\sigma_{stat}$
$a_{f_0(980)K_s}$	1.0 (fixed)
$a_{a_0^{\pm}(980)K^{\mp}}$	0.25 ± 0.03
$a_{\phi K_s}$	0.58 ± 0.04
$\delta_{f_0(980)K_s}$	0° (fixed)
$\delta_{a_0^{\pm}(980)K^{\mp}}$	138 ± 14°
$\delta_{\phi K_s}$	-83 ± 7°
$f_{f_0(980)K_s}$	0.680 ± 0.044
$f_{a_0^{\pm}(980)K^{\mp}}$	0.140 ± 0.034
$f_{\phi K_s}$	0.476 ± 0.036

5.4 Can a pure $K_s\phi$ CP odd be obtained from $D^0 \to K_sK^+K^-$?

The scatter plot of $D^0 \to K_sK^+K^-$ is shown in Figure 5.5. The "ϕ" region is defined to be within the square. Fraction of events in the "ϕ" region, $f^{\phi}_{\phi rgion}$, due to $K_s\phi$ is:

$$f^{\phi}_{\phi rgion} = \frac{\int\limits_{\phi region} \mathcal{A}^*_{\phi}\mathcal{A}_{\phi}}{\int\limits_{\phi region} \mathcal{A}^*_{total}\mathcal{A}_{total}} \tag{5.2}$$

The values for $f^{\phi}_{\phi rgion}$ as well as $f^{f_0}_{\phi rgion}$ and $f^{a_0^{\pm}}_{\phi rgion}$ are shown in Table 5.5 at two different mass limits. In the limit $M^2_{k^+K^-} < 1.1\,(MeV/c^2)^2$ only $67.2 \pm 3.6\%$ of events in the ϕ region is due to ϕ. The rest of events, $39.0 \pm 3.6\%$, are due to $f_0(980)$. In a tighter mass limit of $1.034 < M^2_{k^+K^-} < 1.042$, the fraction changes to $93.0 \pm 0.9\%$ for ϕ and only $7.7 \pm 1.0\%$ for $f_0(980)$. The ϕ sample is significantly cleaner with this

Table 5.5: fractions in the ϕ region

Resonance	Fraction in the ϕ region $((MeV/c^2)^2)$	
	$M^2_{K^+K^-} < 1.1$	$1.034 < M^2_{K^+K^-} < 1.042$
$f_0(980)$	$39.0 \pm 3.6\%$	$7.7 \pm 1.0\%$
$a_0^+(980)$	$0.3 \pm 0.1\%$	$0.05 \pm 0.01\%$
ϕ	$67.2 \pm 3.1\%$	$93.0 \pm 2.0\%$

cut although some contamination from $f_0(980)$ still remains.

The $K_s\phi$ decay mode is a CP odd state: K_s is a $P = -1$ and if we assume CP conservation $C = -1$ which makes it a CP even state, ϕ is a $C = -1$ and $P = -1$ state which makes it a CP even as well, and considering that $K_s\phi$ has a total angular momentum of one, it is a relative p-wave with parity $(-1)^1$. The $K_s f_0(980)$ is CP even state, because $f_0(980)$ is a $C = +1$ and $P = +1$ state which makes it a CP even state, and because $K_s f_0(980)$ has a total angular momentum of zero, it is a relative s-wave with parity $(-1)^0$.

The two states $K_s\phi$ and $K_s f_0(980)$ interfere in the same region in the Dalitz plot, some CP even state will be present under any ϕ cut, therefore a pure $K_s\phi$ CP odd can't technically be obtained from $D^0 \to K_s K^+ K^-$.

The fit results and errors in Table 5.4 are those obtained directly from the fit and include statistical errors only. In the next two Chapters we will investigate possible fit biases, underestimates of the statistical errors, and evaluation of systematic errors. The final values with our best estimate of the true error appears in the Summary Chapter.

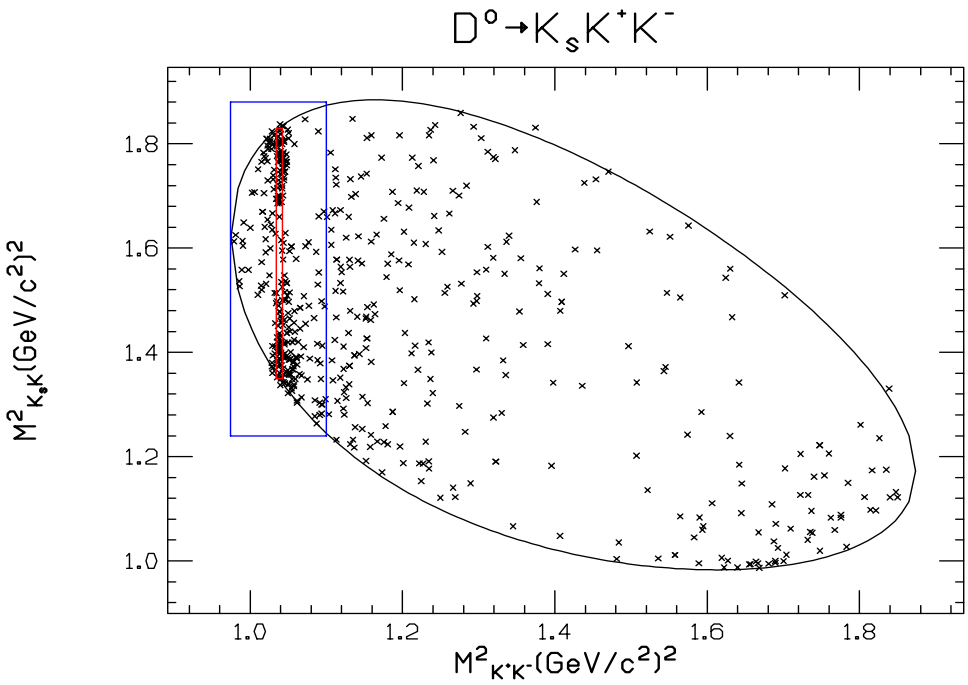

Figure 5.5: The D^0 scatter plot. The ϕ regions $M^2_{K^+K^-} < 1.1$ and $1.034 < M^2_{K^+K^-} < 1.042$ are shown as the inside the rectangles.

Chapter 6

Checking the Fidelity of the Fitting Technique

6.1 Introduction

In this chapter we discuss the Monte Carlo method used to check the fitting technique. Specifically we are trying to understand : (1) if the fitting method is biased and (2) if the returned errors properly represents the spread in the returned fit parameters. Our findings are that the fit is somewhat biased on the 1–3 σ level for some parameters, and the returned statistical errors underestimate the spread in returned fit parameters and should be inflated by factors of from $1.3 \rightarrow 1.8$. For the most part, we understand why this is true. We review several motivations for undertaking such a study.

Although a properly performed linear fit can be shown to produce unbiased fit parameters, to our knowledge there is no such general proof that a continuous likelihood fit is unbiased except in an asymptotic sense. [1] In addition we have taken some shortcuts in our modeling of the Dalitz intensity which are capable of introducing

[1] One can only show that fit biases approach zero in the limit of infinite statistics.

biases in the fit parameters. For example we have neglected experimental resolution of the Dalitz submasses in order to avoid having to parameterize a two dimensional, correlated resolution function. Although it is unlikely that the resolution smearing (which is on the order of $\approx 5\ MeV$) will effect the amplitude and phases for broad resonances, not taking into account smearing creates bias in the parameters for narrow resonances such as the $\phi(1020)$. Similarly, the fitting procedure does not properly model smearing outside of the Dalitz boundary.

The situation with errors is somewhat more complicated. We are computing the errors on fit parameters by looking at the curvature of the $w = -2\ln(\text{Likelihood})$ function about the likelihood minimum. In the case of a linear χ^2-fit, one can show that (1) the log-likelihood function is purely parabolic and (2) that the fit parameters will be Gaussian distributed about the true fit value with an Gaussian width equal to the error deduced from the curvature. These conclusions in general are not precisely true for the sort of continuous likelihood fit being performed here.

In addition, there are additional sources of statistical fluctuation present in these fits which are not present in the traditional continuous fit. One important example are statistical fluctuations on the Monte Carlo sample used to get the efficiency correction. Another example is statistical fluctuations on the sideband background sample used for the background parameterization.

We employ what we will call a *mini-Monte Carlo* technique to study fit biases and error inflation. The basic idea is to generate a large number of simulated data sets (*ensembles*)with a known Dalitz intensity.[2] The principle analysis technique will be

[2] We use the word mini-Monte Carlo since in the interests of CPU time, we do not do a complete simulation of detector response at *ie* the hit level, but rather parameterize features such as the acceptance and resolution for both the signal and background. This method allows us to generate many, many versions of a full FOCUS data set in a moderate (say overnight) time scale.

to study the *pull* distribution where the pull is the difference between a given returned fit parameter and the input fit parameter divided by the returned fit error.

6.2 Getting the parameter pulls

6.2.1 The mini-Monte Carlo Technique

Each simulated event is processed through three stages. At the first stage the four momenta for D^+ and its daughters K^+, K^- and π^+ are drawn. To do so, the D^+ mass, M_{D^+}, is drawn by smearing the nominal D^+ mass as follow:

$$M_{D^+} = M_{D^+_{nominal}} + \sigma_{D^+} \mathcal{G} \tag{6.1}$$

where σ_{D^+} is the experimental width of the D^+ and $\mathcal{G}$ is independent and Gaussian distributed random number with mean 0 and $\sigma = 1$ and is obtained using the following algorithm [1]:

$$\mathcal{G} = \cos(2\pi\Re_1)\sqrt{-2\ln\Re_2} \tag{6.2}$$

where $\Re_1$ and $\Re_2$ are uniform random numbers on the interval $(0, 1)$. Then the four momenta of the the daughters, K^+, K^- and π^+, are assigned using a program to simulate LIPS (Lorenz Invariant Phase Space).

In addition to smearing the mass of the D, we simulate smearing of the submasses. This is done under the assumption that the mass smearing is proportional to the *exothermicity* Q of the two body submass. For example, for the KK submass in the D^+ and D_s^+ Dalitz plot, we would simulate the reconstruction via $M(K^+K^-)_{\text{meas}} = M(K^+K^-)_{\text{true}} + \mathcal{G} \times \sigma_o \times (M(K^+K^-)_{\text{true}} - 2M_K)$ where σ_o is $0.00753\, MeV/c^2$ is based on the observed mass resolution of the D^+ peak.[3]

[3]This form assumes that the mass resolution is primarily due to resolution on the momentum rather than decay angle.

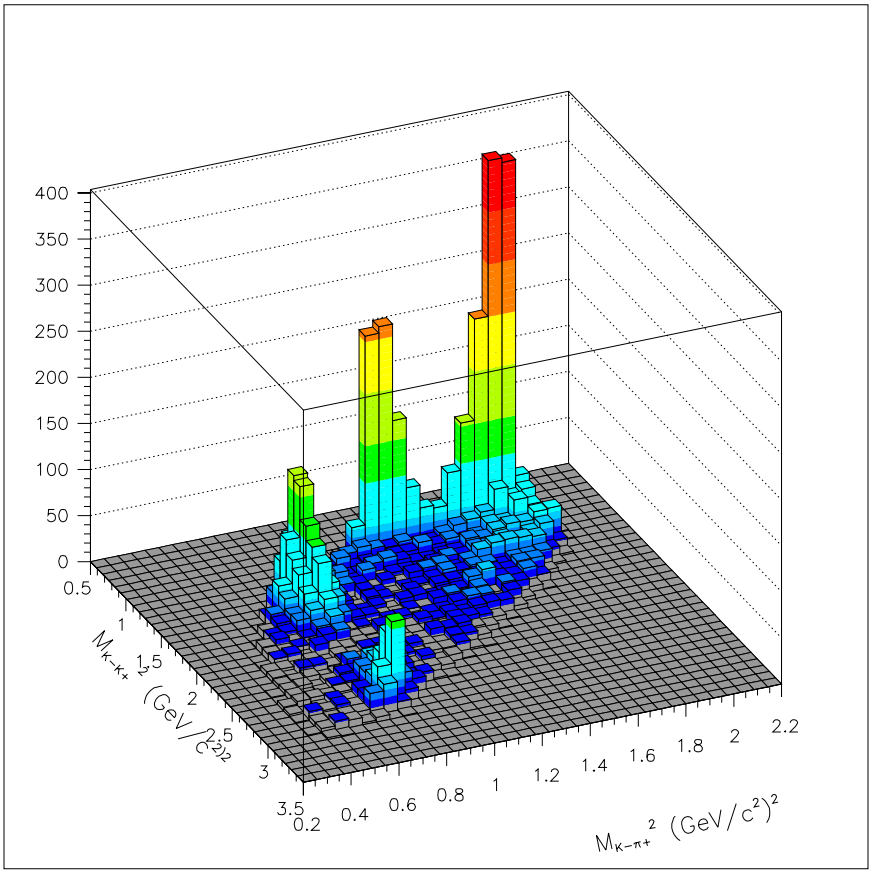

Figure 6.1: The signal region mini Monte Carlo simulation of $D^+ \to K^+K^-\pi^+$.

At the next stage, the population in the Dalitz plot for both the signal and side band regions in each MC sample is simulated. The idea is to obtain random deviates drawn from the intensity function. The rejection method is used for this purpose [4] The simulation of the signal region is done by rejecting on the decay matrix element in Eq. 4.10, where the fit results to data are used as the input parameters a_i and δ_i. The background in the signal region is simulated similarly, as well as the sideband regions where the fit results from the fit to the high and low side band regions in data are used as the input parameters and the rejection method is performed with the background parameterization shown in equation 4.10. The simulated signal and side band Dalitz region lego plots are shown in figures 6.1 and 6.2.

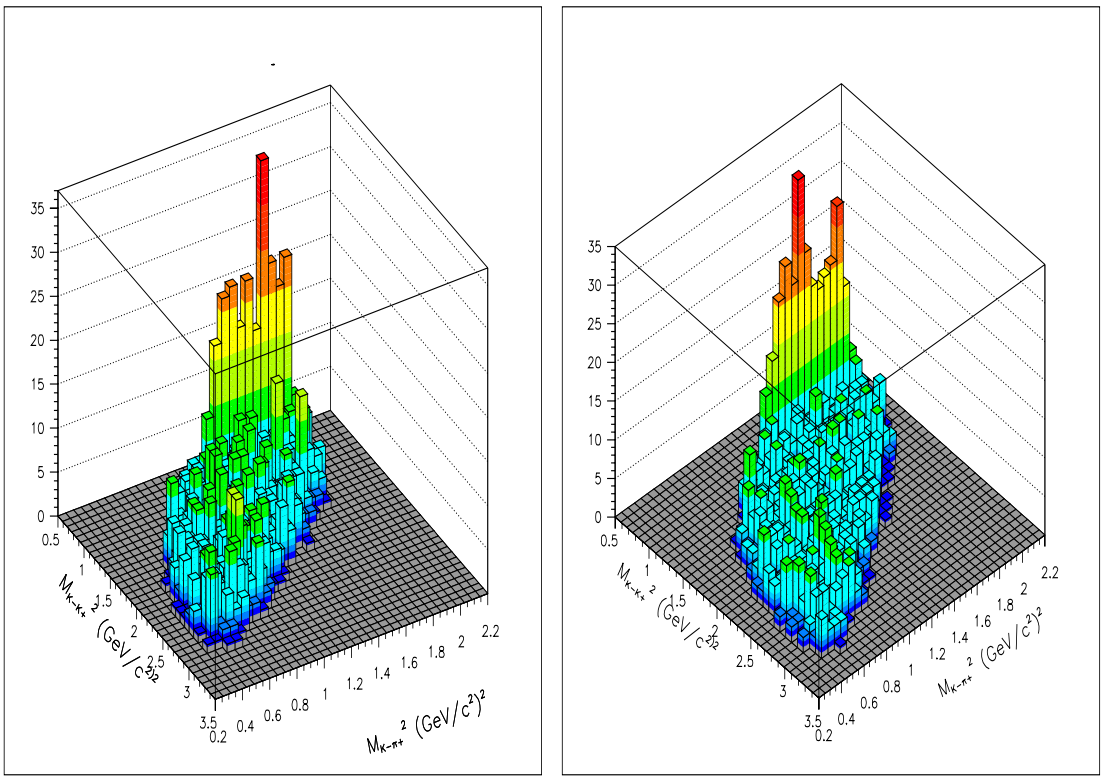

Figure 6.2: Low and high side band regions mini Monte Carlo simulation of $D^+ \to K^+K^-\pi^+$.

Comparing the *mmc* Dalitz plot in figure 6.1 with data Dalitz plot in figure 4.12, both the $\bar{K}^*(892)^0$ and ϕ lobes as well as asymmetries in the lobes are evident. On the other hand, there are no nodal structures of the ϕ lobes in the simulations shown in figure 6.2. This is expected as no Zemach terms are included in background parameterization equation 4.10 for the background simulation. However, there is clear evidence of Zemach nodes in the side band Dalitz plots in data in figure 4.7, which we attribute to events in the signal region spilling over into the sidebands.

The object of the mini-Monte Carlo exercise is to do a good job at simulating all aspects of the fitting process including obtaining the efficiency table, fitting the background when likelihood penalty terms are used, as well as the actual fits to the signal region which use these backgrounds and efficiencies. We begin by describing

our method for accounting for statistical fluctuations on Monte Carlo sample for the efficiency correction.

As discussed in Section 4.2.2, the efficiency in MC is obtained by constructing a binned table of accepted events with a large sample of fully simulated events initially generated with a uniform Dalitz plot. Each mini-MC trial begins with a new, statistically independent generation of a simulated Monte Carlo table where we use the the efficiency table obtained from the full Monte Carlo as the underlying "parent" distribution. This table is generated with the same statistics as that used in the actual full Monte Carlo used to correct the data. This table of efficiencies for each bin on the Dalitz plot is prestored with a bining scheme shown in fig 4.10. The color plot shown in fig 6.3 shows the efficiency of a sample that was generated which is in good agreement when compared with the D^+ efficiency color plot in fig. 4.9.

We next must simulate two independent background Dalitz distributions: 1) A background for the sidebands and 2) A background for the signal region. Again this simulation is done by using rejection from a "parent" distribution obtained through actual fits to the low, high and signal background regions. The background sideband Dalitz plot is first fit to get the "central" values and the error matrix required to construct the penalty terms. Again both backgrounds are generated with the number of background events observed in the data.

The final stage is to fit the simulated signal region which has signal events as well as an independent set of background events with the appropriate ratio. We next compare the returned fit parameters with input parameters which were initially obtained from our fit to the data. The mini Monte Carlo is analyzed using the same analysis algorithm as the actual data. The difference of fit results from mini Monte Carlo analysis and the input parameters divided by the error for an ensemble of mini Monte Carlo sets are plotted. Ideally this *pull* distribution would be Gaussian

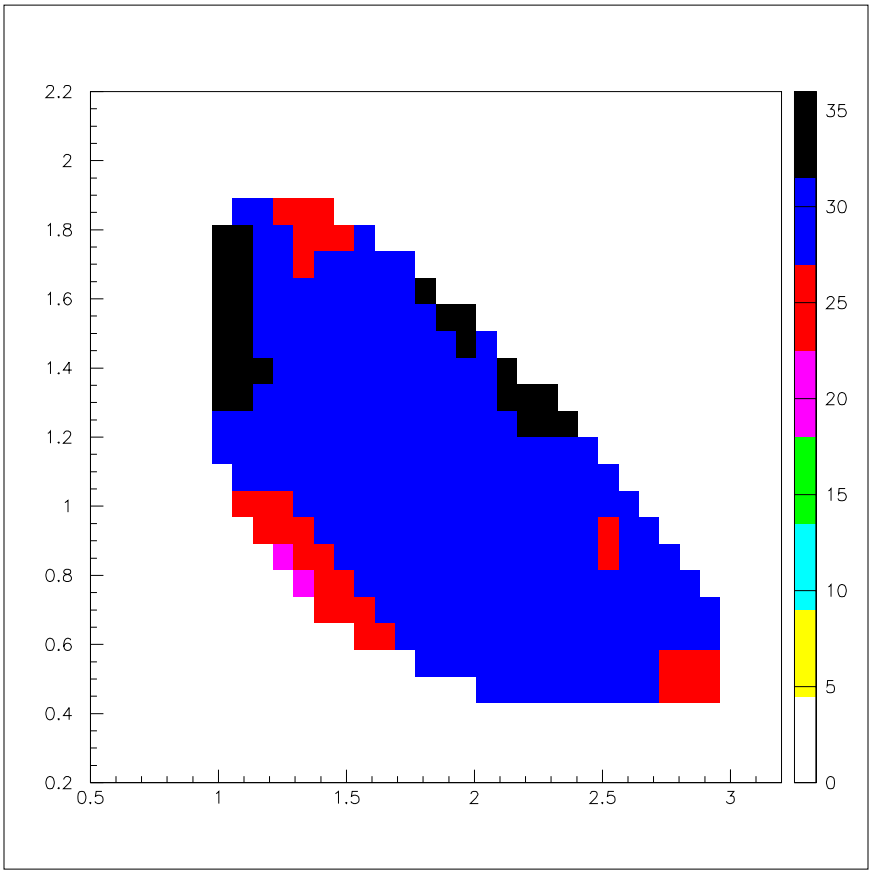

Figure 6.3: Simulated efficiency

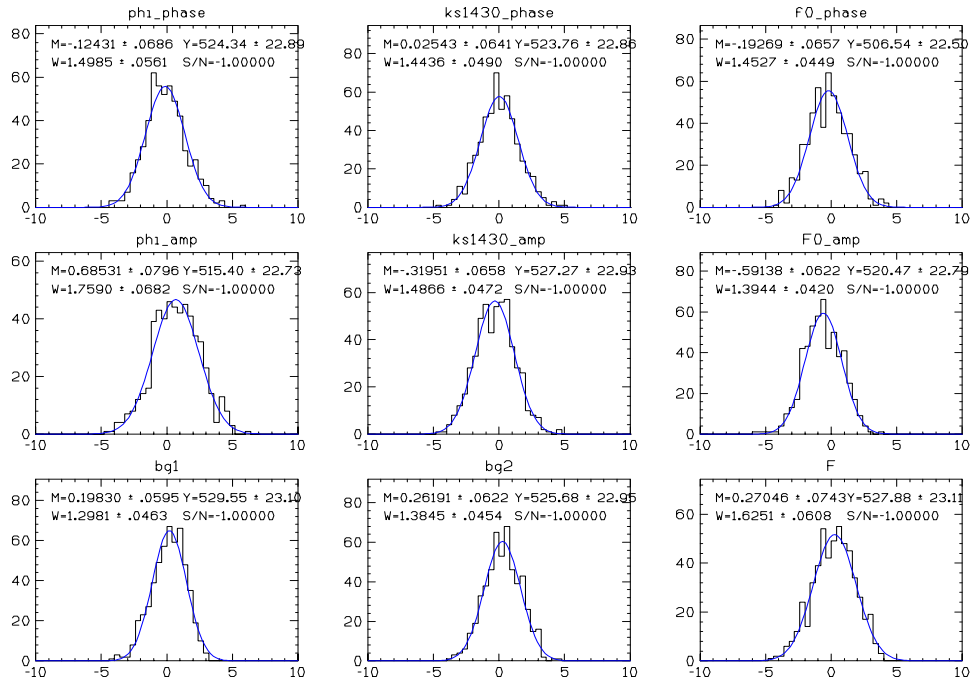

Figure 6.4: D^+ fit parameter pulls

distributed with a mean of 0 and $\sigma = 1$ for each parameter. Deviations from $\sigma = 1$ such that $\sigma > 1$ indicates that fit errors should be inflated, and any deviation from mean of 0 indicates that the fit estimates should be readjusted.

6.2.2 D^+ Pulls

The fit parameter pulls for $D^+ \to K^+K^-\pi^+$ are shown in Figure 6.4.

The pull summary is shown in Table 6.1. The widths, σ_{pull}'s, are greater than unity, this indicates that errors from the fits maybe underestimated and ought to be inflated by a factor of σ_{pull}. The mean of the pulls, μ_{pull} are not exactly zero, as one would expect in an ideal situation, however, they are relatively close to zero. The fit values must to be changed by adding $-(\mu_{\text{pull}} \times \sigma_{\text{fit}})$ to each corresponding fit value.

We are not positive what has caused the underestimation of the error bars but

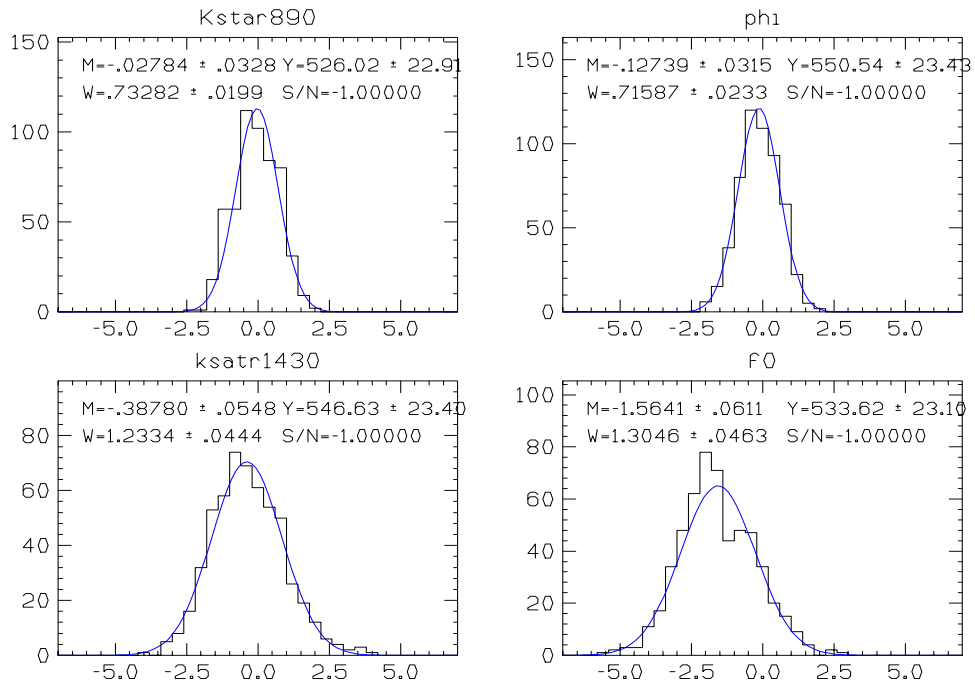

Figure 6.5: D^+ pulls on the four fit fractions. The fit fractions represent integrals over the intensity computed using the parameters returned from the Mini-MC.

one very likely possibility is due to the finite Monte Carlo statistics used to get the efficiency correction factor. We generally used a Monte Carlo sample with roughly 10 $\times$ the observed D^+ sample however our Monte Carlo sample was generated with a *uniform* Dalitz distribution. As a result, the region with high intensity such as in the vicinity of the narrow ϕ resonance, may have a much smaller MC to data ratio and fluctuations in the efficiency table may be significant. Assessing the effects of the finite MC statistics was a primary motivation for this Mini-MC study.

Table 6.1: D^+ fit parameter pull statistics

Parameter	Mean (μ_{pull})	Width (σ_{pull})
δ_ϕ	0.124 ± 0.069	1.499 ± 0.056
$\delta_{K^*(1430)}$	0.025 ± 0.064	1.444 ± 0.049
$\delta_{f_0(980)}$	0.193 ± 0.066	1.453 ± 0.045
a_ϕ	0.685 ± 0.080	1.759 ± 0.068
$a_{K^*(1430)}$	-0.320 ± 0.062	1.487 ± 0.045
$a_{f_0(980)}$	-0.270 ± 0.073	1.625 ± 0.061
a_ϕ^{bg}	0.198 ± 0.060	1.298 ± 0.046
$a_{K^*(1430)}^{bg}$	0.262 ± 0.062	1.385 ± 0.045
F	0.270 ± 0.074	1.625 ± 0.061

The fit fraction pulls are shown in Figure 6.5, and the summary are shown in Table 6.2. For the fit fractions the widths, σ_{pull} indicate that the errors for $\phi\pi^+$ and $\bar{K}^*(890)^0K^+$ are overestimated, therefore the fit errors could be deflated.

We are a bit surprised at the 1.6 σ pull in the f_0 fit parameter even though the pulls in the amplitudes and phases are much smaller. We believe that this might reflect non-linearities in the transformation which gets one from the amplitudes to fit

fractions.

Table 6.2: D^+ fit fraction pull statistics

Fit Fraction	Mean (μ_{pull})	Width (σ_{pull})
$f_{\bar{K}^*(890)^0 K^+}$	-0.027 ± 0.033	0.733 ± 0.020
$f_{\phi\pi^+}$	-0.127 ± 0.032	0.716 ± 0.023
$f_{K^*(1430)K^+}$	-0.388 ± 0.055	1.233 ± 0.044
$f_{f_0(980)\pi^+}$	-1.564 ± 0.061	1.305 ± 0.046

The fit parameters and fit fractions will be adjusted based on these pulls. The errors will be inflated if they are overestimated, but the errors that are underestimated will not be changed, as a more conservative result is preferred.

6.2.3 D_s^+ Pulls

The fit parameter pulls for $D_s^+ \to K^+K^-\pi^+$ are shown in Figure 6.6. The fit fraction pulls are shown in Figure 6.7

The fit parameter pull summary is shown in Table 6.3.The fit fraction pull summary is shown in Table 6.4.

We note that unlike the case for the D^+ there is a significant pull in the $\phi\pi^+$ amplitude by nearly 2 σ. We believe that this is partially due to the fact that the $\phi\pi^+$ contribution is both much cleaner and much more prevalent in the D_s^+ Dalitz plot compared to the D^+ Dalitz plot. As a result it is much more susceptible to bias due to neglecting mass smearing in the fit. To verify this, we turned off smearing in the mini-MC simulation process and re-ran the fits. The bias in the $\phi\pi^+$ amplitude is somewhat reduced.

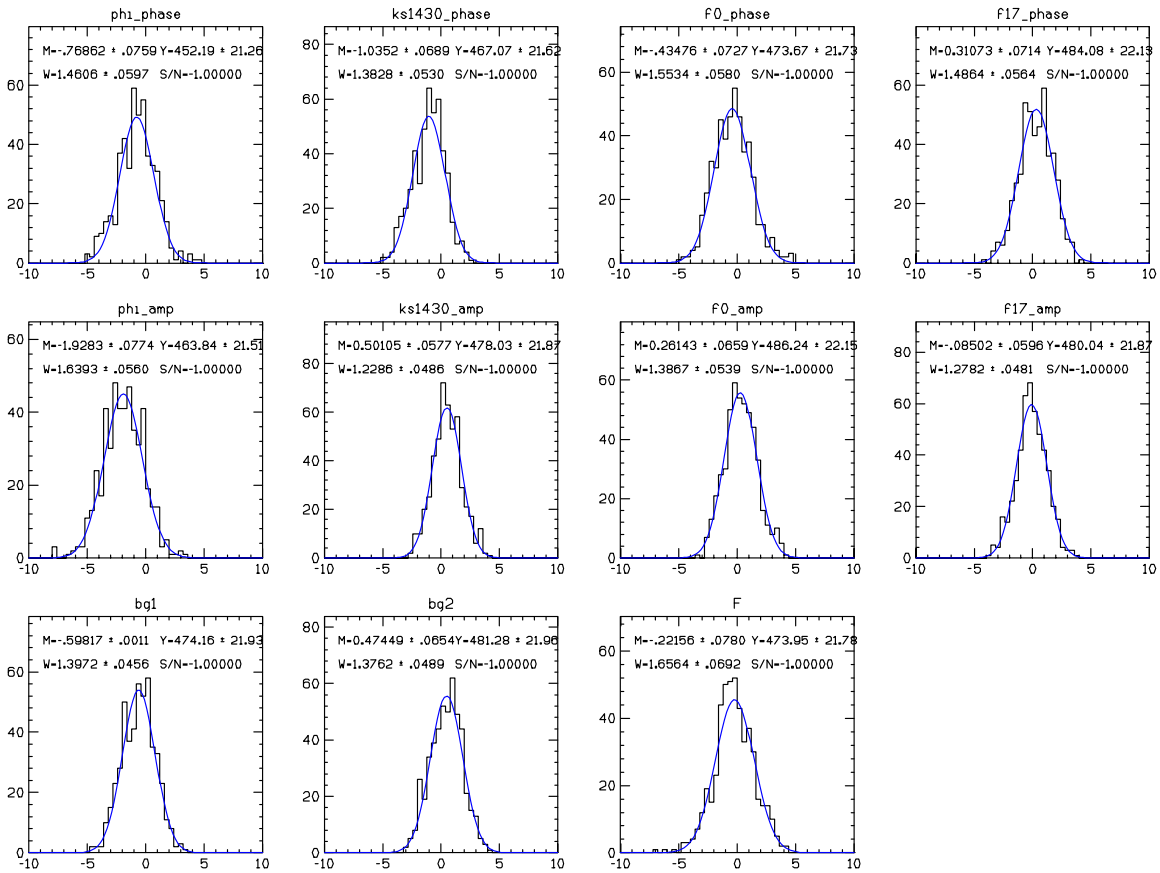

Figure 6.6: D_s^+ fit parameter pulls

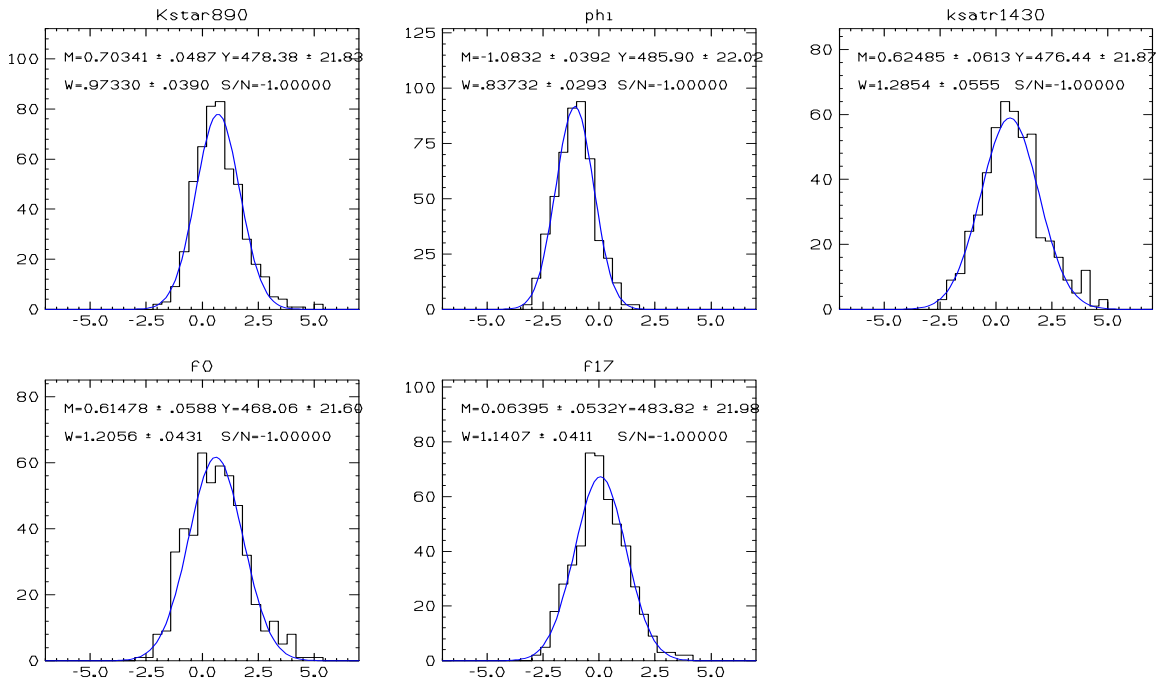

Figure 6.7: D_s^+ pulls five fit fractions. The fit fractions represent integrals over the intensity computed using the parameters returned from the Mini-MC.

Table 6.3: D_s^+ fit parameter pull statistics

Parameter	Mean (μ_{pull})	Width (σ_{pull})
δ_ϕ	-0.769 ± 0.076	1.461 ± 0.060
$\delta_{K^*(1430)}$	1.035 ± 0.069	1.383 ± 0.053
$\delta_{f_0(980)}$	-0.435 ± 0.073	1.553 ± 0.058
$\delta_{f_J(1710)}$	0.317 ± 0.071	1.486 ± 0.056
a_ϕ	-1.928 ± 0.077	1.639 ± 0.056
$a_{K^*(1430)}$	0.510 ± 0.058	1.229 ± 0.049
$a_{f_0(980)}$	0.261 ± 0.066	1.387 ± 0.054
$a_{f_J(1710)}$	-0.085 ± 0.060	1.278 ± 0.048
a_ϕ^{bg}	-0.598 ± 0.001	1.397 ± 0.046
$a_{K^*(1430)}^{bg}$	0.474 ± 0.065	1.376 ± 0.049
F	-0.222 ± 0.078	1.656 ± 0.069

Table 6.4: D_s^+ fit fraction pull statistics

Fit Fraction	Mean (μ_{pull})	Width (σ_{pull})
$f_{\bar{K}^*(890)^0 K^+}$	0.703 ± 0.049	0.973 ± 0.039
$f_{\phi\pi^+}$	-1.083 ± 0.039	0.837 ± 0.029
$f_{K^*(1430)K^+}$	0.625 ± 0.061	1.285 ± 0.056
$f_{f_0(980)\pi^+}$	0.615 ± 0.059	1.206 ± 0.043
$f_{f_J(1710)\pi^+}$	0.064 ± 0.053	1.141 ± 0.041

6.2.4 D^0 Pulls

The fit parameter pulls for $D_s^+ \to K^+K^-\pi^+$ are shown in Figure 6.8. The fit fraction pulls are shown in Figure 6.9

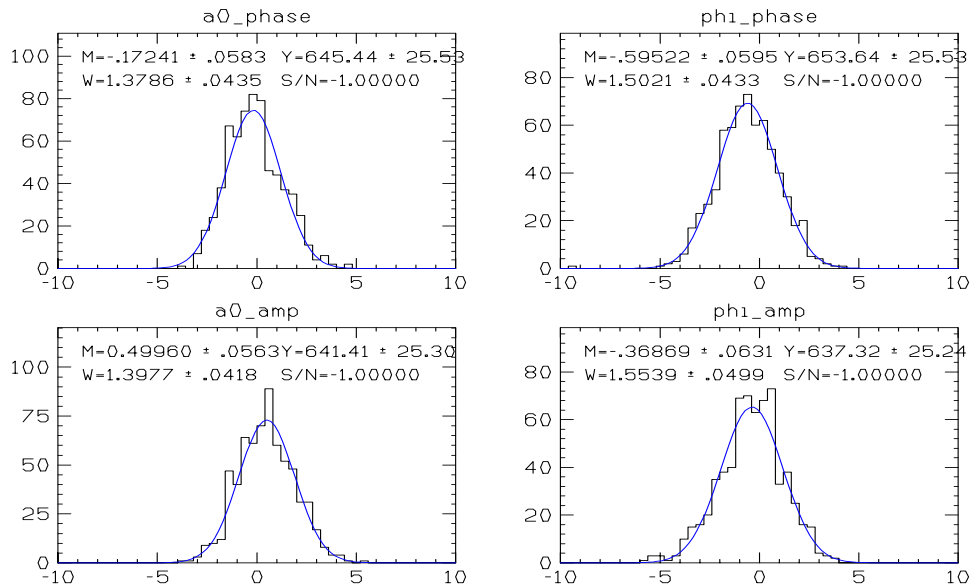

Figure 6.8: D^0 fit parameter pulls

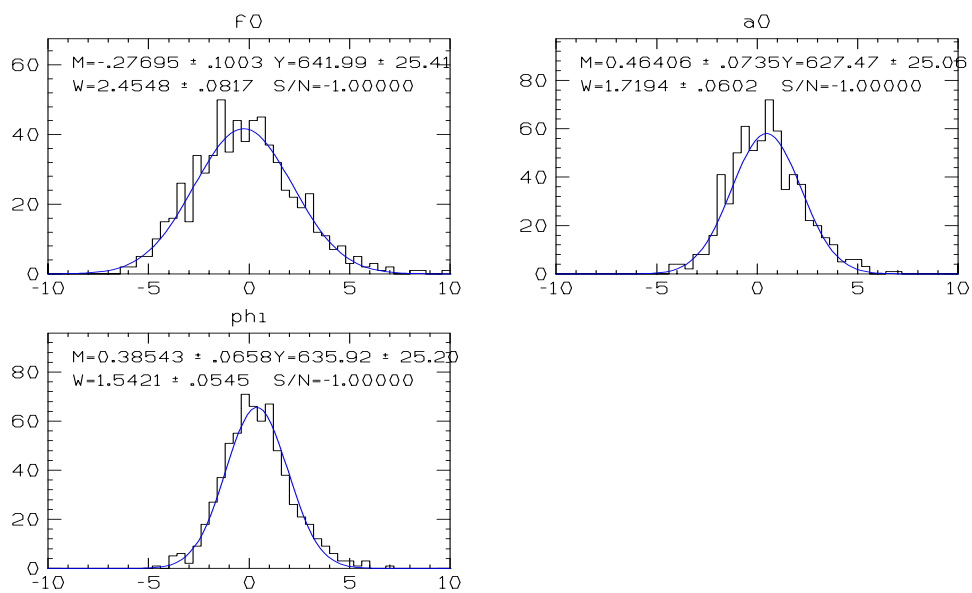

Figure 6.9: D^0 fit fraction pulls

The four fit parameter pull summary is shown in Table 6.5, which show a a shift of less than 0.6 σ. The fit fraction pull summary is shown in Table 6.6, which show a shift of less than 0.5 σ.

Table 6.5: D^0 fit parameter pull statistics

Parameter	Mean (μ_{pull})	Width (σ_{pull})
$\delta_{a_0^{\pm}(980)K^{\mp}}$	-0.172 ± 0.058	1.379 ± 0.044
$\delta_{\phi K_s}$	-0.595 ± 0.060	1.502 ± 0.043
$a_{a_0^{\pm}(980)K^{\mp}}$	0.500 ± 0.056	1.398 ± 0.042
$a_{\phi K_s}$	-0.369 ± 0.063	1.554 ± 0.050

Table 6.6: D^0 fit fraction pull statistics

Fit Fraction	Mean (μ_{pull})	Width (σ_{pull})
$f_{f_0(980)K_s}$	-0.278 ± 0.100	2.455 ± 0.082
$f_{a_0^{\pm}(980)K^{\mp}}$	0.464 ± 0.074	1.719 ± 0.060
$f_{\phi K_s}$	0.385 ± 0.066	1.542 ± 0.055

In addition, Figure 6.10 shows the fit fraction pulls in the ϕ region of $D^0 \to K_s K^+ K^-$ Dalitz plot, and the statistics are summarized in table 6.7. The pulls are shifted by less than 0.4 σ.

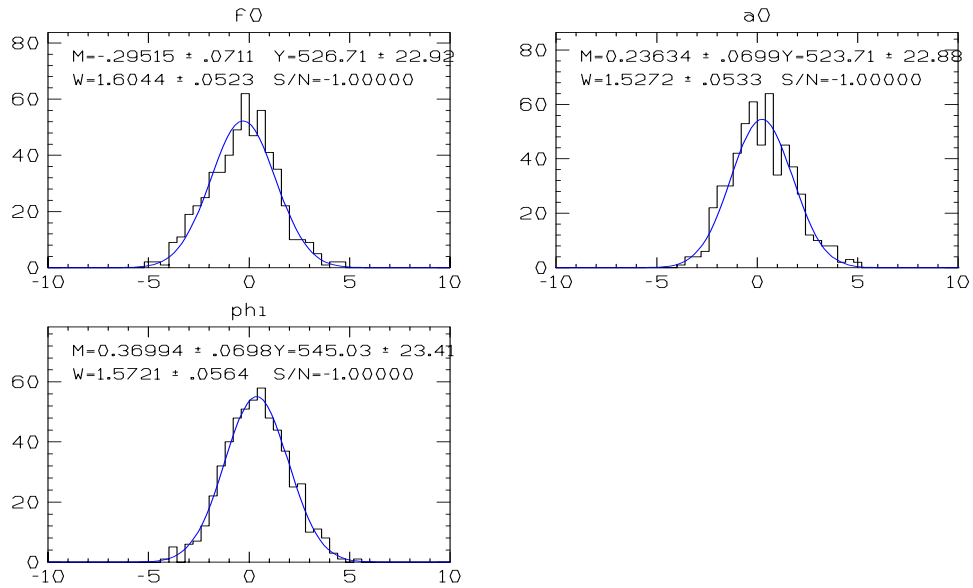

Figure 6.10: D^0 fit fraction pulls in the ϕ region $M^2_{K^+K^-} < 1.1$

Table 6.7: D^0 fit fraction pull statistics in the ϕ region $M^2_{K^+K^-} < 1.1$

Fit Fraction	Mean (μ_{pull})	Width (σ_{pull})
$f_{f_0(980)K_s}$	-0.295 ± 0.071	1.604 ± 0.052
$f_{a_0^{\pm}(980)K^{\mp}}$	0.236 ± 0.070	1.527 ± 0.053
$f_{\phi K_s}$	0.340 ± 0.070	1.572 ± 0.056

Chapter 7

Estimating Systematic Errors

Although estimation of the statistical error is straightforward , computing systematic errors is more of an art than an science except for the simplest sort of measurements. In the Dalitz analyses presented here, the dominant systematic uncertainty is likely to come from handling of the background, and efficiency. We feel that perhaps the most reliable way of estimating the systematic error on the amplitude, phases, and fit fractions, is to see how these quantities change as features of the analysis are changed. The variants considered involve changing the underlying cuts used to bring out the signal, the way we compute the efficiency, and the way the background is parameterized and subtracted.

For each mode, our summary tables have inflated statistical errors and adjusted central values in accordance with the mini-MC studies of Chapter 6.

We have computed the systematic error based on the *sample standard deviation* of the alternative fits.

$$\sigma_{sys} = \sqrt{\frac{\sum_i^N x_i^2 - N < x >^2}{N-1}} \tag{7.1}$$

where $< x >= \sum_i x_i/N$. The sample standard deviation is justified since we believe the results from these semi-arbitrary technique choices are *a priori* equally likely.

This formula also has the virtue that the quoted systematic error to be essentially independent of the number of systematics sources considered. This method, described more fully in Reference [48], was used for assessing systematics in many E687 and FOCUS publications.

To a certain extent, using the sample standard deviation of alternative fits as an estimate of systematic errors is somewhat conservative since it ascribes some of the variation due to statistical fluctuation of disjoint samples to the systematic as well as statistical error. This is especially true when one compares results from samples satisfying, for example, loose cuts versus tight cuts.

7.1 $D^+ \to K^+K^-\pi^+$ Systematics

We have chosen to compute several sources of systematic errors separately and then add these contributions in quadrature for an overall systematic. We believe this approach should result in a very conservative systematic error.

To assess a systematic due to variation in cuts, we ran our fit with the 9 different cut choices indicated in Table 7.1. The 9 variants, are for 3 different detachments, followed by 5 sets where a standard analysis cut is removed or significantly loosened, followed by a 9th cut set where the primary isolation cut is replaced by a cut requiring that the $K^-K^+\pi^+$ is not consistent with the decay chain: $D^{*+} \to (K^-K^+X)\pi^+$.[1] Figure 7.2 shows that cut variant # 4, where the "out of target" cut has been removed, has significantly more background, that the other 8 cut variants and thus provides a

[1]We established in Chapter 4, Section 4.1 that the primary isolation cut significantly reduced contamination from this source. We also believe that the primary isolation cut is likely to create an efficiency depletion at the edge of the Dalitz plot and for that reason might be a good cut to eliminate if we could get a reasonable fit through a substitution. This was not successful as we will show.

good gauge of background systematic uncertainty.

We then assess the cut variant systematic by computing the sample variance for those fits which returned acceptable projections according to the criteria of Figure 7.1. Figure 7.1 shows that we are unable to get acceptable fits once the kaonicity cut is lowered from 3 to 1 or whenever the primary isolation cut is eliminated which leaves us with 6 acceptable cut variants. The cut variant systematic for the D^+ results are summarized in the 3rd column of table 7.2. Figures 7.3 and 7.4 and 7.5 give a graphical summary for the amplitude, phase, and fit fraction systematics as a function of cut variant.

To gauge the systematic uncertainty which can be attributed to the efficiency correction we re-ran the fits with larger efficiency correction bins (using 13×13 rather than the standard 25×25). This systematic gives an idea on whether or not we are using small enough efficiency bins given the gradient of the efficiency function and the required precision of the correction given our statistical error. The red points in Figures 7.3 and 7.4 and 7.5 give a graphical summary for the amplitude, phase, and fit fraction systematics as a function of cut variant with the larger efficiency bins. The "efficiency" systematic summarized in the 4th column of Table 7.2 is the sample standard deviation between the standard efficiency binning and the coarser binning for our "standard" cuts (cut variant #1).[2]

The third source of systematic uncertainty is assessed by removing the likelihood penalty terms which tie the background shape in the signal region to that found in the sidebands through a χ^2 term based on the error matrix of the sideband, background fit. This means that the background shape is entirely determined from the signal region. The blue points in Figures 7.3 and 7.4 and 7.5 give a graphical summary for

[2]For the case of just two fit variants, the sample standard deviation is just the difference in values divided by $\sqrt{2}$.

the amplitude, phase, and fit fraction systematics as a function of cut variant when the likelihood penalty is removed. Quite a few of the blue points are missing indicating that we were unable to achieve fit convergence without the likelihood penalty terms to help "guide" the fit. Again the "background likelihood penalty" systematic summarized in the 5th column of Table 7.2 is the sample standard deviation between the standard fit with likelihood terms and the fit with no likelihood penalty terms for our "standard" cuts (cut variant #1).

The sixth column of of Table 7.2 gives the fit result, the statistical error and a very conservative "grand" systematic error obtained by adding the cut variant, efficiency binning, and likelihood penalty systematic errors in quadrature.

Here are some general comments concerning the systematic errors.

1. The systematic errors on amplitudes and phases are generally larger than the statistical errors (typically by a factor of 1.5-2.) quoted in Table 7.2.

2. The largest contribution to the systematic error on amplitudes for narrow resonances tends to be the efficiency correction; while for broader resonances it tends to be the cut variation. We surmise that the broader, spin 0 resonances are harder to distinguish from the background and therefore more sensitive to background changes as one loosens analysis cuts. The likelihood penalty appears to be a minor player throughout.

3. The pattern on sources for systematic error for the phases is less clear although the pattern is similar to that observed in the amplitudes.

4. The systematic errors on fit fractions tend to be comparable to the statistical error.

Table 7.1: D^+ and D_s^+ cut variants

CUT Variant	Cuts					
	l/σ	num. of σ Oom	CL1	CL2	kaonicity	Dstar
1	9.	3.	0.001	0.01	3.(5.)	-
2	6.	3.	0.001	0.01	3.(5.)	-
3	3.	3.	0.001	0.01	3.(5.)	-
4	9.	-	0.001	0.01	3.(5.)	-
5	9.	3.	-	0.01	3.(5.)	-
6	9.	3.	0.001	-	3.(5.)	-
7	9.	3.	0.001	0.01	2.(2.)	-
8	9.	3.	0.001	0.01	1.(1.)	-
9	9.	3.	-	0.01	3.(5.)	0.16

Table 7.2: D^+ Errors

Parameter	Statistical	Systematics			Values
		Cut Variant	Efficiency	Bg Like	
$a_{\bar{K}^*(890)^0K^+}$	-	-	-	-	1.0 (fixed)
$a_{f_0(980)\pi^+}$	0.099	0.030	0.158	0.008	$1.940 \pm 0.099 \pm 0.161$
$a_{\phi\pi^+}$	0.025	0.014	0.028	0.002	$1.118 \pm 0.025 \pm 0.031$
$a_{K^*(1430)K^+}$	0.129	0.107	0.110	0.040	$2.966 \pm 0.129 \pm 0.159$
$a_{f_J(1710)\pi^+}$	0.048	0.083	0.012	0.009	$0.616 \pm 0.048 \pm 0.084$
$\delta_{\bar{K}^*(890)^0K^+}$	-	-	-	-	0° (fixed)
$\delta_{f_0(980)\pi^+}$	2.6^o	1.3^o	2.3^o	0.5^o	$-100.0 \pm 2.6 \pm 2.7^o$
$\delta_{\phi\pi^+}$	4.0^o	2.2^o	5.2^o	0.1^o	$118.9 \pm 4.0 \pm 6.7^o$
$\delta_{K^*(1430)K^+}$	2.6^o	1.8^o	1.2^o	0.6^o	$109.4 \pm 2.6 \pm 2.2^o$
$\delta_{f_J(1710)\pi^+}$	4.0^o	5.5^o	4.3^o	3.1^o	$-59.6 \pm 4.0 \pm 7.6^o$
$f_{\bar{K}^*(890)^0K^+}$	0.013	0.003	0.007	0.004	$0.285 \pm 0.013 \pm 0.009$
$f_{f_0(980)\pi^+}$	0.027	0.007	0.042	0.002	$0.301 \pm 0.027 \pm .042$
$f_{\phi\pi^+}$	0.015	0.006	0.006	0.006	$0.283 \pm 0.015 \pm 0.010$
$f_{K^*(1430)K^+}$	0.030	0.022	0.017	0.004	$0.362 \pm 0.030 \pm 0.028$
$f_{f_J(1710)\pi^+}$	0.005	0.005	0.001	0.001	$0.032 \pm 0.005 \pm 0.005$

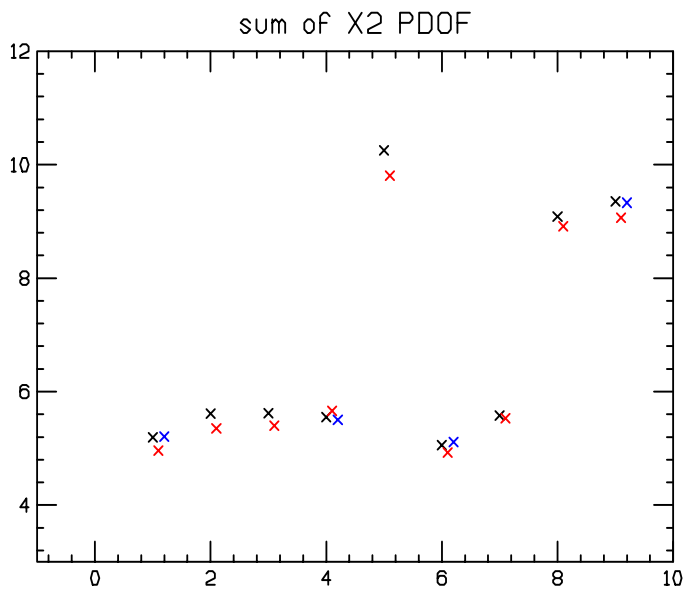

Figure 7.1: The sum of the χ^2/D.o.F. for the three mass projections as a function of cut variant. We plot this for our standard fit technique with $\Delta W_K > 3$ (black), and with $\Delta W_K > 5$ (green), a fit with only 13×13 bins of efficiency instead of our standard 25×25 bin correction (red), and a fit with the background likelihood penalty terms removed (blue). We will use χ^2/D.o.F < 6 as our criteria for an "acceptable" fit.

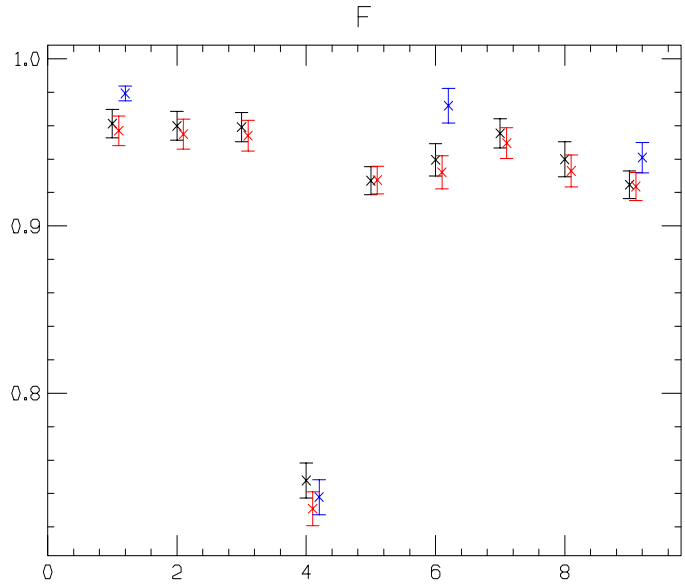

Figure 7.2: The signal fraction in the signal region as a function of cut variant. We plot this for our standard fit technique with $\Delta W_K > 3$ (black), and with $\Delta W_K > 5$ (green), a fit with only 13×13 bins of efficiency instead of our standard 25×25 bin correction (red), and a fit with the background likelihood penalty terms removed (blue).

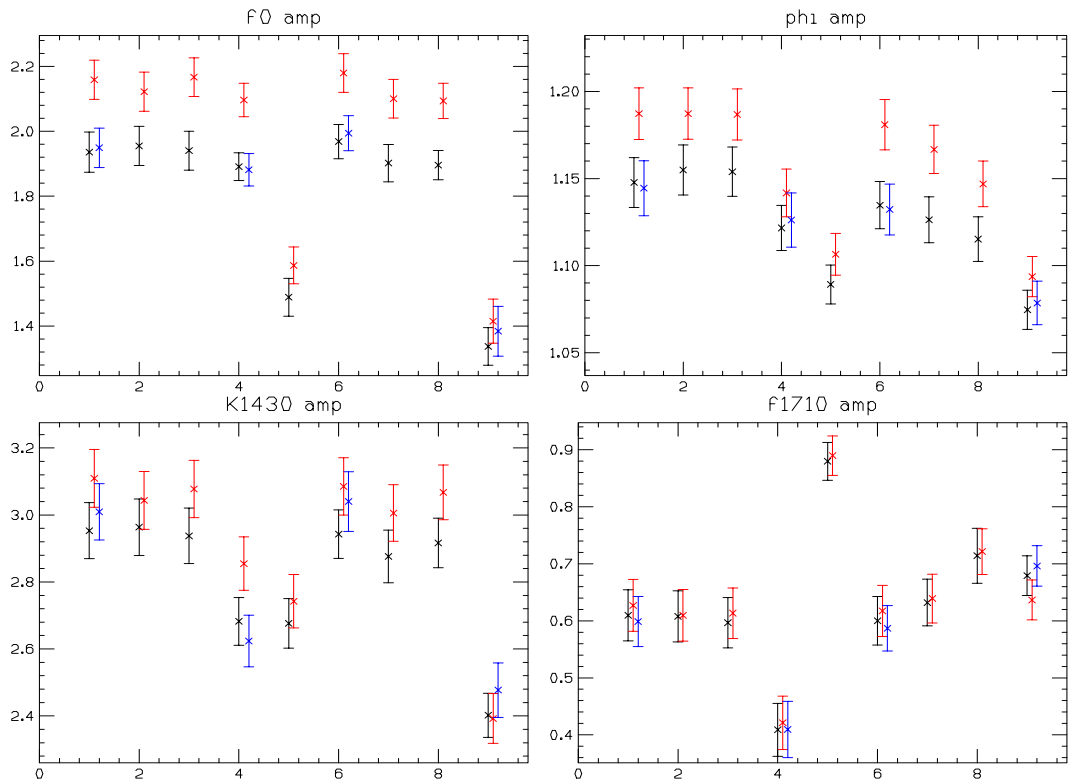

Figure 7.3: D^+ amplitude systematics. We plot each amplitude as a function of cut variant. We plot this for our standard fit technique with $\Delta W_K > 3$ (black), and with $\Delta W_K > 5$ (green), a fit with only 13×13 bins of efficiency instead of our standard 25×25 bin correction (red), and a fit with the background likelihood penalty terms removed (blue).

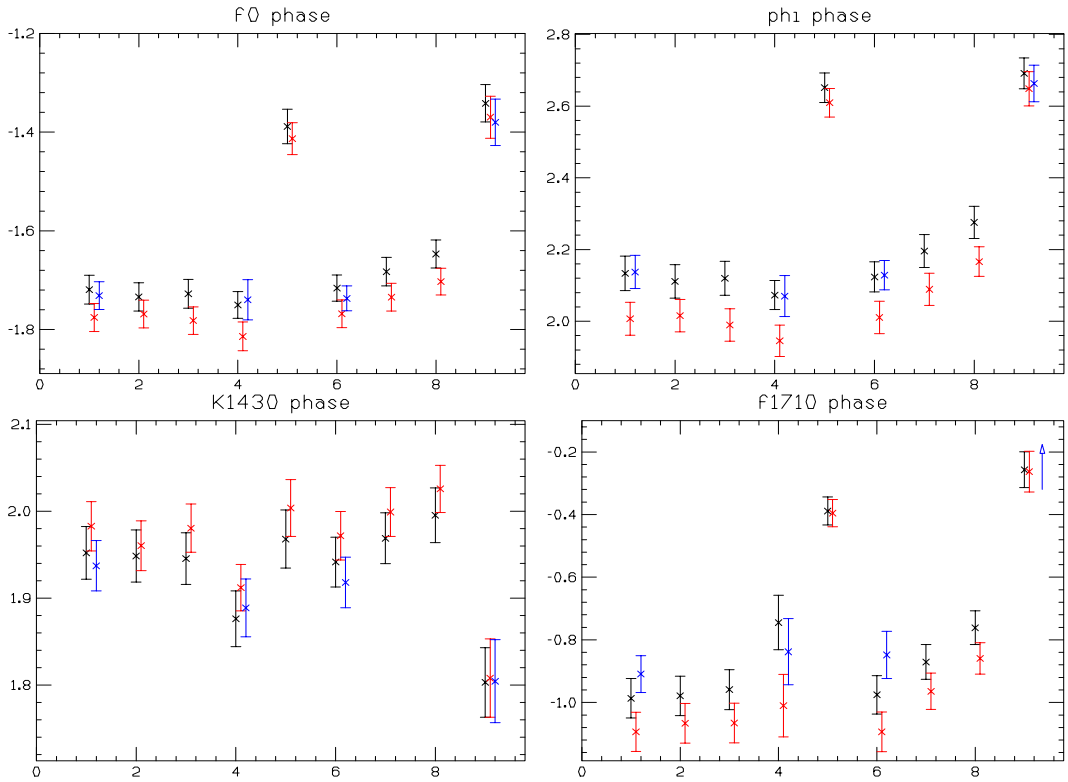

Figure 7.4: D^+ phase systematics. We plot each phase (in radians) as a function of cut variant. We plot this for our standard fit technique with $\Delta W_K > 3$ (black), and with $\Delta W_K > 5$ (green), a fit with only 13×13 bins of efficiency instead of our standard 25×25 bin correction (red), and a fit with the background likelihood penalty terms removed (blue).

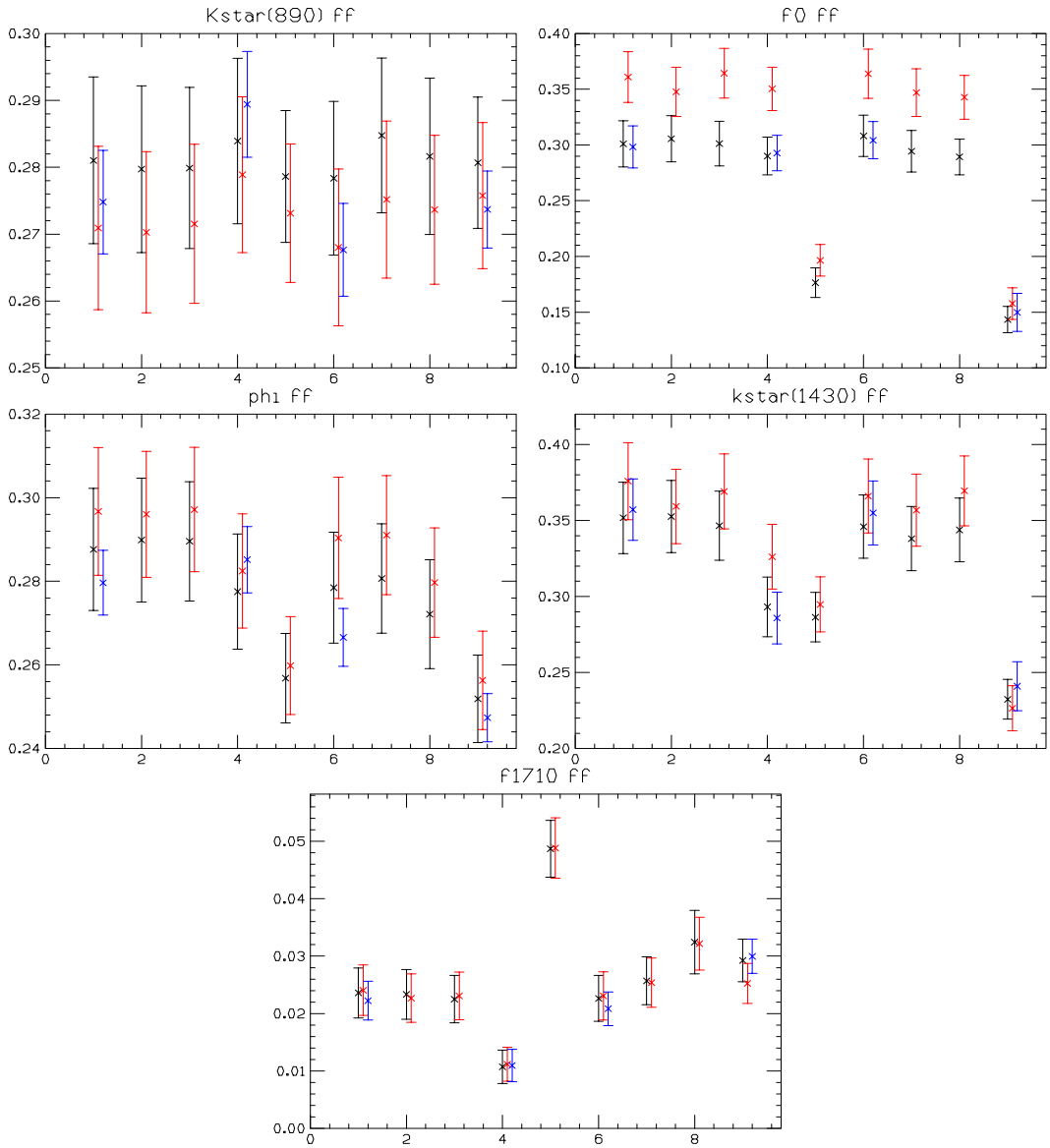

Figure 7.5: D^+ fit fraction systematics. We plot each fit fraction as a function of cut variant. We plot this for our standard fit technique with $\Delta W_K > 3$ (black), a fit with only 13×13 bins of efficiency instead of our standard 25×25 bin correction (red), and a fit with the background likelihood penalty terms removed (blue).

7.2 $D_s^+ \to K^+K^-\pi^+$ Systematics

We assess the systematics for the D_s^+ in an essentially identical way as the method used for the D_+. The same set of standard cuts and cut variants, shown in Table 7.1, is used for both states. The variation in the amplitude, phases, and fit fractions for the D_s^+ are shown in Figures 7.8, 7.9, and 7.10. The sum of the χ^2/D.o.F. for the three Dalitz projections are shown for the cut variants of the D_s^+ in Figure 7.6. As was the case with the D^+ we were unable to get respectable projection χ^2 without the primary isolation cut (cut variants # 5 and #9) or when the kaonicity cut is lowered from 3 to 1 (cut variant #8). We will exclude these variants in computing the cut variant systematic for the D_s^+ as we did for the D^+. Table 7.3 summarizes the systematic error calculation for the the D_s^+ amplitudes, phases, and fit fractions. Here are a few observations on the results.

1. The systematic error on the $\phi\pi^+$ amplitude for the D_s^+ is larger than the statistical error by a factor of 3 with the dominant contribution coming from the efficiency systematic. For the case of the D^+, the systematic error on the $\phi\pi^+$ amplitude was less than 1.5 times the statistical error which was more in line with the the systematic/statistical error ratio of the other 3 resonances. We clearly could reduce the systematic error on the $\phi\pi^+$ amplitude through the use of smaller efficiency bins and more Monte Carlo.

2. The large systematic error on the $\phi\pi^+$ amplitude for the D_s^+ relative to the D^+ is likely to be related to the much larger bias in this amplitude in the D_s^+ revealed to the mini-MC studies discussed in Chapter 6. We aren't sure what creates the extra sensitivity of the $\phi\pi^+$ amplitude for the D_s^+.

3. Systematic errors on the $f_J(1710)$ are smaller than the statistical error.

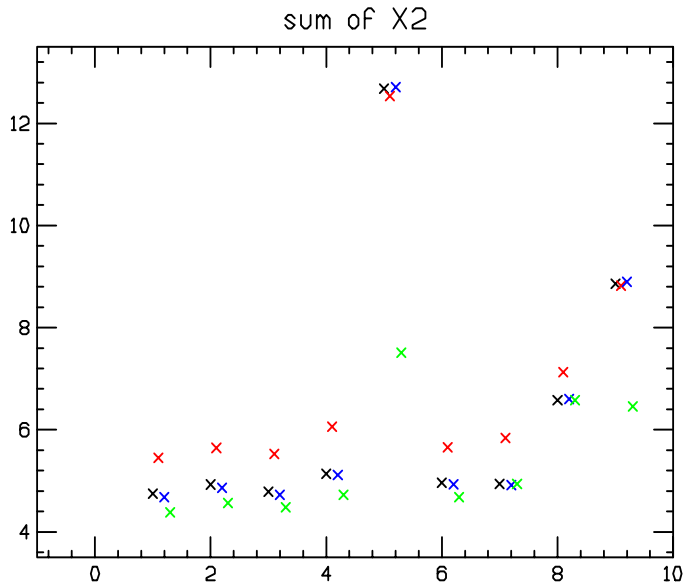

Figure 7.6: The D_s^+ sum of the χ^2/D.o.F. for the three mass projections as a function of cut variant. We plot this for our standard fit technique with $\Delta W_K > 3$ (black), and with $\Delta W_K > 5$ (green), a fit with only 13×13 bins of efficiency instead of our standard 25×25 bin correction (red), and a fit with the background likelihood penalty terms removed (blue). We will use χ^2/D.o.F < 6 as our criteria for an "acceptable" fit.

4. Except for the $f_J(1710)$, the systematic errors on the fit fraction and phases are roughly twice the statistical errors.

7.3 $D^0 \to K_s^o K^- K^+$ Systematics

We assess the systematics for the D^0 in an analogous way as that used for the D^+ and D_s^+. We consider the 8 cut variants listed in Table 7.4. These variants include different cuts on the kaonicity applied to both kaons, cuts on the K_s^+ quality, different cuts on detachment, and cuts on the isolation of the secondary vertex. Because it is necessary to employ $D^{*+} - D^0$ tagging to determine the strangeness of the K_s^o as discussed in Chapter 5, Section 5.1, the signal is necessarily very clean. As a

Table 7.3: D_s^+ Errors

Param.	Stat.	Systematics			Values
		Cut Var. ($W_K > 5$)	Eff.	Bg. Like.	
$a_{\bar{K}^*(890)^0 K^+}$	–	–	–	–	1.0 (fixed)
$a_{f_0(980)\pi^+}$	0.056	0.074	0.001	0.010	$1.202 \pm 0.056 \pm 0.075$
$a_{\phi\pi^+}$	0.021	0.023	0.054	0.009	$1.026 \pm 0.021 \pm 0.059$
$a_{K^*(1430)K^+}$	0.065	0.112	0.037	0.018	$0.824 \pm 0.065 \pm 0.119$
$a_{f_J(1710)\pi^+}$	0.042	0.031	0.016	0.007	$0.399 \pm 0.042 \pm 0.036$
$\delta_{\bar{K}^*(890)^0 K^+}$	–	–	–	–	0° (fixed)
$\delta_{f_0(980)\pi^+}$	5.4^o	8.6^o	3.6^o	0.09^o	$131.2 \pm 5.4 \pm 9.3^o$
$\delta_{\phi\pi^+}$	5.4^o	7.6^o	5.0^o	0.07^o	$150.2 \pm 5.4 \pm 9.1^o$
$\delta_{K^*(1430)K^+}$	7.7^o	11.0^o	12.0^o	1.3^o	$121.7 \pm 7.7 \pm 16.3^o$
$\delta_{f_J(1710)\pi^+}$	11.3^o	1.8^o	3.0^o	0.5^o	$80.4 \pm 11.3 \pm 3.5^o$
$f_{\bar{K}^*(890)^0 K^+}$	0.0153	0.0189	0.0213	0.0062	$0.5026 \pm 0.0153 \pm 0.0291$
$f_{f_0(980)\pi^+}$	0.0108	0.0139	0.0008	0.0006	$0.1477 \pm 0.0108 \pm 0.0139$
$f_{\phi\pi^+}$	0.0134	0.0118	0.0243	0.0022	$0.3989 \pm 0.0134 \pm 0.0271$
$f_{K^*(1430)K^+}$	0.0075	0.0143	0.0062	0.0017	$0.0577 \pm 0.0075 \pm 0.0157$
$f_{f_J(1710)K^+}$	0.0033	0.0040	0.0009	0.0004	$0.0196 \pm 0.0033 \pm 0.0041$

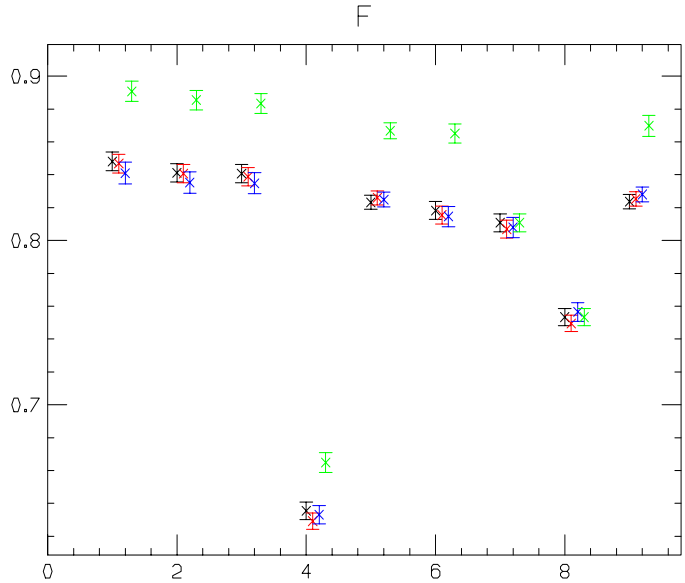

Figure 7.7: The D_s^+ signal fraction in the signal region as a function of cut variant. We plot this for our standard fit technique with $\Delta W_K > 3$ (black), and with $\Delta W_K > 5$ (green), a fit with only 13×13 bins of efficiency instead of our standard 25×25 bin correction (red), and a fit with the background likelihood penalty terms removed (blue).

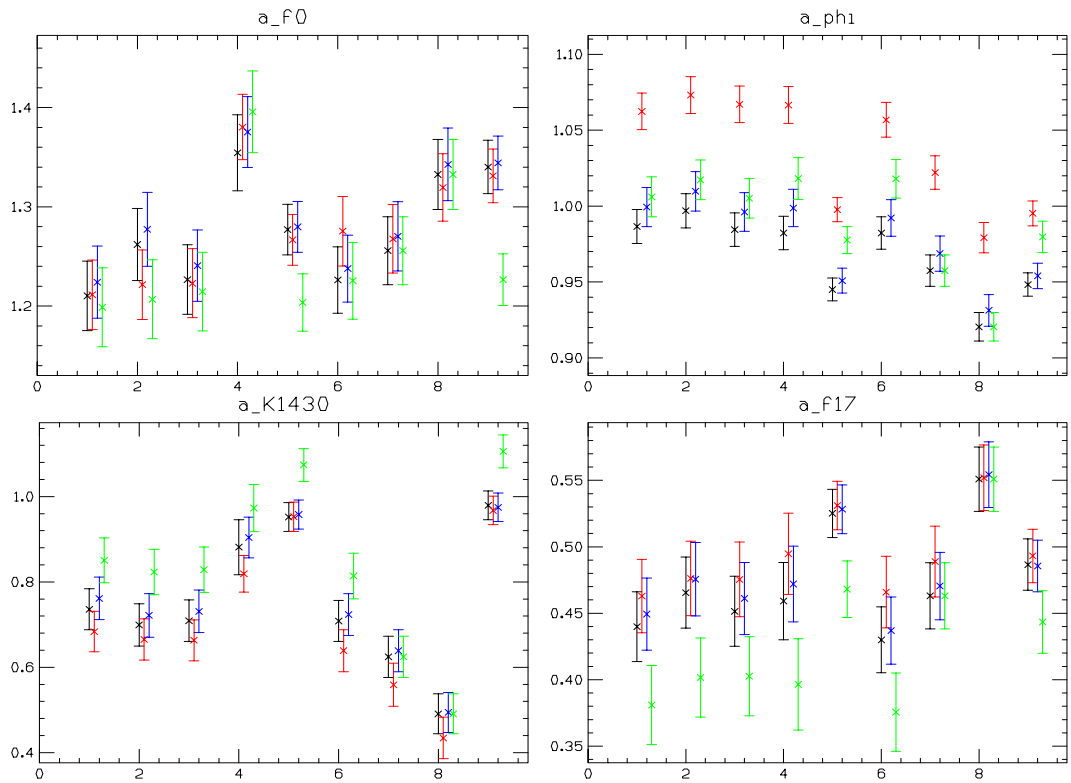

Figure 7.8: D_s^+ amplitude systematics. We plot each amplitude as a function of cut variant. We plot this for our standard fit technique with $\Delta W_K > 3$ (black), and with $\Delta W_K > 5$ (green), a fit with only 13×13 bins of efficiency instead of our standard 25×25 bin correction (red), and a fit with the background likelihood penalty terms removed (blue).

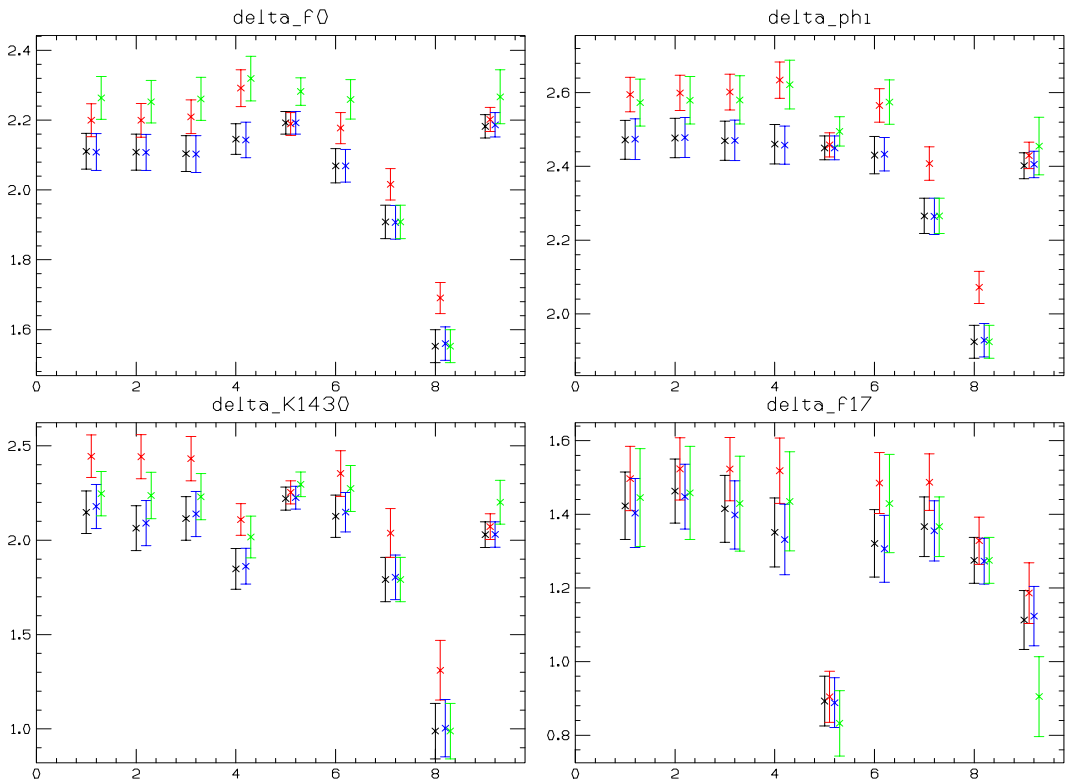

Figure 7.9: D_s^+ phase systematics. We plot each phase (in radians) as a function of cut variant. We plot this for our standard fit technique with $\Delta W_K > 3$ (black), and with $\Delta W_K > 5$ (green), a fit with only 13×13 bins of efficiency instead of our standard 25×25 bin correction (red), and a fit with the background likelihood penalty terms removed (blue).

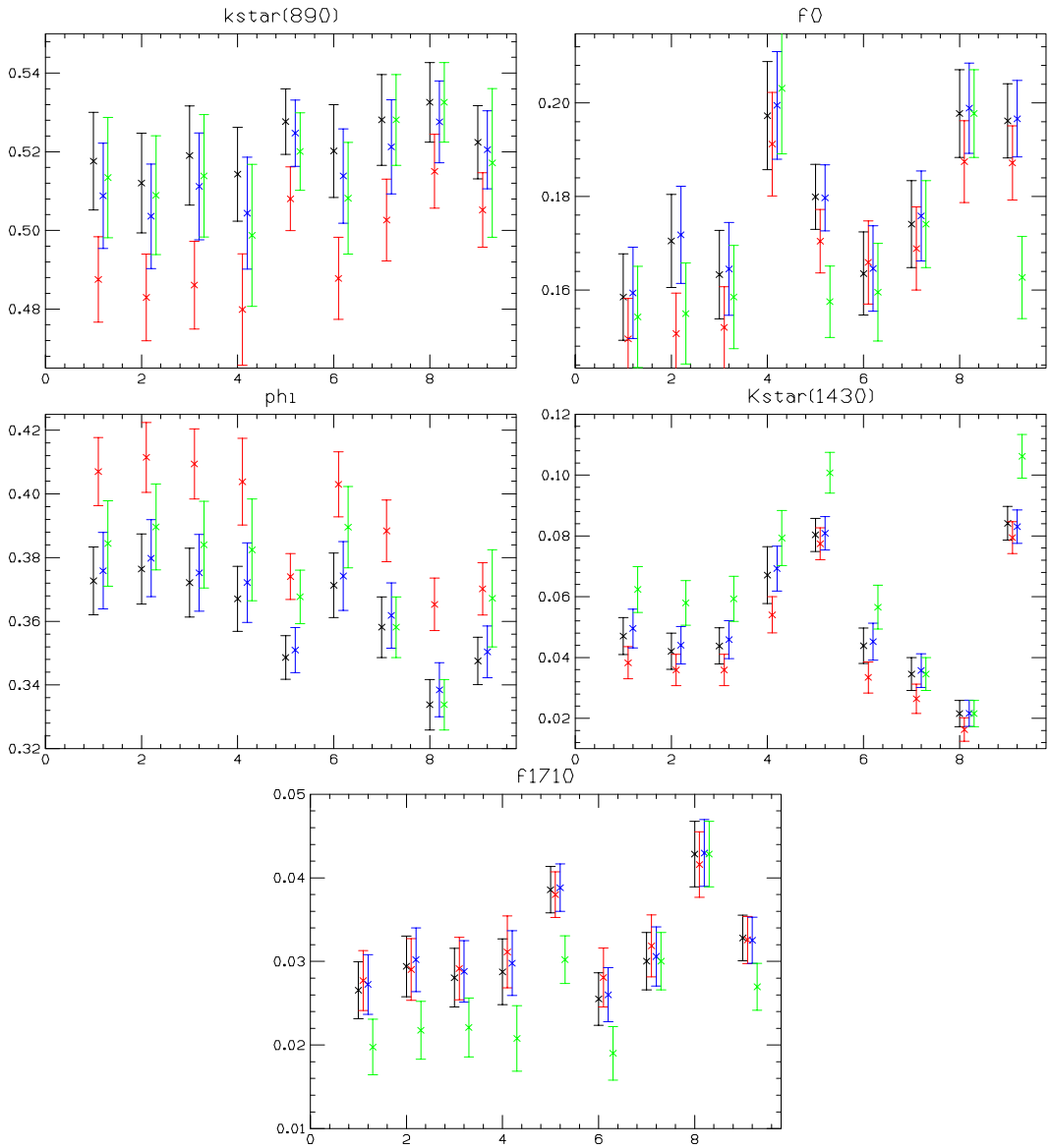

Figure 7.10: D_s^+ fit fraction systematics. We plot each fit fraction as a function of cut variant. We plot this for our standard fit technique (black), a fit with only 13×13 bins of efficiency instead of our standard 25×25 bin correction (red), and a fit with the background likelihood penalty terms removed (blue).

result these cut variants have little additional effect on the signal purity as evidenced by Figure 7.12. Because one has nearly the same signal purity for each variant, it is unclear to us how incisive a test of systematics this is. The variation in the amplitude, phases, and fit fractions for the D^0 are shown in Figures 7.13, 7.14, and 7.15. The sum of the χ^2/D.o.F. for the three Dalitz projections are shown for the cut variants of the D^0 in Figure 7.11. We were unable to get convergent fits using cut variant #8. We will exclude these variants in computing the cut variant systematic for the D^0.

Another "down side" to having a very good signal to noise, is that there is is insufficient background to make good likelihood penalty systematic. We were unable to get convergence using anything other than a "flat" background and at that point, there no likelihood penalty terms to study.

Table 7.5 summarizes the systematic error calculation for the the D^0 amplitudes, phases, and fit fractions. In most cases the systematic errors are small compared to the statistical errors. To a large extent this reflects the relatively small statistics for the tagged $D^0 \to K_s^o K^- K^+$ decay sample. Finally Figures 7.6 and Figures 7.7 give the systematic uncertainty for the fit fractions in the two vicinities of the ϕ peak which is relevant to the use of the $K_s^o \phi$ state as a CP odd state for lifetime measurement.

Table 7.4: D^0 cuts variants. $EZDBIT = 1$ is a Sezdee skim level cut with a loose particle id and a detachment cut of $l/\sigma > 2.5$.

CUT Variant	Cuts				
	l/σ	EZDBIT	CL2	kaonicity	goodks
1	4.	1.	0.01	3.	2
2	6.	1.	0.01	3.	2
3	4.	-	0.01	3.	2
4	4.	1	-	3.	2
5	4.	1.	0.01	2.	2
6	4.	1.	0.01	1.	2
7	4.	1.	0.01	3.	1.
8	4.	1.	0.01	4.	-

Table 7.5: D^0 Errors

Parameter	Statistical	Systematics		Values
		Cut Variant	Efficiency	
$a_{f_0(980)\pi^+}$	–	–		1.0 (fixed)
$a_{a_0^\pm(980)K^\mp}$	0.04	0.01	0.001	$0.24 \pm 0.04 \pm 0.01$
$a_{\phi\pi^+}$	0.06	0.01	0.02	$0.59 \pm 0.06 \pm 0.03$
$\delta_{f_0(980)\pi^+}$	–	–	–	0° (fixed)
$\delta_{a_0^\pm(980)K^\mp}$	19°	5°	1°	$140 \pm 19^o \pm 6^o$
$\delta_{\phi\pi^+}$	11°	6°	2°	$-87 \pm 11^o \pm 7^o$
$f_{f_0(980)\pi^+}$	0.044	0.013	0.016	$0.692 \pm 0.044 \pm 0.02$
$f_{a_0^\pm(980)K^\mp}$	0.034	0.017	0.005	$0.124 \pm 0.034 \pm 0.02$
$f_{\phi\pi^+}$	0.036	0.006	0.015	$0.462 \pm 0.036 \pm 0.02$

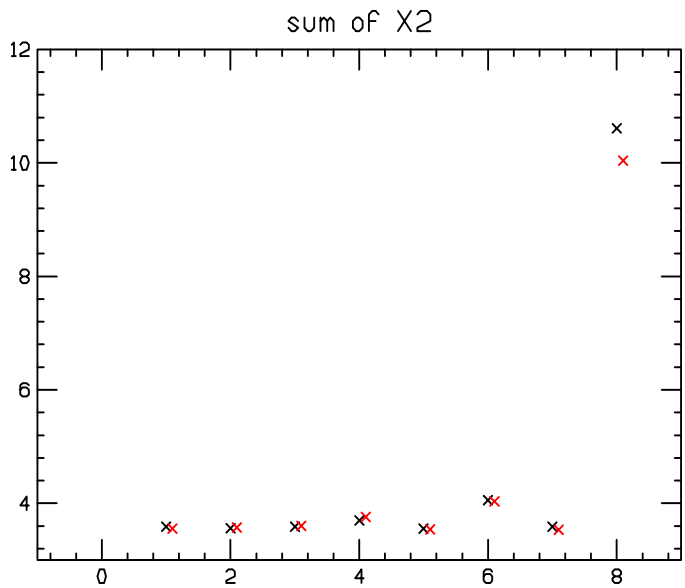

Figure 7.11: The D^0 sum of the χ^2/D.o.F. for the three mass projections as a function of cut variant. **The 8th fit variant didn't converge, and is exluded in the the following systematics plots**. We plot this for our standard fit technique (black), a fit with only 10×10 bins of efficiency instead of our standard 20×20 bin correction (red) We will use χ^2/D.o.F < 6 as our criteria for an "acceptable" fit.

Table 7.6: ϕ region D^0 Errors ($M^2_{K^+K^-} < 1.1$)

Parameter	Statistical	Systematics		Values
		Cut Variant	Efficiency	
$f_{f_0(980)\pi^+}$	5.8%	0.7%	4.9%	$40.1 \pm 5.8 \pm 5.1\%$
$f_{a_0^\pm(980)K^\mp}$	0.2%	0.03%	0.02%	$0.3 \pm 0.2 \pm 0.04\%$
$f_{\phi\pi^+}$	4.9%	0.6%	4.4%	$66.1 \pm 4.9 \pm 4.7\%$

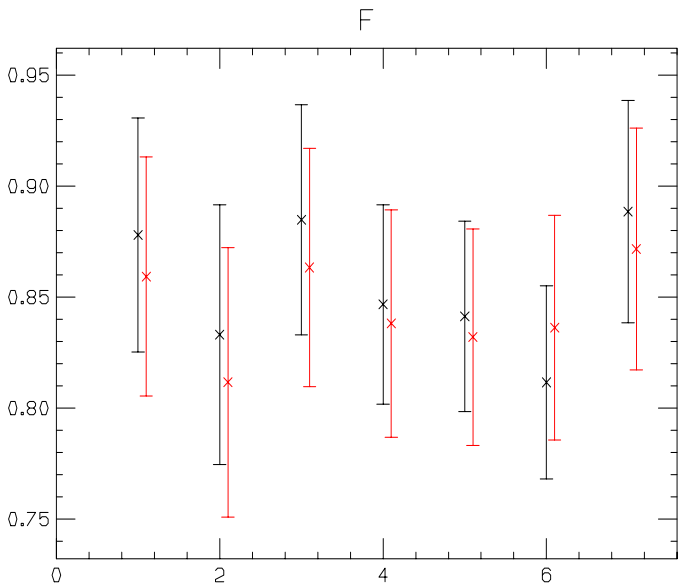

Figure 7.12: The D^0 signal fraction in the signal region as a function of cut variant. We plot this for our standard fit technique (black), a fit with only 10×10 bins of efficiency instead of our standard 20×20 bin correction (red).

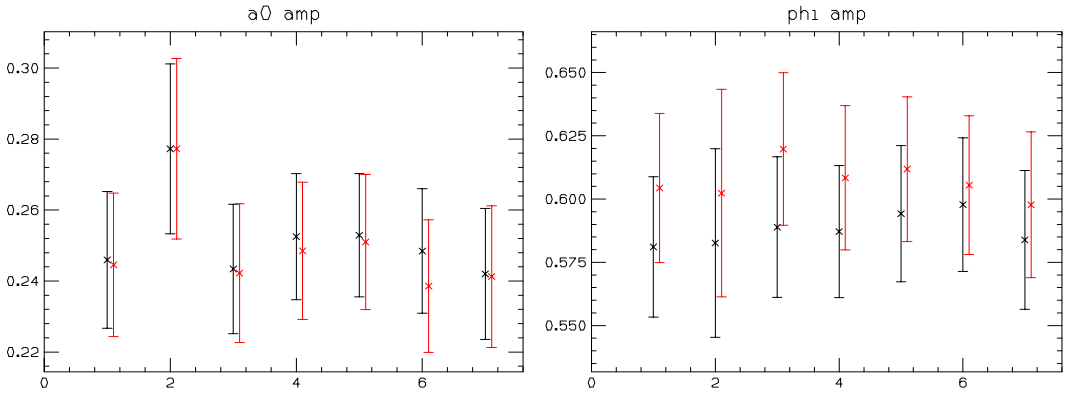

Figure 7.13: D^0 amplitude systematics. We plot each amplitude as a function of cut variant. We plot this for our standard fit technique (black), a fit with only 10×10 bins of efficiency instead of our standard 20×20 bin correction (red).

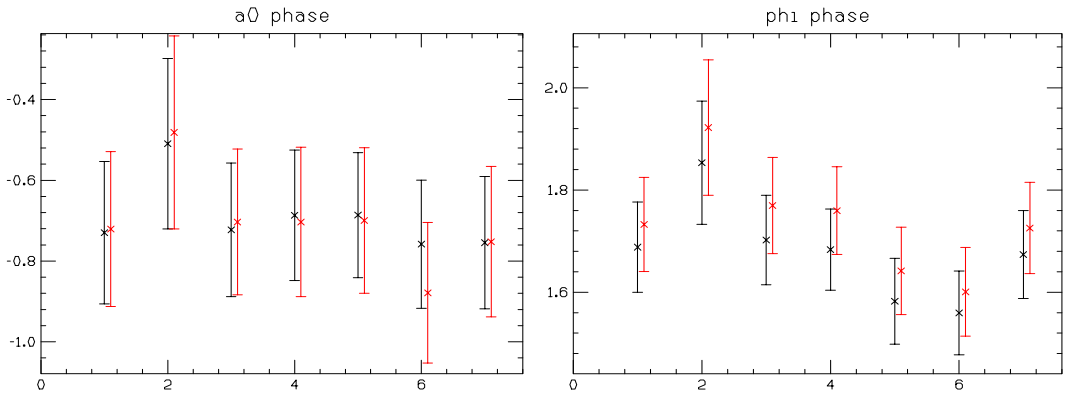

Figure 7.14: D^0 phase systematics. We plot each phase (in radians) as a function of cut variant. We plot this for our standard fit technique (black), a fit with only 10×10 bins of efficiency instead of our standard 20×20 bin correction (red).

Table 7.7: ϕ region D^0 Errors ($1.034 < M^2_{K^+K^-} < 1.042$)

Parameter	Statistical	Systematics		Values
		Cut Variant	Efficiency	
$f_{f_0(980)\pi^+}$	1.0%	0.2%	0.26%	$7.7 \pm 1.0 \pm 0.4\%$
$f_{a_0^\pm(980)K^\mp}$	0.01%	0.006%	0.1%	$0.05 \pm 0.01 \pm 0.1\%$
$f_{\phi\pi^+}$	2.0%	0.2%	0.1%	$93.0 \pm 2.0 \pm 0.3\%$

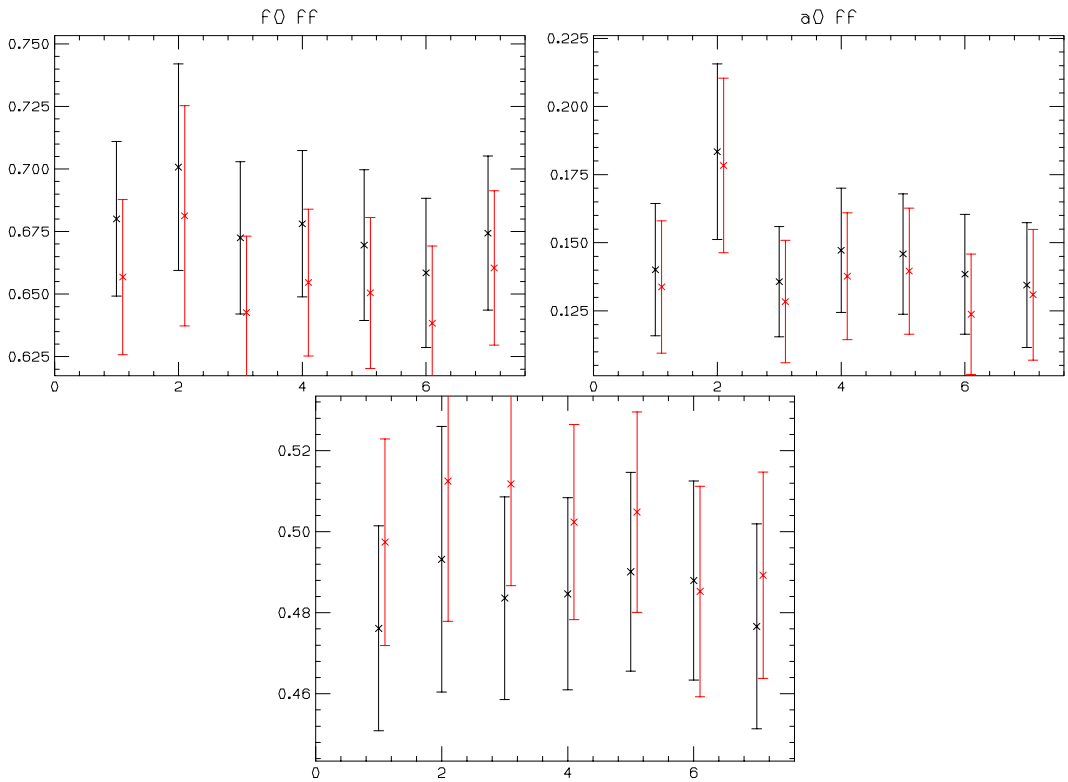

Figure 7.15: D^0 fit fraction systematics. We plot each fit fraction as a function of cut variant. We plot this for our standard fit technique (black), a fit with only 10×10 bins of efficiency instead of our standard 20×20 bin correction (red).

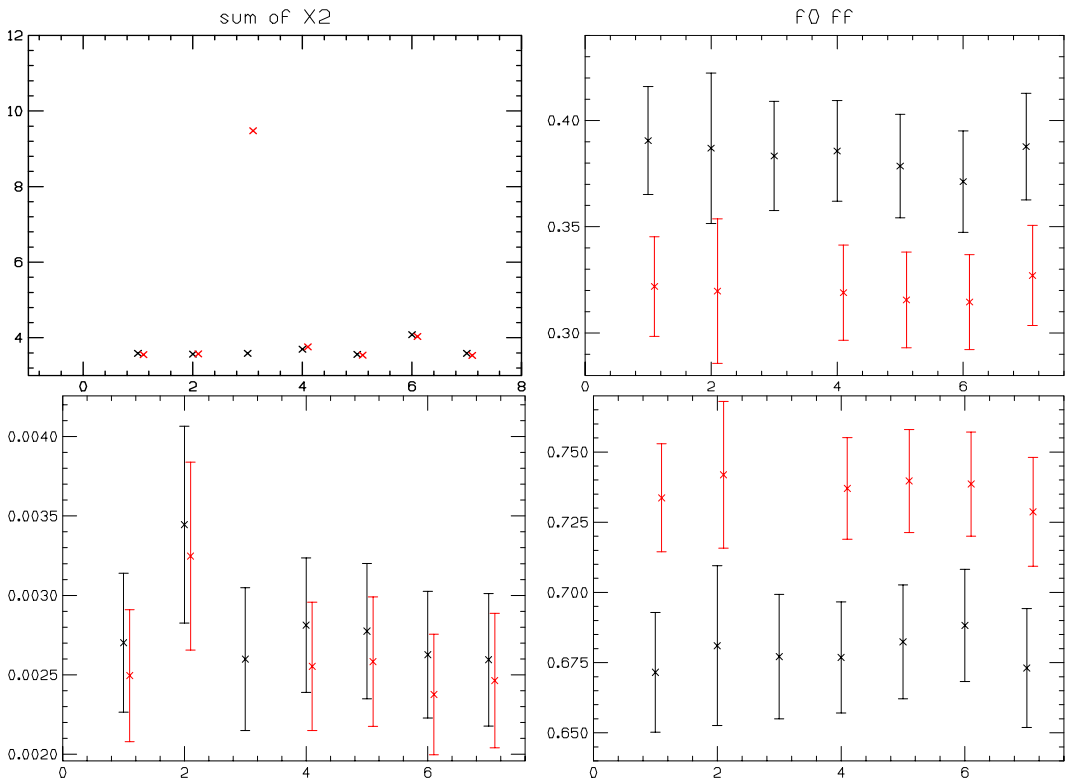

Figure 7.16: D^0 χ^2/D.o.F. for the three mass projections and fit fraction systematics in the ϕ region $M^2_{K^+K^-} < 1.1$. We plot each fit fraction as a function of cut variant. We plot this for our standard fit technique (black), a fit with only 10×10 bins of efficiency instead of our standard 20×20 bin correction (red).

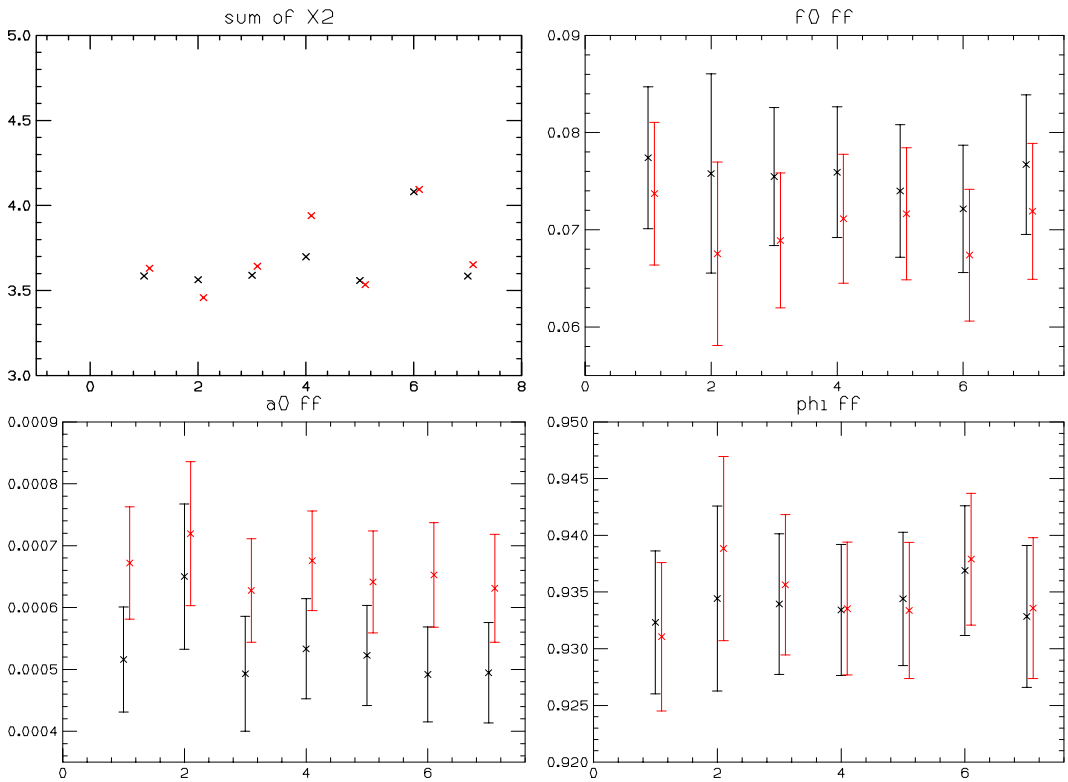

Figure 7.17: D^0 χ^2/D.o.F. for the three mass projections and fit fraction systematics in the ϕ region $1.034 < M^2_{K^+K^-} < 1.042$ We plot each fit fraction as a function of cut variant. We plot this for our standard fit technique (black), a fit with only 40 bins of efficiency instead of our standard 20×20 bin correction (red).

Chapter 8

Summary and Conclusions

This thesis has concentrated on the amplitude analysis of three charm decays $D^+ \to K^-K^+\pi^+$, $D_s^+ \to K^-K^+\pi^+$, and $D^0 \to K_s^0K^+K^-$. We will separately summarize our studies of the $K^-K^+\pi^+$ and $K_s^0K^+K^-$ final state. For each mode, our summary tables have inflated errors and adjusted central values in accordance with the mini-MC studies of Chapter 6.

8.1 Summary on $D^+, D_s^+ \to K^-K^+\pi^+$

Analyses of the $K^-K^+\pi^+$ final state have been done in the past. The first fully coherent analysis of these was performed by our preceding experiment, E687 [35]. I began the studies of the $K^-K^+\pi^+$ final state primarily as a "warm-up" exercise since the D_s^+ and D^+ Dalitz plots had interesting structures which were first measured in our preceding experiment by Dr. Rodney Greene[2] who was a former member of our research group. We thought it would be interesting to revisit these decays with the much better quality data available from FOCUS as a good calibration point.

For the most part, our studies confirmed Rodney's earlier observation on the $K^-K^+\pi^+$ final states. The two analyses are directly compared in Table 8.1 for the

D^+ and Table 8.2 for the D_s^+. Here are a few observations on these results and this analysis.

1. Both the $D_s^+ \to K^-K^+\pi^+$ and $D^+ \to K^-K^+\pi^+$ Dalitz plots are dominated nearly exclusively by quasi-two-body final states – primarily through the $\phi\pi^+$ and $\bar{K}^*(890)K^+$ final states.

2. The dominance of the $\phi\pi^+$ and $\bar{K}^*(890)K^+$ final states is much more complete for the D_s^+ where they encompasses 89% of the total fit fraction of the $K^-K^+\pi^+$ final state. For the D^+ the ϕ and $\bar{K}^*(890)$ final state encompasses only 57% of the $K^-K^+\pi^+$

3. The physical appearance of the $D^+, D_s^+ \to K^-K^+\pi^+$ Dalitz plots are strikingly different as shown in Figure 8.1. Because the dominant $\phi\pi^+$ and $\bar{K}^*(890)K^+$ contributions involve narrow, spin one resonances, the D^+ and D_s^+ (3-D) Dalitz plots are dominated by striking double lobe towers created through the angular correlations within the decays $\bar{K}^*(890) \to K^-\pi^+$ and $\phi \to K^-K^+$. The two ϕ lobes are relatively symmetric in appearance for both the D^+ and D_s^+; but the $\bar{K}^*(890)$ lobes are grossly asymmetric for the D^+ while still relatively symmetric for the D_s^+.

4. The most plausible explanation for the pronounced $\bar{K}^*(890)$ lobe asymmetry present for the D^+ is an interference with a broad spin 0 resonance contribution which is most likely the $\bar{K}^*(1430)K^+$. In order to produce this asymmetry the relative phase angle between the two interfering contributions must be roughly 90^0. To account for the much stronger asymmetry present in D^+ Dalitz plot, the contribution of the broad $\bar{K}^*(1430)$ resonance must be much larger in the D^+ relative to the D_s^+ Dalitz plot. Indeed Figure 8.1 shows a much larger broad

resonance "pedistal" on which the $\bar{K}^*(890)$ and ϕ lobes sit in the D^+ Dalitz plot. Although the FOCUS five resonance fit, is generally quite different than the E687 three resonance fit for the D^+, both experiments agree with these basic facts.

5. We found evidence for two additional contributions beyond the $\phi\pi^+$, $\bar{K}^*(890)K^+$, and $\bar{K}^*(1430)K^+$ used in the original E687 fit of the D^+ Dalitz plot. We are most certain about the inclusion of a $f_0(980)\pi^+$ contribution which significantly improved agreement between the data and model in both the $K^-\pi^+$ and $K^+\pi^+$ squared mass projections, and in our fits that has an amplitude which is $\approx 30\ \sigma$ from zero. We model this amplitude using the "WA76" parameterization found by an earlier strong scattering experiment[13], although there are significant questions about the validity of this parameterization. FOCUS is considering a potentially more accurate coupled channel analysis for this state. We are somewhat less certain about a 5th contribution – $f_J(1710)\pi^+$ – which visibly improves the agreement in the $K^+\pi^+$ squared mass projection and appears in our fit with an amplitude which is $\approx 13\ \sigma$ from zero. This resonance also has highly uncertain properties – even to the extent that it has a questionable spin. In our fits it is modeled with a width of $133\,MeV/c^2$ and a spin of 0.

6. Table 8.2 shows a considerable discrepancy between my values and the E687 amplitudes for the spin 0 resonant contributions for D^+ decay even though the fit fractions are reasonably consistent and the same amplitudes are considered in the fit. By way of contrast, the vector amplitudes in the D^+ decay are much closer. We believe that this discrepancy is probably due to a different multiplicative factor in the scalar amplitude conventions used by Rodney and myself since a variety of forms appear in the literature. Such a multiplicative

factor would not effect the fit fraction.

7. In the present analysis, the systematic errors, which we assessed by running the fit with different cuts, different ways of handling the background, and with different efficiency corrections, tend to be a comparable to the statistical errors. To a large extent, this is because we have chosen to quote the systematic errors in a very conservative fashion. In particular, the efficiency component of the $\phi\pi^+$ amplitude systematic error of the D^+ is extremely large for reasons we don't fully understand. In Section 7.1, we discuss how some of the shortcomings of this analysis which can be addressed prior to actual publication in order to reduce these systematic errors.

In the earlier E687 fit, Rodney used 5 resonances for the D_s^+ and only 3 for the D^+. Interestingly enough, given the much higher quality data available in FOCUS, we found we needed the same 5 resonant set for the D^+ and D_s^+ as Rodney had for D_s^+. It is intriguing that often very unusual resonances with either unknown quark content or expected hybrid or glueball states appear in the decays of charm particles. The $f_0(980)$ and $f_J(1710)$ in particular have generally appeared in compilations such as the Review of Particle Properties [1] as potential non-$q\bar{q}$ candidates and the $f_J(1710)$ has many of the properties expected in lattice gauge calculations for a low lying "glueball".[50]

Although we have no simple physics argument for the appearance of unusual resonances such as the $f_0(980)$ in both the $D^+, D_s^+ \to K^-K^+\pi^+$ Dalitz plots, there is a rather natural explanation (which was presented in Section 1.2.3, Chapter 1 and summarized here as well) for their observed presence in the $D_s^+ \to \pi^+\pi^+\pi^-$ Dalitz plot (initially analyzed by E691[39] and E687[18]) and in the $D^0 \to K_s^o K^+K^-$ Dalitz which is analyzed in this thesis for the first time. Given that the $f_0(980)$

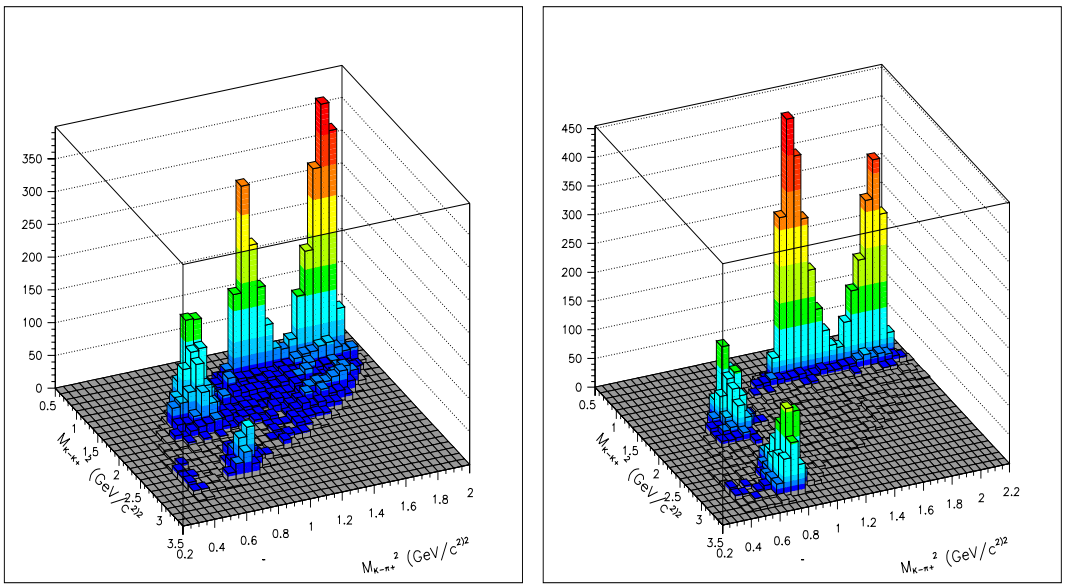

Figure 8.1: Dalitz 3-D plot for $D^+ \to K^+K^-\pi^+$ (left) and $D_s^+ \to K^+K^-\pi^+$ (right).

has simultaneous coupling into the channels $f_0(980) \to \pi^+\pi^-$ and K^-K^+, it must exist in the $D_s^+ \to K^-K^+\pi^+$ Dalitz plot at some level given its strong presence in the $D_s^+ \to \pi^+\pi^-\pi^+$. E687[18] also has some weaker evidence for an $f_0(980)\pi^+$ contribution in the D^+ Dalitz plot and hence one might expect to see it in the $D^+ \to K^-K^+\pi^+$ as well.

8.2 Summary on $D^0 \to K_s^o K^- K^+$

This thesis presents the first amplitude analysis of the $D^0 \to K_s^o K^- K^+$ final state. There are two principle motivations for such a study.

The first motivation is that this is an unusual decay which complements the interesting and previously studied $D^+ \to \pi^+\pi^-\pi^+$ decay. The $D^0 \to K_s^o K^- K^+$ final state appears to have a branching ratio consistent with a Cabibbo favored decay and obeys the usual $\Delta C = \Delta S$ selection rule. At quark level one would expect de-

Table 8.1: D^+ Fit Results

Parameter	Fitted Value	
	$E687$	$E831$
$a_{\bar{K}^*(890)^0K^+}$	1.0 (fixed)	1.0 (fixed)
$a_{f_0(980)\pi^+}$	-	$1.940 \pm 0.099 \pm 0.161$
$a_{\phi\pi^+}$	0.98 ± 0.05	$1.118 \pm 0.025 \pm 0.031$
$a_{K^*(1430)K^+}$	1.11 ± 0.07	$2.966 \pm 0.129 \pm 0.159$
$a_{f_J(1710)\pi^+}$	-	$0.616 \pm 0.048 \pm 0.084$
$\delta_{\bar{K}^*(890)^0K^+}$	0° (fixed)	0° (fixed)
$\delta_{f_0(980)\pi^+}$	-	$-100.0 \pm 2.6 \pm 2.7^o$
$\delta_{\phi\pi^+}$	$-159 \pm 8 \pm 11^o$	$118.9 \pm 4.0 \pm 6.7^o$
$\delta_{K^*(1430)K^+}$	$70 \pm 7 \pm 4^o$	$109.4 \pm 2.6 \pm 2.2^o$
$\delta_{f_J(1710)\pi^+}$	-	$-59.6 \pm 4.0 \pm 7.6^o$
$f_{\bar{K}^*(890)^0K^+}$	$0.301 \pm 0.020 \pm 0.025$	$0.285 \pm 0.013 \pm 0.009$
$f_{f_0(980)\pi^+}$	-	$0.301 \pm 0.027 \pm .042$
$f_{\phi\pi^+}$	$0.292 \pm 0.031 \pm 0.030$	$0.283 \pm 0.015 \pm 0.010$
$f_{K^*(1430)K^+}$	$0.370 \pm 0.035 \pm 0.018$	$0.362 \pm 0.030 \pm 0.028$
$f_{f_J(1710)\pi^+}$	-	$0.032 \pm 0.005 \pm 0.005$

Table 8.2: D_s^+ Fit Results

Parameter	Fitted Value	
	$E687$	$E831$
$a_{\bar{K}^*(890)^0K^+}$	1.0 (fixed)	1.0 (fixed)
$a_{f_0(980)\pi^+}$	0.48 ± 0.08	$1.202 \pm 0.056 \pm 0.075$
$a_{\phi\pi^+}$	0.91 ± 0.05	$1.026 \pm 0.021 \pm 0.059$
$a_{K^*(1430)K^+}$	0.44 ± 0.08	$0.824 \pm 0.065 \pm 0.119$
$a_{f_J(1710)\pi^+}$	0.27 ± 0.07	$0.399 \pm 0.042 \pm 0.036$
$\delta_{\bar{K}^*(890)^0K^+}$	0° (fixed)	0° (fixed)
$\delta_{f_0(980)\pi^+}$	$159 \pm 22 \pm 16^o$	$131.2 \pm 5.4 \pm 9.3^o$
$\delta_{\phi\pi^+}$	$178 \pm 20 \pm 24^o$	$150.2 \pm 5.4 \pm 9.1^o$
$\delta_{K^*(1430)K^+}$	$152 \pm 40 \pm 39^o$	$121.7 \pm 7.7 \pm 16.3^o$
$\delta_{f_J(1710)\pi^+}$	$110 \pm 20 \pm 17^o$	$80.4 \pm 11.3 \pm 3.5^o$
$f_{\bar{K}^*(890)^0K^+}$	$0.478 \pm 0.046 \pm 0.040$	$0.5026 \pm 0.0153 \pm 0.0291$
$f_{f_0(980)\pi^+}$	$0.110 \pm 0.035 \pm 0.026$	$0.1477 \pm 0.0108 \pm 0.0139$
$f_{\phi\pi^+}$	$0.396 \pm 0.033 \pm 0.047$	$0.3989 \pm 0.0134 \pm 0.0271$
$f_{K^*(1430)K^+}$	$0.093 \pm 0.032 \pm 0.032$	$0.0577 \pm 0.0075 \pm 0.0157$
$f_{f_J(1710)K^+}$	$0.034 \pm 0.023 \pm 0.035$	$0.0196 \pm 0.0033 \pm 0.0041$

cay through a $c \to su\bar{d}$ transition, leading to a final state (at quark level) of the form $D^0 \equiv c\bar{u} \to (su\bar{d})\bar{u}$. But unlike the usual Cabibbo allowed decays such as $D^0 \to K^-\pi^+$, three kaons appear in the final state each with either an s or $\bar{s}$ quark.

From the standpoint of decay dynamics the $D^0 \to K_s^o K^- K^+$ decay is very analogous to the decay $D_s^+ \to \pi^+\pi^-\pi^+$. At quark level we expect the final state $D_s^+ \equiv c\bar{s} \to (su\bar{d})\bar{s}$ and yet none of these strange quarks appear on the final state tripion. Although the explanation for this long known anomaly could be the Cabibbo allowed, non-spectator processes known as weak-annihilation $D_s^+ \to W^+ \to u\bar{d} \to \pi^+\pi^-\pi^+$ which might be expected to produce a nearly uniform Dalitz plot, in fact one observes a Dalitz plot strongly dominated by the $f_0(980)\pi^+$ final state. Since the $f_0(980)$ is one of only 3 established resonances with simultaneous dikaon and dipion couplings, nature is providing us with a large hint that the tripion decay of the D^+ occurs via $D_s^+ \equiv c\bar{s} \to (su\bar{d})\bar{s} \to (s\bar{s})_{f0}\ u\bar{d} \to (\pi^+\pi^-)\pi^+$. This is exactly the sort of quasi-two-body spectator process expected in the BSW model and observed in nearly all three body charm decays. Carrying this analogy through, we would expect the D^0 to proceed via: $D^0 \equiv c\bar{u} \to (su\bar{d})\bar{u} \to (u\bar{u})_{f_0} s\bar{d} \to (K^-K^+)K_s^o$ or (with an alternative re-arrangement): $D^0 \equiv c\bar{u} \to (su\bar{d})\bar{u} \to (u\bar{d})_{a_0^+(980)} s\bar{u} \to (K_s^o K^+)K^-$. The $f_0(980$ and $a_0^+(980)$ are well established resonances that have the ability to couple to dipions (*i.e.* u and d quarks) as well as dikaons and thus mediate these decay mechanisms. Hence a principle motivation for this study was to search for such quasi-two-body decays in the $D^0 \to K^-K^+K_s^o$ along with the previously observed decay $D^0 \to \phi K_s^o \to (K^-K^+)K_s^o$

Which leads to our second motivation – the analysis of the lifetime for CP odd eigenstates. There are interesting and somewhat conflicting information from CLEO[20] and FOCUS[19] that there are surprisingly large flavor oscillations of the form $D^0 \leftrightarrow \bar{D}^0$. If this is correct and CP is approximately conserved in charm decay, one would

expect that a CP even final state would have a different lifetime than a CP odd final state. FOCUS data indicates that the CP even K^-K^+ final state has a shorter lifetime than the CP mixed final state $D^0 \to K^-\pi^+$ by $(3.42 \pm 1.39 \pm 0.74)\%$. If so, one would expect an odd CP final state such as $D_s^+ \to \phi K_s^o$ to have a **longer** lifetime by about 3.42 %. The $D_s^+ \to \phi K_s^o$ final state is perhaps the most experimentally accessible CP odd[1] decay available to FOCUS and (perhaps) CLEO. If, as the argument in the previous paragraph suggests, there is a strong $f_0(980)K_s^0$ contribution to $D^0 \to K^-K^+K_s^o$, there will be an CP **even**[2] contamination to the $D_s^+ \to \phi K_s^o$ process in the same region of the $D^0 \to K^-K^+K_s^o$ Dalitz plot. It is therefore of considerable, topical interest to assess the level of $f_0(980)K_s^o$ in the "ϕ" region of the $D^0 \to K^-K^+K_s^o$ Dalitz plot.

We summarize our conclusions on this analysis:

1. Figure 8.2 shows a very clean (15 to 1 signal to noise) $D^0 \to K^-K^+K_s^o$ Dalitz plot with very prominent $\phi \to K^+K^-$ lobes and considerable "ground" clutter. We attribute the accumulation in the vacinity of the two ϕ lobes as a contribution from the $f_0(980)K_s^o$ final state. We attribute the accumulation at the large K^-K^+ mass edge of the Dalitz plot to the $a_o^+(980)K^-$ final state.

2. We are able to get a reasonably good fit to the complete Dalitz plot using just the three contributions ϕK_s^o, $f_o(980)K_s^o$ and and $a_o^+(980)K^-$ with phases and amplitudes given in Table 8.3. My analysis suggests that the largest resonant contribution is from $f_o(980)K_s^o$ although by virtue of its narrowness the ϕK_s^o forms a much more visible landmark.

[1]This final state is CP odd since the CP of the K_s^o and ϕ are both even, and to conserve angular momentum the $K_s^0\phi$ must be in an odd parity p-wave angular momentum state.

[2]Again the $f_0(980)$ and K_s^o are both CP even. This time they are in an even parity relative s-wave making the $f_0(980)K_s^o$ an even CP final state.

3. For this analysis, the systematic errors, determined in a way similar to the technique used to assess $D^+, D_s^+ \to K^-K^+\pi^+\pi^-$, tend to be smaller or comparable to the statistical errors. The statistical errors are larger for this analysis since yields are smaller. The signal is also much cleaner due to the tagging requirement and hence systematics due to backgrounds are likely to be much smaller.

4. In order to assess CP even pollution to the CP odd ϕK_s^o final state, we have computed the relative contributions of these two sources within a large and small band about the ϕ. In a broad region (within 50 MeV/c^2) of the ϕ the CP even contamination is 40% (based on the relative $f_0(980)$ and ϕ fit fraction); while in a narrow region (within 4 MeV/c^2 of the ϕ) the CP even contamination drops to 7.7%.

5. However our fit suggests quantum mechanical interference between the even and odd CP states which should be taken into account when reporting on eigenstate lifetime differences in this system. One indication of such interference is the asymmetry in the two ϕ lobes suggested by Figure 8.2 although it is not clear how statistically significant this asymmetry is.

8.3 What we would do differently

Writing up this thesis has given us the opportunity to contemplate how these three analyses could be improved with a little additional work prior to actual publication of the results. Here is a list of the improvements that we wish to pursue:

1. We could, in principle, put resolution smearing in our intensity model which might reduce the pulls we are seeing in narrow resonances.

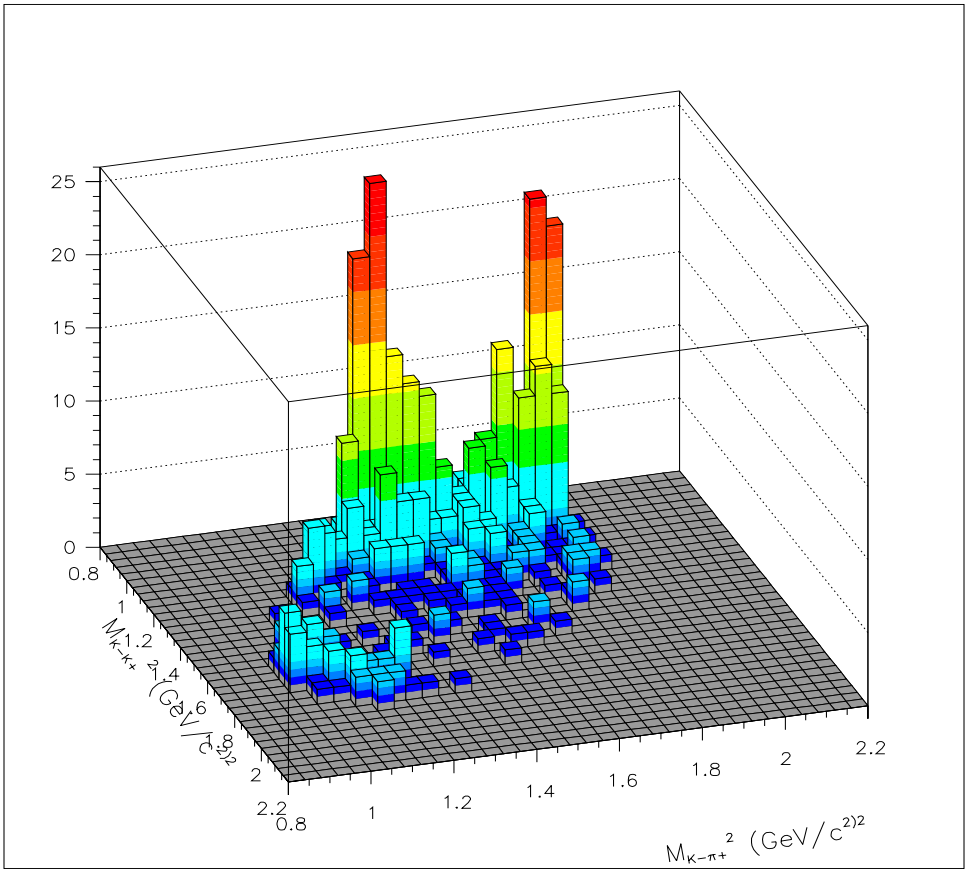

Figure 8.2: Dalitz 3-D plot of $D^0 \to K_s K^+ K^-$.

Table 8.3: D^0 Fit Results

Parameter	Fitted Value $\pm\sigma_{stat}$
$a_{f_0(980)K_s}$	1.0 (fixed)
$a_{a_0^\pm(980)K^\mp}$	$0.24 \pm 0.04 \pm 0.01$
$a_{\phi K_s}$	$0.59 \pm 0.06 \pm 0.03$
$\delta_{f_0(980)K_s}$	0° (fixed)
$\delta_{a_0^\pm(980)K^\mp}$	$140 \pm 19^o \pm 6^o$
$\delta_{\phi K_s}$	$-87 \pm 11^o \pm 7^o$
$f_{f_0(980)K_s}$	$0.692 \pm 0.044 \pm 0.02$
$f_{a_0^\pm(980)K^\mp}$	$0.124 \pm 0.034 \pm 0.02$
$f_{\phi K_s}$	$0.462 \pm 0.036 \pm 0.02$

2. It is clear to us that we have chosen our efficiency bins to be too large to compensate for the fact that the Monte Carlo samples were limited. As a result the principle systematic error for many of the narrow amplitudes are due to the efficiency correction. We believe that the most economical way of improving this situation would be to generate more and better Monte Carlo samples. We can get a "better" Monte Carlo sample by generating decays according to the intensities based on the amplitudes measured in this thesis, rather than according to a uniform phase space. As a result, the simulated events will populate the Dalitz regions where most of the data is, which is the region where the efficiency correction is most critical.

   Rather than using uniform size efficiency correction bins, we would switch over to an "adaptively" binned correction. In an adaptive bin scheme, an algorithm is used to repeatedly split bins until a certain minimum number of simulated

events appear in each bin. This allows one to make the finest scale efficiency correction compatible with having a certain counting statistics accuracy. We could assess binning systematics by raising the event count minimum used by the adaptive binner.

3. Our analysis of the $D^0 \to K_s^o K^- K^+$ state uses $D^{*+} - D^0$ tagging in order to determine if we have a D^0 or $\bar{D}^0$ state and (using the $\Delta C = \Delta S$ selection rule) whether or not the K_s^o emanated from a K^o or $\bar{K}^o$. This information was considered crucial so that we would know whether or not to combine the K_s^o with either the K^- or K^+ when searching for the strangeness zero $a_o^{\pm}(980)$ resonance. The D^* tagging also eliminated much of the background, but was very costly (by a factor of 4) in signal yield.

   We could potentially make an untagged analysis of the state where we fit the Dalitz intensity to a near equal mixture of the intensity for a D^0 and the intensity for a $\bar{D}^0$. This might both reduce statistical errors and provide a powerful check on systematic error.

4. We could easily search for additional resonant and non-resonant contributions for all three modes considered here. We clearly have problems in matching the $M^2(K^+\pi^+)$ projection for the the $D^+ \to K^- K^+ \pi^+$ decay. Although the match to the mass projections in $D_s^+ \to K^- K^+ \pi^+$ and $D^0 \to K_s^o K^- K^+$ are not bad, there may well be regions in the Dalitz plot which could be improved by adding in additional resonant channels. In the past, E687[18] found indications for resonances which were previously unknown or poorly established in charm Dalitz plots.

5. We could potentially compare the amplitude and phases for the $D^+ \to K^- K^+ \pi^+$ to those of the $D^- \to K^- K^+ \pi^-$ to search for CP violation in charm decay. In

this work the two samples are combined under the assumption that CP violations are small. We concentrate on this state since it is Cabibbo suppressed and potentially would exhibit stronger interference with a smaller CP violating amplitude than say the Cabibbo allowed decay $D^+ \to K^-\pi^+\pi^+$. Such a study would be strongly motivated if theoretical estimates of CP violation within the Dalitz plot were available.

6. At present, we are missing a potentially important systematic due to uncertainties in resonance parameters. It is straightforward but tedious to vary the Breit-Wigner resonance parameters within plus or minus their error on resonance mass or width. We believe, however, that the major "resonance" systematics are likely to come from broad, poorly known states which are unlikely not even able to be described by the simple Breit-Wigner pole form. The classical example of this problem is "coupled channel" parameterization of the $f_0(980)$. It is ironic that charm decays often decay by channels involving such unsual resonances. We hope that some of the "coupled-channel" analyses undertaken by our Milan FOCUS colleagues will guide us in assessing this potentially important systematic.

8.4 Future Charm Dalitz Analysis Physics

There are also some interesting potential long term extensions this work.

1. We are well configured to perform an analysis of $D^0 \to K_s^0 K^-\pi^+$ and $D^0 \to K_s^0 K^+\pi^-$. This might also be a profitable place to search for CP violation since it is another Cabibbo suppressed decay. I have studied both states with an intent to study their relative decay rates and Dalitz intensity.

2. Coupled channel analysis based on comparing channels such as $D_s^+ \to K^-K^+\pi^+$ and $D_s^+ \to \pi^-\pi^+\pi^+$ might well lead to a much better description of both final states. One "channel" which couples to both decays is the $f_0(980) \to K^-K+\ ,\pi^-\pi^+$. In a "coupled channel" analysis, the resonance is no longer considered to be a pole in the T matrix but rather becomes a pole in a K-matrix. As a result the resonance has a phase which depends on mass in a manner different than that of a Breit-Wigner.

3. According to Watson's Theorem, the phase shift between resonant amplitudes is due to final state interactions. In principle the S-matrix decribing these interactions can be calculated. If such calculations were available, one could multiply the vector describing the measured amplitudes by $S^{-1/2}$ to extract the bare "weak" amplitudes. It would be extremely interesting to find out if these bare amplitudes were relatively real as expected. If so, it would be interesting to compare the bare amplitudes to the predictions of factorization models and see if the bare amplitudes agree any better than the observed amplitudes which include FSI effects.

4. There are potentially interesting dynamic effects which are not included in our model for the Dalitz intensity. One such effect is the possibility of having non-resonance contributions with non-uniform, slowly varying Dalitz intensities. There are specific models for such terms.[49] One anticipates that the Dalitz plots with identical particles in the final state such as $D^+ \to K^-\pi^+\pi^+$ should exhibit the Goldhaber, Goldhaber, Lee and Pais (GGLP) effect which is related to Bose Einstein condensation and the Hanberry-Twiss effect. Present analyses have neglected such phenomena.

There are probably many other examples of interesting future "Dalitz physics" in hadronic charm and beauty decays.

Appendix A

Glossary of Terms

Baryon Any of a group of fundamental particles made up of three quarks

BGM Beam Gamma Monitor: an electromagnetic shower counter at zero degrees, designed to collect primarily uninteracted beam photons.

Boson a particle (as a photon or meson) whose spin is zero or an integral number.

BR Branching Ratio: the fraction of parent particles which decay a certain way.

Bremsstrahlung Energy loss through radiation.

Cabibbo favored Transition of a quark (charm) within the same generation (strange) is a Cabibbo favored decay and the decay amplitude is proportional to the $\cos\theta_c$, where $\theta_c = 13.1^0$ is the Cabibbo angle.

Cabibbo suppressed Cross generational transition of a quark ($c \rightarrow d$), and the decay amplitude is proportional to $\sin\theta_c$. (See **Cabibbo favored**)

Čerenkov radiation Čerenkov radiation arises when a charged particle in a material medium moves faster than the speed of light in that medium.

Čerenkov detector Čerenkov detector exploits the threshold requirement for the emission of Čerenkov radiation and the dependence of the emission angle on the particle velocity, to identify particles.

CITADL Čerenkov Identification of Tracks by an Algorithm using Digital Likelihood.

CL1 The confidence level a charm daughter does not point back to the primary vertex.

CL2 The confidence level that no tracks, not in the primary or secondary are in the secondary vertex.

Dalitz Plot A Dalitz plot is used to study the characteristic of three body decay . It is the scatter plot of m_{ab}^2 versus m_{ac}^2 in the decay $D \to abc$.

DCL The confidence level of a secondary or charm vertex.

End point Highest energy photon from bremsstrahlung.

Fermion A particle (as an electron, proton, or neutron) whose spin quantum number is an odd multiple of 1/2.

ℓ/σ The separation between the primary vertex and secondary vertex divided by its error.

Gluon a neutral spin one massless particle held to bind together quarks to form hadrons.

Hadron Any of a group of fundamental particles made up of quarks, and interact strongly.

HC Hadron Calorimeter: calorimeter to measure the energy of charged hadrons. This device is also used for triggering.

hxv Two planes of scintillators: one with counters arranged horizontally, the other with the planes arranged vertically. These counters are used for triggering.

Interaction length Mean free path of neutron interaction in matter.

IE Inner Electromagnetic shower counter: detects electromagnetic particles at smaller angles.

Link The requirement that a particle trajectory is found in the SSD's and the MWPC's and the two segments are associated.

Kick The "kick" of a magnet is a measurement of the integral of the B-field such that the angular deflection of a charged particle traversing the magnet is given by the kick over momentum to leading order in 1/momentum.

Lepton Any of a family of fundamental particles (as electrons, muons, and neutrinos) that have spin quantum number 1/2 and that experience no strong forces.

M1, M2 The first and second analysis magnet.

Mean free path the mean distance traveled by a particle without suffering a collision.

Meson Any of a group of fundamental particles made up of a quark and anti-quark, and have zero or integer number of quantum units of spin.

MG Master Gate: the trigger which initiates basic data acquisition.

OE Outer Electromagnetic shower counter: large aperture device for detecting electromagnetic particles.

OH Outer Hodoscope: large aperture scintillator array, used for triggering.

Photohadronic The part of the cross section of the photon interaction with the nucleus which creates final state hadrons.

Photoelectron Number of electrons ejected off the photocathod in a PMT (see **PMT**) by Čerenkov radiation.

PMT Photomultipliers (PMT's) are electron tube devices which convert light into a measurable current.

POSH Recoil positron shower hodoscope.

Primary vertex The photon-nucleon interaction point.

MWPC Multiwire Proportional Chamber: wire chamber for detecting charged particles.

Radiation length The distance over which the electron energy is reduced by a factor of $1/e$ due to radiation only.

RESH Recoil electron shower hodoscope.

Resonance The enhancement of a particle reaction or a scattering event. An extremely short-lived elementary particle.

SSD Silicon Strip Detector: the high resolution, silicon microstrip vertexing detector.

TR1 Scintillator trigger counter immediately upstream of the microstrip detector.

Trigger The electronic logic that is required to select the interesting events from the background is called the trigger.

TSSD Target Silicon Strip Detector.

References

[1] *Review of Particle Physics,* C. Caso *et al.,* The Europearn Physical Journal **C3** (1998) 1

[2] Rodney Green, *Nonleptonic Decays of Charm Mesons,* Ph.D. thesis, University of Illinois at Urbana-Champaing, 1995

[3] E687 Collab., P.L. Frabetti *et al.,* Phys. Rev. **D 50** (1994) 254.

[4] *Data Reduction and Error Analysis for the Physical Sciences,* P.R Bevington and D.K. Robinson

[5] *MINUIT Functional Minimization and Error Analysis Refrence Manual,* F. James, CERN Geneva, Switzerland

[6] Mark III Collab., J. Adler *et al.,* Phys. Lett. **B 196** (1987) 107.

[7] ARGUS Collab., H. Albrecht *et al.,* Phys. Lett. **B 308** (1993) 435.

[8] E687 Collab., P.L. Frabetti *et al.,* Phys. Lett. **B 407** (1997) 79.

[9] *Techniques for Nuclear and Particle Physics Experiments,* W.R. Leo

[10] E687 Collab. P. L. Frabetti *et al.* Nucl. Instrumm. Methods Phys. Res. **Sect.A320**) (1992 519.

[11] Mark 1 Collab. G. Goldhaber *et al.*, PRL **37** (1976) 255

[12] Fermi National Lab, http://www.gnal.gov/

[13] WA76 Collab., T.A. Armstrong, *et al.*, Z. Phys. **C 51** (1991) 351.

[14] E687 Collab. P.L. Frabetti, *et al.*, Phys. Lett. **B 364** (1995) 461.

[15] E687 Collab. P.L. Frabetti, *et al.*, Phys. LEtt. **B 321** (1994) 295

[16] D. M. Schmidt , R. J. Morrison , and M. S. Witherell, Nucl. Instrum. Methods, **A 328** (1993) 547.

[17] E687 Collab. P.L. Frabetti, *et al.*, E831 Nim Article

[18] E687 Collab. P.L. Frabetti, *et al.*, Phys. Lett. **B 407** (1997) 79

[19] E831 Collab. J.M. Link *et al.*, hep-ex/0004034

[20] CLEO Collab. R. Godang *et al.*, hep-ex/0001060

[21] E687 Collab. P.L. Frabetti, *et al.*, Phys. Lett. **B 313** (1993) 253 ; Phys. Lett. B328 (1994) 187

[22] E687 Collab. P.L. Frabetti *et al.*, Phys. Lett. **B 382** (1996) 312

[23] M. Bauer, B. Stech, M. Wirbel, Z. Phys. **C 29** (1985) 637;
M. Bauer and M. Wirbel, Z. Phys. **C 42** (1989) 671.;
M. Bauer, B. Stech. M. Wirbel, Z. Phys. **C 34** (1987) 103.

[24] P. Frabetti *et al.*, Phys. Lett. **B 321** (1994) 295;
E687 Collab., P.L. Frabetti *et al.,* Phys. Lett. **B 354** (1995) 486.

[25] M.Adamovich *et al.*, Phys. Lett. **B 280** (1992) 163

[26] J. C. Anjos *et al.*, Phys. Rev. **D 44** (1991)R3371

[27] F. Halzen, A. Martin, *Quarks and Leptons,* (1984)

[28] J. Alexander *et al.*, Phys. Rev. Lett. **B 65** (1990) 1184

[29] Thomas E. Browder , Klaus Honscheid , and Daniele Pedrini, Ann. Rev. Nucl. Part. Sci. **46** (1997) 395

[30] P. Frabetti *et al.*,Phys. Lett. **B 331** (1994)217

[31] J.C. Anjos *et al.*,Phys. Rev. **D 48** (1993)56

[32] H. Albrecht *et al.*,Phys. Lett. **B 308** (1993)435

[33] J. F. Donoghue *et al., Dynamics of the Standard Model* (1992)

[34] W. E. Burcham, M. Jobes *Nuclear and Particle Physics* (1995)

[35] P. Frabetti *et al.*, Phys. Lett **B 351** (1995) 591.

[36] C. Zemach, Phys. Rev. **B 140** (1965) 109

[37] C. Zemach, Phys. Rev. **B 140** (1965) 97

[38] C. Zemach, Phys. Rev. **B 133** (1964) 1201

[39] J.C. Anjos *et al.*, Phys. Rev. Lett. **62** (1989) 125

[40] Particle Data Group, R. M. Barnett *et al.*,Review of Particle Physics, Phys. Rev. **D 54** (1996) 557

[41] S. Malvezzi *et al.*, The $f_0(980)$ coupled-channel resonance and the K-matrix formalism, $E831$ internal memo, April 2000

[42] Anselmino, Bediaga, and Predazzi, CBPF-NF-045-95, Jul 1995, e-Print Archive hep-ph/9507292.

[43] Harry J. Lipkin, in AIP Conference Proceeding **196**: Heavy Quark Physics Ithaca, NY 1989 – Persius S. Drell & David L. Rubin, Editors p. 72-76

[44] J.M. Blatt, V.F. Weisskopf, *Theoretical Nuclear Physics,* (1952)

[45] P. Frabetti *et al.*, Phys. Lett. **B 407** (1997) 79.

[46] F. Buccella, M. Luisignola, and A. Pugliese, Phys. Lett. **B 379** (1996) 249.

[47] R. Balest *et al.*, Phys. Rev. Lett. **70** (1997) 1436

[48] J. Wiss, R. Gardner, Estimating Systematic Errors, $E687$ internal memo, February 1994

[49] I. Bediaga, C. Gobel, R. Mendez-Galain, PRL, **78** (1997) 22

[50] J. Sexton *et al.*, PRL, **75** (1995) 4563

Vita

Amir M. Rahimi was born in Khoy, Iran and moved to Urumieh at an early age. He attended Ferdowsi Mathematics and Physics High School. After completing his high school education, with the support of his parents, he emigrated to the United States. He settled in Portland Maine and studied Physics at the University of Southern Maine, before transferring to Rensselaer Polytechnique Institute in Troy New York, where he received his B.S degree in physics with CUM LAUDE honors in December of 1990. He was a recipient of a $9000 Rensselaer scholarship annually during his undergraduate years at RPI. He was involved in Nuclear Physics summer research at Brookhaven National Laboratory.

During the first two years of graduate school here at UIUC Amir was a teaching and laboratory assistant for undergraduates in the subjects of Mechanics and Electricity and Magnetism. He was listed among "The Incomplete List of Excellent Teaching Assistants" in the Spring of 92.

In 1993 he joined the FOCUS collaboration, Photoproduction of Charm with Upgraded Spectrometer at Fermilab, where he participated in fixed target run of 96-97. He participanted in the design, and construction of the Inner Muon detector and recomissioning the Cerenkov detector, as well as calibration and algorithm development and data analysis software.